



**HAL**  
open science

## Mercury accumulation in the sediment of the Western Mediterranean abyssal plain: A reliable archive of the late Holocene

D. Cossa, A. Mucci, Stéphane Guédron, Marina Coquery, Olivier Radakovitch, R. Escoube, S. Campillo, Serge Heussner

### ► To cite this version:

D. Cossa, A. Mucci, Stéphane Guédron, Marina Coquery, Olivier Radakovitch, et al.. Mercury accumulation in the sediment of the Western Mediterranean abyssal plain: A reliable archive of the late Holocene. *Geochimica et Cosmochimica Acta*, 2021, 309 (309), pp.1-15. 10.1016/j.gca.2021.06.014 . hal-03603517

**HAL Id: hal-03603517**

**<https://hal.science/hal-03603517>**

Submitted on 9 Mar 2022

**HAL** is a multi-disciplinary open access archive for the deposit and dissemination of scientific research documents, whether they are published or not. The documents may come from teaching and research institutions in France or abroad, or from public or private research centers.

L'archive ouverte pluridisciplinaire **HAL**, est destinée au dépôt et à la diffusion de documents scientifiques de niveau recherche, publiés ou non, émanant des établissements d'enseignement et de recherche français ou étrangers, des laboratoires publics ou privés.



Distributed under a Creative Commons Attribution - NonCommercial - NoDerivatives 4.0 International License

# Geochimica et Cosmochimica Acta

## Mercury accumulation in the sediment of the Western Mediterranean abyssal plain: A reliable archive of the late Holocene.

--Manuscript Draft--

Manuscript Number:	GCA-D-21-00102R1
Article Type:	Article
Keywords:	Mercury; Abyssal sediment; Holocene; Western Mediterranean
Corresponding Author:	Daniel Cossa, Ph D Université Grenoble Alpes FRANCE
First Author:	Daniel Cossa, Ph D
Order of Authors:	Daniel Cossa, Ph D Alfonso Mucci, Ph D Séphane Guédron, Ph D Marina Coquery, Ph D Olivier Radakovich Raphaelle Escoube Sylvain Campillo Serge Heussner
Abstract:	<p>Temporal reconstruction of Hg deposition from sediment archives is relatively straightforward in organic-rich or high sedimentation rate environments, such as lakes and ocean margins. To retrieve long-term records at regional or global scales, deep-sea sediments are more appropriate, but such records are scarce and their reliability has been questioned because of possible post-depositional Hg diagenetic remobilization. Here, we investigated the accumulation of Hg in the Balearic Abyssal Plain (2850 m deep) of the Western Mediterranean through a comprehensive characterization of the chemical and isotopic composition (organic carbon, nitrogen, sulfur, major and redox-sensitive elements) of sediment trap material and sediment cores. The analysis of material collected in the sediment traps, deployed at 250, 1440, and 2820 m, indicates that Hg is (i) partially re-emitted to the atmosphere and mobilized in the twilight zone and that (ii) the Hg downward flux depends on the primary production in surface waters, suggesting that organic matter (OM) acts as the main Hg-carrier phase. As the Hg concentrations of material collected in the traps vary little with depth but the Hg:C<sub>org</sub> ratio of the settling particulate matter decreases with depth, Hg must be re-adsorbed onto the more refractory fraction of the settling OM. Results of selective chemical extractions of the sediment indicate that Hg is very weakly coupled to the iron cycle but strongly associated with sulfur, supporting the assumption that its vertical distribution was only weakly altered by diagenetic remobilization. In addition, the distributions of S and <math>\delta^{34}\text{S}</math> in the sedimentary column exclude the possibility that local volcanism impacted on Hg enrichment of the sediments. Accordingly, a reconstruction of Hg accumulation rates (Hg-AR) during the Late Holocene is readily achieved. Biological mixing and smoothing of the sediment record, as revealed by the distribution of radionuclides in surface sediments, was considered in the interpretation of the Hg-AR record. The first anthropogenic Hg signal recorded in the studied cores corresponds to the Iron Age and the Roman Empire period, as Hg-ARs rose from the baseline (<math>0.7 \pm 0.2 \mu\text{g m}^{-2} \text{yr}^{-1}</math>) to an average value of <math>2.2 \pm 0.5 \mu\text{g m}^{-2} \text{yr}^{-1}</math>. The Hg-ARs return to baseline values at the decline of the Roman Empire, display a small increase during the Medieval Period (<math>1.5 \pm 0.5 \mu\text{g m}^{-2} \text{yr}^{-1}</math>), increase abruptly at the onset of the Industrial Era, leading to a ~10-fold increase in Hg deposition in the last 120 years (<math>8.9 \pm 1.4 \mu\text{g m}^{-2} \text{yr}^{-1}</math>), and retreat progressively over the past 50 years.</p>

1 *Running title: Hg in abyssal Western Mediterranean sediments*

2

3 **Mercury accumulation in the sediment of the Western Mediterranean abyssal**  
4 **plain: A reliable archive of the late Holocene**

5 Cossa, D.<sup>1,2\*</sup>, Mucci A.<sup>3</sup>, Guédron S.<sup>1</sup>, Coquery M.<sup>4</sup>, Radakovich O.<sup>5,6</sup>, Escoube R.<sup>2,7</sup>, Campillo,  
6 S.<sup>1</sup>, Heussner, S.<sup>8</sup>

7 <sup>1</sup>*Université Grenoble Alpes, ISTERre, CS 40700, F-38058 Grenoble Cedex 9, France*

8 <sup>2</sup>*IFREMER, Atlantic Center, LBCM, F-44031 Nantes, France*

9 <sup>3</sup>*Geotop and Department of Earth and Planetary Sciences, McGill University, 3450 University St.,*  
10 *Montreal, QC, H3A 0E8 Canada*

11 <sup>4</sup>*INRAE, UR RiverLy, 5 rue de la Doua CS 20244, F-69625 Villeurbanne, France*

12 <sup>5</sup>*IRSN (Institut de Radioprotection et de Sécurité Nucléaire), PSE-ENV/SRTE/LRTA, F-13115 Saint-Paul-*  
13 *lès-Durance, France.*

14 <sup>6</sup>*Aix Marseille Université, CNRS, IRD, INRAE, Coll France, CEREGE, F-13545 Aix-en-Provence, France*

15 <sup>7</sup>*Université de Lyon, ESN Lyon, Earth Sciences Department, BP 7000, F-69342 Lyon Cedex 07, France*

16 <sup>8</sup>*Univeristé de Perpignan Via Domitia, CEFREM, UMR 5110, F-66860 Perpignan Cedex, France*

17 *\*Corresponding author: dcossa@ifremer.fr*

18

19

20 **Abstract**

21 Temporal reconstruction of Hg deposition from sediment archives is relatively straightforward  
22 in organic-rich or high sedimentation rate environments, such as lakes and ocean margins. To  
23 retrieve long-term records at regional or global scales, deep-sea sediments are more appropriate,  
24 but such records are scarce and their reliability has been questioned because of possible post-  
25 depositional Hg diagenetic remobilization. Here, we investigated the accumulation of Hg in the  
26 Balearic Abyssal Plain (2850 m deep) of the Western Mediterranean through a comprehensive  
27 characterization of the chemical and isotopic composition (organic carbon, nitrogen, sulfur, major  
28 and redox-sensitive elements) of sediment trap material and sediment cores. The analysis of  
29 material collected in the sediment traps, deployed at 250, 1440, and 2820 m, indicates that Hg is

30 (i) partially re-emitted to the atmosphere and mobilized in the twilight zone and that (ii) the Hg  
31 downward flux depends on the primary production in surface waters, suggesting that organic matter  
32 (OM) acts as the main Hg-carrier phase. As the Hg concentrations of material collected in the traps  
33 vary little with depth but the Hg:C<sub>org</sub> ratio of the settling particulate matter decreases with depth,  
34 Hg must be re-adsorbed onto the more refractory fraction of the settling OM. Results of selective  
35 chemical extractions of the sediment indicate that Hg is very weakly coupled to the iron cycle but  
36 strongly associated with sulfur, supporting the assumption that its vertical distribution was only  
37 weakly altered by diagenetic remobilization. In addition, the distributions of S and  $\delta^{34}\text{S}$  in the  
38 sedimentary column exclude the possibility that local volcanism impacted on Hg enrichment of the  
39 sediments. Accordingly, a reconstruction of Hg accumulation rates (Hg-AR) during the Late  
40 Holocene is readily achieved. Biological mixing and smoothing of the sediment record, as revealed  
41 by the distribution of radionuclides in surface sediments, was considered in the interpretation of  
42 the Hg-AR record. The first anthropogenic Hg signal recorded in the studied cores corresponds to  
43 the Iron Age and the Roman Empire period, as Hg-ARs rose from the baseline ( $0.7 \pm 0.2 \mu\text{g m}^{-2}$   
44  $\text{yr}^{-1}$ ) to an average value of  $2.2 \pm 0.5 \mu\text{g m}^{-2} \text{yr}^{-1}$ . The Hg-ARs return to baseline values at the  
45 decline of the Roman Empire, display a small increase during the Medieval Period ( $1.5 \pm 0.5 \mu\text{g}$   
46  $\text{m}^{-2} \text{yr}^{-1}$ ), increase abruptly at the onset of the Industrial Era, leading to a ~10-fold increase in Hg  
47 deposition in the last 120 years ( $8.9 \pm 1.4 \mu\text{g m}^{-2} \text{yr}^{-1}$ ), and retreat progressively over the past 50  
48 years.

49

50 *Keywords:* Mercury, Abyssal sediment, Holocene, Western Mediterranean

51

52

## 1. INTRODUCTION

53 Aquatic sediments can provide a record of trace element deposition from atmospheric and  
54 riverine sources, including evidence of natural and anthropogenic forcing (Bertine and Goldberg,  
55 1977; Callender, 2003; Tribovillard et al., 2006). Historical reconstructions of trace element  
56 deposition from sediment archives are relatively straightforward if the element is not subject to  
57 strong diagenetic remobilization, of which Hg is a good example at least in organic-rich or high  
58 sedimentation rate environments such as lakes and marine coastal zones (Edgington and Robbins,  
59 1976; Smith and Loring, 1981; Fitzgerald et al., 2018; Guédron et al., 2016). Natural sources of  
60 Hg to sediments are mainly from atmospheric and submarine volcanism, wildfires, and low-  
61 temperature volatilization from soils and some continental rocks (Fitzgerald and Lamborg, 2005;  
62 Mason et al., 2012). Anthropogenic Hg sources include high-temperature processes (fossil fuel and  
63 biomass burning, municipal waste incineration, etc.), mining activities, deforestation/erosion,  
64 industrial processes, and past domestic uses (Outridge et al., 2018; UN-Environment, 2019).  
65 Variations of Hg accumulation rates (Hg-AR) from natural and anthropogenic sources have been  
66 reported in sediment cores. The volcanic origin of Hg in sediments of the Triassic-Jurassic Muller  
67 Canyon (Nevada, USA) (Thibodeau et al., 2016; Thibodeau and Bergquist, 2017) and Permian  
68 Buchanan Lake (Canada) (Sanei et al., 2012) was well illustrated, whereas seafloor hydrothermal  
69 activity was revealed by elevated Hg concentrations in Holocene sediments of the northwestern  
70 Pacific (Lim et al., 2017). The impact of climate on Hg deposition, in response to changes in  
71 precipitation or biological productivity, has been identified in lakes and marine sediments  
72 (Outridge et al., 2007; Grasby et al., 2013; Kita et al., 2013, 2016; Guédron et al., 2018). Sediment  
73 records of anthropogenic Hg deposition in freshwater lakes as well as near-shore and ocean margin  
74 environments are numerous and have been used to document increases in global or local sources

75 (Cossa et al., 2001; Muir et al., 2009; Hare et al., 2010; Mucci et al., 2015). Several studies  
76 underscore the rapid increase in Hg deposition starting at the beginning of the Industrial Era, i.e.,  
77 after AD 1850 (Azoury et al., 2013; Fitzgerald et al., 2018; Cooke et al., 2020). Enhanced Hg-ARs,  
78 linked to pre-industrial human activities, have been documented in strata of a Mediterranean lagoon  
79 sediment core dated to before ~AD 1850 (Elbaz-Poulichet et al. 2011). These authors highlighted  
80 two periods of increasing Hg deposition: the Middle Age, probably due to deforestation and  
81 biomass burning, and the XVI-XVII<sup>th</sup> Centuries, most likely associated with the increase in Hg  
82 mining activities resulting from the development of the Hg amalgamation process for the recovery  
83 of silver and gold. Evidence of (pre-)historical anthropogenic Hg emissions has also been identified  
84 in lake sediments (Thevenon et al., 2011; Guédron et al., 2016; Cooke et al., 2009; Corella et al.,  
85 2017), including those associated with mining and metal treatment during the Bronze and Iron  
86 Ages (Elbaz-Poulichet et al., 2020). These results bolster the adequacy of aquatic sediments as  
87 geochronological records of Hg deposition.

88 Deep-sea sediments are of particular interest in this context since, given their slow  
89 accumulation rates, they can potentially provide an entire record of Holocene deposition even in  
90 short cores. Episodic depositional events (e.g., mass-wasting) or/and changes in redox conditions  
91 in response to a gradual or sudden modification of the sedimentation regime may, however, modify  
92 the sedimentary records of multivalent elements (Thomson et al., 1998; Crusius and Thomson,  
93 2003). Mercury remobilization was documented at the oxic/suboxic boundary in deep-sea  
94 sediments where oxidation of pre-existing sulfides occurred (Mercone et al., 1999). Furthermore,  
95 chemical gradients across or near the sediment-water interface (SWI) can trigger a post-  
96 depositional redistribution of trace elements. Mercury enrichment at, or slightly below, the  
97 sediment-water interface (SWI) as well as downcore-decreasing concentrations were observed in

98 Arctic deep-sea sediments (Gobeil et al., 1999). Whereas increased anthropogenic Hg deposition  
99 was considered, the authors underlined that these profiles resulted from early diagenetic  
100 rearrangements of Hg in response to its affinity for authigenic Fe-oxyhydroxides that accumulate  
101 in the oxic layer. The effect of diagenetic remobilization was promoted by active bioturbation and  
102 low sedimentation rates, sedimentary conditions that are common to abyssal environments. In  
103 pelagic sediments of the Sea of Japan, Hg distributions display peaks near the SWI as well as in  
104 buried, brown “oxidized” sediment layers, also suggesting redox-driven diagenetic Hg  
105 redistribution (Kota, 2004). Conversely, in the sediment of the trench system and adjacent abyssal  
106 plain off the Kuril Islands, Hg burial is governed by atmospheric deposition and biological  
107 productivity. A Hg profile at this site, recording the last 120 years of deposition, features a  
108 maximum Hg flux corresponding to the second part of the XX<sup>th</sup> Century (Aksentov and Sattarova,  
109 2020). Irrespective, biological mixing (bioturbation and bioirrigation) can smooth the sediment  
110 records resulting from marked changes in Hg deposition rates. To sum up, records of Hg  
111 accumulation in deep-sea sediments have been shown to reflect the chronology of paleo and (pre-  
112 )historical Hg deposition, but post-depositional Hg redistribution cannot be ruled out.

113 High-resolution vertical profiles of Hg concentrations were determined in three ~30-cm  
114 sediment cores recovered from the Balearic Abyssal Plain (BAP), covering the Late Holocene  
115 Period, in the Western Mediterranean (Fig. 1). These data, combined with analyses of settling  
116 particulate material collected at various depths in the water column, allowed us to interpret the Hg  
117 sedimentary records in terms of post-depositional dynamic and depositional chronology. Results  
118 show that post-depositional remobilization of Hg is minor and that, despite significant biological  
119 mixing, the Hg accumulation rates record the impact of the Iron Age, the Roman Empire, and the  
120 onset of the Industrial Era.

121

122

## 2. MATERIAL AND METHODS

### 123 *2.1. Sampling*

124 Undisturbed sediment cores (24-33 cm long) were obtained from three stations (A, B, C),  
125 roughly 25 km apart from each other, in the BAP (also called Algero-Balearic or Algero-Provencal  
126 Basin) of the Western Mediterranean Basin during a cruise onboard the R/V Urania in March 2001  
127 (Fig. 1, Table 1). Cores were collected using a Wuttke-type multicorer and treated on-board  
128 immediately after recovery. Each core was sliced at 0.5 cm intervals over the first 5 cm, at 1 cm  
129 intervals from 5 to 20 cm, and at 2 cm intervals from 20 cm to the bottom.

130 At station C, three sediment traps (Technicap®, 0.125 m<sup>2</sup> diameter) were deployed along a  
131 mooring line at 250, 1440, and 2820 m depth, allowing the collection of 14 samples from each trap  
132 between April 2001 and April 2002 (Heussner et al., 1990; Zúñiga et al., 2007a). The samples were  
133 frozen immediately upon recovery, then freeze-dried, homogenized, and sub-sampled for various  
134 subsequent chemical analyses. Detailed descriptions of the cores and trapped material are given in  
135 the project final report (ADIOS, 2004).

### 136 *2.2. Chemical analyses*

137 Total Hg analyses were performed using an automatic atomic absorption spectrophotometer  
138 (AAS; Altec®, model AMA-254), according to the protocol described by EPA (2007). Briefly,  
139 weighed aliquots of freeze-dried sediment were introduced into the analytical system where they  
140 were heated to 550°C. The volatilized Hg was carried by a stream of oxygen to a gold trap onto  
141 which Hg was concentrated by amalgamation, before being thermally dissociated and analyzed by  
142 atomic absorption spectrometry. The detection limit was 7 ng g<sup>-1</sup>, calculated as 3.3 times the  
143 standard deviation of the blanks. We used a marine sediment certified reference material (CRM)

144 (MESS-2 from the National Research Council of Canada) to ensure the accuracy of the analyses;  
145 the mean value obtained ( $92 \pm 2 \text{ ng g}^{-1}$ ) was always within the range of the certified value:  $92 \pm 9$   
146  $\text{ng g}^{-1}$ . The reproducibility, defined as the coefficient of variation of six replicate analyses of the  
147 same CRM was 1.8 %. The analytical uncertainty (EURACHEM/CITAC, 2000) is  $\sim 10$  %. Labile Fe  
148 (and associated Hg) concentrations were estimated upon partial dissolution of the sediment with  
149 buffered ascorbate (pH 8.0) and dilute HCl (0.5 M) solutions according to protocols described by  
150 Kostka and Luther (1994). The ascorbate extraction is believed to dissolve only amorphous oxides,  
151 whereas the HCl extraction dissolves carbonates, crystalline Fe-oxyhydroxides, and acid volatile  
152 sulfides (AVS). It should be noted that the 0.5 M HCl extraction does not dissolve HgS (Mikac et  
153 al., 2000). To avoid losing the  $\text{Hg}^0$  formed during the ascorbate extraction, the sample was not  
154 stirred continuously during the 24 h extraction, as the original protocol prescribes, but gently mixed  
155 a few times, and the resulting solution was analyzed immediately after the extraction and  
156 centrifugation.

157 The activities of  $^{210}\text{Pb}$  in these cores were measured by alpha spectrometry of its daughter  
158 product  $^{210}\text{Po}$  (see details in Angelidis et al., 2011). An additional set of  $^{210}\text{Pb}$  activities were also  
159 obtained to refine the age-depth model between 13 and 20 cm in core B. They were acquired  
160 indirectly from the freeze-dried sediments by measuring the decay rate of its daughter isotope  $^{210}\text{Po}$   
161 by alpha spectrometry at the GEOTOP-UQAM Geochronology Laboratory. Uncertainties were  
162 estimated as two standard deviations (2s) for counting statistics, which is 4-8 % of the value  
163 obtained. A detailed description of the method can be found in Genovesi et al. (2011).

164 The total sulfur (S) and sulfur isotopic ratio ( $^{34}\text{S}:^{32}\text{S}$ ) of the solids were measured on an  
165 Isoprime model VisIon isotope ratio mass spectrometer coupled to an Elementar Vario PyroCube  
166 elemental analyzer running in continuous flow mode at the Geotop-UQAM Light Stable Isotope  
167 Geochemistry Laboratory. The freeze-dried and crushed sediment samples were weighted in tin

168 cups to obtain similar amounts of SO<sub>2</sub> for all samples and reference materials. The elemental  
169 analyzer was calibrated against known amounts of sulfanilamide. Two internal reference materials  
170 (IAEA-S2 & IAEA-S3;  $\delta^{34}\text{S} = +22.62 \pm 0.16 \text{ ‰}$ , and  $\delta^{34}\text{S} = -32.49 \pm 0.16 \text{ ‰}$ , respectively) were  
171 used to normalize the isotope ratios to the Vienna-Canyon Diablo Troilite (*VCDT*). A third  
172 reference material (IAEA-S1;  $\delta^{34}\text{S} = -0.3 \pm 0.00 \text{ ‰}$ ) was analyzed as an unknown to assess the  
173 exactness of the normalization. Results are reported in delta units ( $\delta$ ) in ‰ vs VCDT. The overall  
174 analytical uncertainty (2s), based on the propagation of uncertainties of the normalization of the  
175 internal reference materials and the samples, is better than  $\pm 0.2 \text{ ‰}$ , but it does not account for the  
176 homogeneity nor the representativity of the sample. Total sulfur concentrations and  $\delta^{34}\text{S}$  values  
177 were corrected for the porewater sulfate contributions, using porosity values (Suppl. Info., Table  
178 S1) and assuming [SO<sub>4</sub><sup>2-</sup>] was 0.0282 mole kg<sup>-1</sup> and a 21 ‰ VCDT value for the modern ocean  
179  $\delta^{34}\text{S-SO}_4^{2-}$  (Rees et al., 1978).

180 Major elements were analyzed by X-ray fluorescence spectrometry and results were published  
181 earlier (Angelidis et al., 2011). Total organic carbon (C<sub>org</sub>) content and its isotopic composition  
182 ( $\delta^{13}\text{C}_{\text{org}}$ ) were measured, after decarbonation (Suppl. Info., SI.2), by Cavity Ring-Down  
183 Spectrometry (Picarro Inc.<sup>®</sup>) coupled to a Combustion Module (Costech Inc.<sup>®</sup>) (CM-CRDS) using  
184 previously reported analytical methods, calibration and sample preparation (Guédron et al., 2019  
185 and references therein).

### 186 ***2.3. Age model and Hg accumulation rate calculation***

187 The Hg-ARs within the 3 cores were obtained after computation of an age-depth model based  
188 on the <sup>210</sup>Pb activity data and the four radiocarbon ages reported in core C by Zúñiga et al. (2007b).  
189 The age-depth model was derived using the IntCal20 calibration curve (Reimer et al., 2020) with  
190 consideration of the marine reservoir [R(t) = 390 ± 85 y BP] age of the Mediterranean Sea (Siani

191 et al., 2000). Details of the derivation of the age-depth model can be found in Suppl. Info. (SI.3).  
192 Hg-ARs were computed with consideration of the sediment compaction following the equation:

$$193 \quad \text{Hg-ARs} = 10 * [\text{THg}] * \text{SR} * (1 - \phi) * d \quad (1)$$

194 where [THg] is the Hg concentration ( $\text{ng g}^{-1}$ , Fig. 5a), SR the sedimentation rate ( $\text{cm yr}^{-1}$ , Suppl.  
195 Info., SI.3),  $\phi$  the porosity of the sediment (Suppl. Info., Table S1), and d the average grain  
196 sediment density,  $2.65 \text{ g cm}^{-3}$  according to Hamilton et al. (1976).

197

198

### 3. RESULTS

#### 199 **3.1. Sediment traps**

200 The Hg and  $C_{\text{org}}$  concentrations of the particulate material collected by the sediment traps at  
201 Station C are reported in Table 2. Year-long Hg records displayed similar seasonal variations,  
202 irrespective of the trap/sampling depth, with the highest concentrations in spring and autumn, and  
203 the lowest in summer (Fig. 2). Interesting to note are the relatively high Hg concentrations during  
204 the Saharan dust events identified in July and November 2001 (ADIOS, 2004). Most striking are  
205 the nearly constant, mean particulate Hg concentrations throughout the water column (averaging  
206  $128 \pm 23 \text{ ng g}^{-1}$ ,  $n = 42$ ) whereas mean  $C_{\text{org}}$  concentrations decreased by a factor of  $\sim 3$  between 250  
207 and 2820 m depth (Table 2). In other words, the Hg concentrations in settling particles remain the  
208 same during their transit through the water column while particulate organic carbon is  
209 remineralized or dissolved. Accordingly, the Hg: $C_{\text{org}}$  molar ratios increased from 0.06 to  $0.15 \times 10^{-6}$   
210 between 250 and 2820 m.

#### 211 **3.2. Sediment cores**

##### 212 **3.2.1. Sedimentary facies and geological settings**

213 Several cores sampled at stations A, B, and C in the BAP during the same cruise (ADIOS,  
214 2004) were described in two previous publications: one includes a description of their sequence  
215 stratigraphy and sediment lithology (Zúñiga et al., 2007b), whereas the other focusses on their trace  
216 element (Cu, Cd, Pb, Zn) composition (Angelidis et al., 2011). All the cores cover the Late  
217 Holocene Period and consist mainly of yellowish-brown, calcareous pelitic muds. They comprise  
218 five units (Fig. 3) referred to as U1 to U5 from the bottom to the top: two foraminifer-pteropod  
219 oozes (U1 and U4), two pteropod ooze layers (U2 and U5), and a turbidite deposit (U3). According  
220 to Zúñiga et al. (2007b), U3 is a zeolite-rich turbidite that likely originated from pyroclastic  
221 deposits derived from the Sardinian continental margin. For the three cores investigated in this  
222 study, U1 extended from the bottom of the cores to 14-16 cm below the sediment surface, whereas  
223 U5 occupied the top centimeter. The position of the other units in the sedimentary column varied  
224 slightly depending on the core: U2 was a 1-cm thick unit located between 13 and 16 cm from the  
225 surface, U3 was ~6-cm thick and found between 6 and 15 cm from the surface (7-13 cm, 9-15 cm,  
226 and 8-14 cm, for cores A, B, and C, respectively), and U4 was 6-8 cm thick and sat between 1 and  
227 9 cm from the surface (Fig. 3).

### 228 3.2.2. *Elemental distribution in the sedimentary column*

229 At station B, the elemental composition of one core was determined to detail the chemo-  
230 stratigraphy of the sedimentary column (Fig. 4). Two notable features appear (i) high Ca/Fe values  
231 in U2 and U5, and (ii) a spike in Si/Al at the U2-U3 boundary (Fig. 4a, f). The first feature is  
232 coincident with a positive excursion of the CaCO<sub>3</sub> content (Suppl. Info., Fig. S3) which reflects the  
233 abundance of pteropods in units U2 and U5, whereas the Ca/Fe distinguishes turbidites from  
234 pelagites because of the higher Fe and lower Ca contents of turbidites in the BAP (Rothwell et al.,  
235 2006). On the other hand, high Si/Al and K/Al (Fig. 4f and Suppl. Info., Fig. S3) clearly indicate

236 the presence of a lithogenic layer that characterizes the turbiditic layer (U3) (Zúñiga et al., 2007b).  
237 Below the turbidite unit, several parameters abruptly increase, namely  $N_{\text{tot}}$  (and associated  $C_{\text{org}}/N_{\text{tot}}$   
238 decrease),  $\delta^{13}\text{C}_{\text{org}}$ , S, and  $\delta^{34}\text{S}$  (Fig. 4c, e, g, and h), whereas, HCl-extractible Fe and Mn decrease  
239 sharply (Fig. 4i and j). The  $C_{\text{org}}:N_{\text{tot}}$  molar ratios (<8) and  $\delta^{13}\text{C}_{\text{org}}$  (>-25‰) indicate that the  
240 sedimentary organic carbon is mostly of marine (algal) origin (Meyers, 1994; Mackie et al., 2007).  
241 The  $\delta^{34}\text{S}$  values in units U1, U2, U4, and U5 are close to the modern seawater value (~21 ‰), with  
242 lower values (<10 ‰) in unit U3 (Fig. 4g). The sharp, positive gradient of  $\text{Fe}_{\text{HCl}}$  and  $\text{Mn}_{\text{HCl}}$   
243 concentrations at the interface of the U2-U3 units suggests that some Fe and Mn remobilization  
244 has occurred at this level despite the current oxic or suboxic redox conditions throughout the core  
245 ( $E_h > 180$  mV, ADIOS, 2004). This gradient most likely developed (temporary suboxic or anoxic  
246 conditions in response to the respiration of fresh OM at the SWI) in response to the turbidite (U3)  
247 depositional event, which buried the former SWI, as previously suggested by Zúñiga et al. (2007b).  
248 The S and  $\delta^{34}\text{S}$  sediment profiles (Fig. 4g and h) exhibit a slight decrease within the turbidite unit,  
249 a distinctive characteristic of the hosting zeolite mineral, an alteration product of volcanic material  
250 (Zúñiga et al., 2007b). A magmatic origin argues for low  $\delta^{34}\text{S}$  values (Liotta et al., 2012).

### 251 3.2.3. Mercury distribution in the sedimentary column

252 Mercury profiles in the three sediment cores are shown in figure 5a. The Hg concentrations  
253 varied from 9 to 100 ng g<sup>-1</sup>, with the highest values observed within the first 2 cm of the SWI and  
254 the lowest values at the bottom of the cores. The three Hg profiles exhibited the same vertical  
255 distribution patterns, characterized by an exponential decrease of Hg concentrations from the  
256 surface to the bottom of the cores, interrupted by a broad bump between 12 and 22 cm. These  
257 bumps reach 64, 89, and 58 ng g<sup>-1</sup> in cores A, B, and C, respectively. Mercury concentrations  
258 covary with  $C_{\text{org}}$  ( $R^2 = 0.52$ ,  $n = 81$ ,  $p < 0.01$ ). Notwithstanding the bumps (between 12-22 cm) over

259 which the Hg:C<sub>org</sub> molar ratios reach their highest value, the ratios decrease from  $\sim 1 \times 10^{-6}$  at the  
260 sediment surface down to  $0.17 \times 10^{-6}$  at the bottom (Fig. 5c).

261 Vertical profiles of Hg-AR exhibited similar patterns for the 3 cores, with the lowest average  
262 Hg-AR values ( $0.7 \pm 0.2 \mu\text{g}\cdot\text{m}^{-2}\cdot\text{yr}^{-1}$ ) in the basal unit (depth > 23 cm in U1) (Fig. 5d). The Hg-  
263 AR background in marine sediments is poorly documented (see review by Cooke et al., 2020), but  
264 our minimum value is of the same order of magnitude as the background Hg-AR (ca.  $1\text{-}2 \mu\text{g}\cdot\text{m}^{-2}\cdot\text{yr}^{-1}$ )  
265 recorded in various sediment archives (Lamborg et al., 2002; Serrano et al., 2013; de Simone  
266 et al., 2016; Cooke et al., 2020). Above 23 cm in U1, Hg-ARs increase up to 3.20, 3.95, and 2.47  
267  $\mu\text{g}\cdot\text{m}^{-2}\cdot\text{yr}^{-1}$  in core A, B, and C respectively, followed by a rapid decline in U4 above the turbidite  
268 (averaging  $1.0 \pm 0.2 \mu\text{g}\cdot\text{m}^{-2}\cdot\text{yr}^{-1}$  for the 3 cores). In U4, a low-amplitude “shoulder” is also visible  
269 between 3.5 and 6 cm in cores A and C (Fig. 5c, insert). Finally, the highest Hg-ARs ( $8.9 \pm 1.4$   
270  $\mu\text{g}\cdot\text{m}^{-2}\cdot\text{yr}^{-1}$ ) are observed in the surface unit (U5), which includes the last  $\sim 120$  years of deposition  
271 and is affected by mixing processes (Angelidis et al., 2011).

272

273

## 4. DISCUSSION

### 274 *4.1. Mercury transfer from the atmosphere to the sediment*

275 Despite the semi-enclosed nature of the Mediterranean Sea, the main Hg input to the open  
276 surface waters is, by far, from atmospheric deposition (e.g., Žagar et al., 2014). Little is known  
277 about the contributions of continental and hydrothermal inputs, except that mass-wasting events  
278 may reach the BAP (e.g., Cattaneo et al., 2020) and that hydrothermal fluxes, mostly located in the  
279 Tyrrhenian Sea, are rapidly transferred to the atmosphere (Bagnato et al., 2017). According to the  
280 data presented in Table 2, only 35 % of the atmospheric deposition flux ( $\sim 34 \text{ ng m}^{-2} \text{ d}^{-1}$  according

281 to Gencarelli et al., 2014) is found in large particles collected in the 250-m deep sediment trap.  
282 Hence, these observations suggest that a significant (~65 %) amount of the Hg is re-emitted to the  
283 atmosphere, in agreement with results of global air-sea exchange oceanic budgets and models (e.g.,  
284 Mason et al., 2012).

285 The Hg flux associated with settling particles collected at 250 m varied from 1.9 to 24.0 ng m<sup>-2</sup>  
286 d<sup>-1</sup> over the deployment period (Fig. 2); the range of this one-year-long record range is predictably  
287 broader than the range of Hg fluxes recorded in the Central Pacific during 24-hour sediment trap  
288 deployments (3.6 to 8.4 ng m<sup>-2</sup> d<sup>-1</sup> according to Munson et al., 2015). In the settling particles  
289 collected at 250 m during the sediment trap deployment above the BAP, the biogenic fraction was  
290 dominant (averaging 57 %). The concomitant, temporal variations of Hg concentrations and  
291 biogenic contents of the material collected in this trap (Fig. 2) as well as the positive correlation  
292 ( $R^2 = 0.60$ ,  $p < 0.01$ ) between Hg concentrations and the monthly average Chlorophyll-a  
293 concentrations in surface waters (data from Zúñiga et al., 2007a) support the hypothesis that the  
294 vertical transfer of Hg through the water column is governed by phytoplanktonic uptake in the  
295 euphotic zone and the subsequent formation and settling of large biogenic particles in response to  
296 zooplankton grazing and excretion. However, irrespective of depth, there is no significant  
297 correlation between Hg and C<sub>org</sub> concentrations in the trapped material. Biogenic material present  
298 in the settling particles of the Western Mediterranean consists of OM, calcium carbonates, and opal  
299 (Zúñiga et al 2007a), each component having a distinct affinity for Hg. In addition, the downward  
300 Hg flux is modulated by the lithogenic contribution (8-67 % according to Zúñiga et al., 2007a) to  
301 settling particles in the Mediterranean, ballasting biogenic material, especially during Saharan dust  
302 storms (Ternon et al., 2010). It is not surprising, owing to the diversity of settling particle  
303 composition, that its association with Hg is not directly accounted for by the C<sub>org</sub> proxy. Binding

304 sites on OM are numerous and the stability of Hg complexes increases from carboxylic to thiolic  
305 groups (Haitzer et al., 2003; Ravichandran, 2003; Skyllberg et al., 2006; Liang et al., 2019). Using  
306 synchrotron-based X-ray Absorption Near-Edge Structure (XANES) and Extended X-ray  
307 Absorption Fine Structure (EXAFS) spectroscopy, it was discovered that, in laboratory bacterial  
308 cell suspensions, all divalent Hg ions were complexed to cell-bound thiolic functional groups  
309 (Mishra et al., 2017; Song et al., 2020). Complexation of methylmercury to phytoplanktonic cells  
310 may occur through the same mechanism (Skrobonja et al., 2019). In the absence of thiol and sulfur  
311 concentration data in the sediment trap material, the assumption that Hg is strongly associated to  
312 organic planktonic material and their debris is likely sound. This does not mean that the Hg  
313 concentration of settling particles is not, occasionally, affected by Saharan dust inputs. Very high  
314 Hg concentrations ( $\sim 2 \mu\text{g g}^{-1}$ ) have been measured in small particles of African dust collected in  
315 the Azores Islands as a result of emissions from open-pit Hg mines or the mined rock formations  
316 in Algeria (USGS, 2001). However, these findings are not confirmed by recent measurements  
317 performed on Saharan dust collected during a survey in the Canary Islands, where they are  $< 100$   
318  $\text{ng g}^{-1}$  (Bailey, 2021). Additional results are needed to clarify this issue.

319 Mercury associated with particles collected in traps located at 1440 and 2820-m depth only  
320 accounts for ca. 70 % of the total flux at 250 m. This implies that ca. one-third of the Hg is  
321 remobilized from the settling material between 250 and 1440 m. This depth interval, the so-called  
322 “twilight zone”, which hosts heterotrophic activity, is the locus of net microbiological Hg  
323 methylation, with methylmercury (MeHg) accounting for up to 37 % of the THg (Cossa et al.,  
324 2009). Since MeHg has more affinity for the dissolved phase than inorganic Hg, Hg methylation  
325 is likely a critical mobilization process in the twilight zone. Below 1440 m, the Hg flux is invariant.  
326 Accordingly, the Hg:C<sub>org</sub> ratio nearly triples between 250 and 2820 m (Table 2). This increase

327 reflects the preferential removal of Hg from the surface ocean relative to C export, as observed in  
328 the Pacific Ocean water column (Munson et al., 2015), and implies that Hg released upon the  
329 remineralization of particulate OM during settling through the water column must re-adsorb onto  
330 the residual particulate matter. Culture experiments have shown that Zn released from degrading  
331 phytoplankton is rapidly scavenged back onto settling OM (John and Conway, 2014). Such a  
332 process is likely relevant for Hg since conditional stability constants for Hg complexed to dissolved  
333 and particulate OM are larger than those of Zn (e.g., Feyte et al., 2010). During the scavenging  
334 process, the nature of the particulate Hg-OM binding sites probably changes as C<sub>org</sub> is degraded  
335 during settling through the BAP water column, favoring the preferential binding of Hg to stronger  
336 ligands, such as thiol groups (Feyte et al., 2012; Liang et al., 2019; Guédron et al., 2020). Owing  
337 to the oxic conditions of the sediments, it can be expected that biogeochemical processes, similar  
338 to those occurring in the water column, control the Hg behavior in the sedimentary column.  
339 Nonetheless, the contrasting residence times in the two environments must be considered: the  
340 settling time of particles through a 2850 m water column is on the order of weeks, whereas the  
341 accumulation of a 30 cm thick sediment column is counted in thousands of years.

#### 342 ***4.2. Diagenetic remobilization of mercury in the sediment column***

343 Three main differences in the Hg and C<sub>org</sub> geochemical behaviors are observed between  
344 sediment and settling particles collected in the traps. First, except for units U1 and U2, a strong  
345 correlation is found between the two parameters in the three cores ( $R^2 = 0.80$ ,  $p < 0.01$ , Suppl. Info.  
346 Fig. S4). Second, the Hg:C<sub>org</sub> ratio in the sediments decreases with depth, in contrast to the particles  
347 that settles through the water column. Finally, whereas both Hg and C<sub>org</sub> exhibit their highest  
348 concentrations in the first cm below the SWI (Fig. 5a and b) and the C<sub>org</sub> concentrations decrease  
349 with increasing depth in the sediment (Fig. 5b) as a result of active microbial remineralization, the

350 decreasing Hg:C<sub>org</sub> ratio (Fig. 5c) reflects a faster decreasing rate of Hg deposition with depth. This  
351 interpretation rests on the hypothesis that diagenetic Hg remobilization is limited, and supports a  
352 rise in anthropogenic Hg deposition in surficial sediments.

353 It has been proposed that the vertical distribution of Hg in Arctic deep sediments may be  
354 modulated by diagenetic remobilization and shuttling with the Fe cycle (Gobeil et al., 1999). In  
355 order to explore this possibility, we analyzed the Hg associated with amorphous iron oxides or  
356 ascorbate-extractable Fe (Fe<sub>asc</sub>) in the BAP sediments. The Fe<sub>asc</sub> fraction accounts for  $0.7 \pm 0.4$  %  
357 of the total Fe, whereas the associated Hg (Hg<sub>asc</sub>) accounts for  $0.9 \pm 0.7$  % of the total Hg (Suppl.  
358 Info., Table S2). In addition, Hg<sub>asc</sub> and Fe<sub>asc</sub> are not correlated, except weakly in the first 5 cm of  
359 the sediments ( $R^2 = 0.51$ ,  $p < 0.10$ ). Thus, our results indicate that the Hg associated with the  
360 amorphous iron oxide fraction is very small, implying that the amount of Hg diagenetically  
361 recycled with Fe oxides in BAP sediments is very limited. This conclusion is consistent with results  
362 of *in situ* experiments at a lacustrine sediment-water interface and modeling that show Hg to be  
363 preferentially bound to functional groups of the OM rather than to the hydroxyl groups of Fe-  
364 oxy(hydro)oxide surfaces (Feyte et al., 2010). The occurrence of the turbidite layer (U3), which  
365 capped the underlying layers (U1 and U2), also brings complementary insights about the potential  
366 redistribution of Hg resulting from a transitory redox change in the sediment column. The  $\delta^{34}\text{S}$   
367 values below the turbidite fail to indicate the presence of significant sulfate reduction products  
368 (Fig. 4h). Nonetheless, the sharp drop in Fe<sub>HCl</sub> and Mn<sub>HCl</sub> concentrations (Fig. 4i and j) immediately  
369 below the turbidite (U3) could be evidence of transient suboxic or anoxic conditions that developed  
370 at the top of the pteropod ooze (U2), fueled by the rapid burial of fresh OM that had accumulated  
371 at the former SWI. Under these conditions, reactive Mn and Fe in these sediments would have been  
372 reductively dissolved and migrated from U1 to U3 where the Fe and Mn were oxidized and

373 reprecipitated as authigenic oxides by the oxygen advected with the porewaters of the turbidite  
374 (Fig. 4i and j). A similar process has been described in detail for cores collected in a coastal  
375 environment subjected to a mass-wasting event (Mucci et al., 2003). In the BAP, the reductive  
376 dissolution of iron oxides below the turbidite, which might have occurred after the U3 turbidite  
377 deposition, is not accompanied by a decrease in Hg concentration as Hg concentrations peak within  
378 U1 (Fig. 5a). In other words, despite the microbial decay of fresh OM and the transitory  
379 development of reducing conditions that lead to the reductive dissolution of Fe oxides, Hg  
380 remained mostly immobile or was rapidly re-adsorbed onto the solid sediment including OM, as in  
381 the water column, through binding to reduced sulfur compounds. Indeed, the strong affinity of Hg  
382 for reduced sulfur seems to modulate both (i) scavenging through the water column and (ii)  
383 sediment sequestration following diagenetic remobilization. This hypothesis is supported by the  
384 strong correlations between the distributions of Hg and sulfur in the sediment of Core B (Fig. 6).  
385 Most of the variability in Hg concentrations in the deepest part (>23 cm) of the core, and in the  
386 turbidite unit (U3) of the sediment, is explained by the sulfur content, as illustrated by their  
387 respective correlations ( $R^2 = 0.65$  and  $0.74$ ,  $p < 0.10$  and  $p < 0.05$ ). In these two layers, the Hg/S  
388 varies only slightly, whereas, in U1 (<23 cm), U2, U4, and U5, the regression coefficient of the  
389 Hg-S relationship is much higher (Fig. 6). It is interesting to note that in the turbidite (U3), in which  
390 a volcanic contribution has been ascertained (see section 3), there is no Hg anomaly that could hint  
391 at a geogenic origin (Fig. 6, insert). In other words, the distribution of Hg:S ratios through the core  
392 fails to reveal possible Hg inputs of volcanic or hydrothermal sources. The higher Hg:S ratio, in  
393 U1 (<23 cm), U2, U4, and U5 units (Fig. 6) could reflect the accumulation of fine cinnabar particles  
394 emitted to the Mediterranean atmosphere from the Almaden mines (Spain) since the beginning of  
395 their operation around 430 BC (Moreno et al., 2005).

396 At this stage, we can conclude that the participation of Hg in the diagenetic Fe-cycle in these  
397 abyssal sediments is limited and that a possible influence of local volcanism on Hg enrichment of  
398 the sediments is ruled out. Thus, the vertical distribution of Hg in the BAP likely provides an  
399 exploitable chronological record of Hg deposition during the Late Holocene Period, although  
400 smoothing by biological mixing must still be taken into consideration in the interpretation of this  
401 record.

### 402 ***4.3. Chronology of Hg fluxes and deposition***

#### 403 *4.3.1. Modern deposition*

404 Computed Hg-ARs for the first 2 cm (based on radionuclide profiles), which represent the last  
405 120 years, averaged  $9.8 \pm 0.9$ ,  $8.3 \pm 1.0$ , and  $8.5 \pm 1.8 \mu\text{g m}^{-2} \text{yr}^{-1}$  in cores A, B, and C, respectively  
406 (Figs. 5d and 7). Although the  $^{210}\text{Pb}$  profile shows a classical decrease with depth (Suppl. Info.,  
407 Fig. S1), a previous study using artificial radionuclides ( $^{137}\text{Cs}$  and  $^{239,240}\text{Pu}$ ; Garcia-Orellana et al.,  
408 2009) divulges that the Hg signal has been smoothed by biological mixing. Even though they may  
409 carry large uncertainties, estimated surficial (0-1 cm) Hg-ARs ( $8.6 \pm 1.9 \mu\text{g m}^{-2} \text{yr}^{-1}$ ) for the last 50  
410 years in the three cores are consistent with those ( $8.4 \mu\text{g m}^{-2} \text{yr}^{-1}$ ) measured over the same period  
411 in the Ligurian Sea (Heimbürger et al., 2012). Although not directly comparable due to possible  
412 diagenetic processes in the nepheloid layer, these values are also consistent with those derived from  
413 the analysis of the sediment trap material recovered at 2820 m ( $3.1 \pm 0.5 \mu\text{g m}^{-2} \text{yr}^{-1}$ , Table 2),  
414 which integrates the Hg deposition between 2001 and 2002. These lower recent deposition rates  
415 concur with the reported  $\sim 30\%$  decrease of Hg concentrations in the western Mediterranean deep  
416 waters between 1989 and 2012 (Cossa et al., 2020) as well as with the reduced Hg emissions from  
417 utilities over the past two decades, that led to lower global anthropogenic emissions and associated  
418 deposition to ecosystems (Zhang et al., 2016). Overall, the observed sediment-surface Hg-

419 enrichment is consistent with the increasing global anthropogenic Hg emissions since the  
420 beginning of the Industrial Era (i.e., ~AD 1850 according to Outridge et al., 2018). The  
421 corresponding Hg-ARs are at least one order of magnitude larger than for the pre-Anthropocene  
422 epoch (i.e., before 1000 BC) background value ( $0.7 \pm 0.2 \mu\text{g m}^{-2} \text{yr}^{-1}$ ) in the three cores.

#### 423 *4.3.2. Pre- and historical Hg deposition*

424 The first rise in Hg-ARs recorded in the 3 cores recovered in the BAP appears during the Iron  
425 Age period (i.e., the upper part of U1, ~800 to 50 BC), as Hg-ARs increased from the baseline ( $0.7$   
426  $\pm 0.2 \mu\text{g m}^{-2} \text{yr}^{-1}$ ) to an average value of  $2.5 \pm 0.7 \mu\text{g m}^{-2} \text{yr}^{-1}$  (t-test,  $p < 0.01$ ). Because atmospheric  
427 circulation in the Mediterranean Basin is dominated by westerly winds (Ait Brahim et al., 2019;  
428 Azuara et al., 2020), the most probable source of Hg is the Iberian Peninsula where intense mining  
429 activities have been reported since the late Holocene period (Kassianidou and Knapp, 2005;  
430 Martinez-Cortizas et al, 1999), accounting for about half of the registered global Hg production in  
431 Europe (Hylander and Meili, 2003). Metal mining was also very active in Sardinia (Terpstra, 2021).  
432 This peak in Hg-AR is synchronous with the first  $^{206/207}\text{Pb}$  isotope anomaly (down to ~1.192)  
433 reported by Angelidis et al. (2011, Fig. 7, Suppl. Info., Fig. S1), and is consistent with known lead,  
434 silver, and cinnabar refining, smelting, and mining activities in Iberia during the Iron Age and  
435 Roman Empire (Nriagu, 1983). These activities are also recorded in other Mediterranean coastal  
436 sediments (Elbaz-Poulichet et al., 2011; Serrano et al., 2013), in a Spanish mire (Martinez-Cortizas  
437 et al., 1997; 1999), and remote alpine lake sediments (Elbaz-Poulichet et al., 2020; Thevenon et  
438 al., 2011). In contrast to signals recorded in other archives, the dome-shaped Hg-AR record in the  
439 BAP sediments during the Iron Age and Roman Empire (Fig. 7) likely results from smoothing by  
440 biomixing of the geologically high-frequency variation of the anthropogenic signal. At the decline  
441 of the Roman Empire, ca. AD 200, Hg-ARs return to baseline values, just before the turbidite is

442 deposited (U3) (~AD 300). The latter was laid down at the same period as the Mediterranean  
443 megaturbidite was triggered by the AD 365 Crete earthquake and tsunami (Polonia et al., 2013).  
444 From that time on to ~AD 1800, Hg-ARs increase slightly and gradually from, on average,  $1.0 \pm$   
445  $0.2$  to  $1.5 \pm 0.5 \mu\text{g m}^{-2} \text{y}^{-1}$  in the 3 cores. Surprisingly, no marked peak was found corresponding  
446 to the Medieval Period (i.e., AD 500 to 1500), although this period is known for the massive  
447 development of metallurgy throughout Europe, including the intense metallurgical activities during  
448 the Islamic Period in Spain (AD 711 to 1492), a period documented by sharp increases in both Hg  
449 and Pb-ARs in almost all European records (Fig. 7, references herein). We consider that given the  
450 magnitude of the source, the low sedimentation rate, and the resolution of the BAP record,  
451 biomixing may have smoothed the signal and obliterated these short-duration mining peaks.

452

## 453 **5. SUMMARY AND CONCLUSIONS**

454 Temporal reconstruction of Hg deposition from sediment archives is relatively straightforward  
455 in organic-rich or high sedimentation rate environments since its diagenetic remobilization is  
456 limited compared to the large excursions in Hg emissions and deposition over the past 2000 years.  
457 Hg accumulation occurs mostly in areas, i.e., freshwater lakes or near-shore marine zones, close to  
458 point sources. To retrieve historical records on regional or global scales, deep-sea sediments are  
459 more appropriate. In addition, due to their slow accumulation rates, deep-sea sediments can provide  
460 deposition patterns over long periods, at least covering the Holocene. Such records are scarce, and  
461 their reliability has been questioned because of possible diagenetic remobilization, physical and  
462 biological mixing as well as post-depositional Hg redistribution resulting from mass-wasting  
463 processes (e.g., debris flows, submarine landslides/slumps, and turbidity currents). The sediment  
464 record of Hg deposition in the BAP of the Western Mediterranean - where sedimentation rates are

465 low ( $< 5 \text{ cm yr}^{-1}$ ) - is disrupted by episodic submarine slumps, transient redox gradients, and  
466 volcanic events. Nevertheless, our Hg sediment profiles, combined with analyses of sediment trap  
467 material recovered at different depths in the water column, allowed us to interpret its geochemical  
468 behavior through the water and sedimentary columns. Our results suggest that Hg deposited onto  
469 the ocean surface is (i) partially re-emitted from the surface waters to the atmosphere, (ii) taken up  
470 by plankton and sequestered mainly through complexation to thiolic functional groups of the  
471 biogenic material, (iii) partially mobilized and methylated in the twilight zone, and (iv) exported  
472 to the seafloor by the settling particulate organic matter. The vertical distributions of Hg,  $C_{\text{org}}$ , and  
473 S, as well as Fe speciation in the sediment, allow us to conclude that (i) a very limited amount of  
474 Hg is sorbed to amorphous Fe oxyhydroxides and, thus, the record of Hg deposition was not  
475 significantly affected by diagenetic remobilization, and (ii) hydrothermal or volcanic sources did  
476 not alter the Hg distribution. Hence, it is reasonable to propose that, in the Western Mediterranean,  
477 Hg is scavenged out of the water column and buried in the sediment as thiolate complexes, which  
478 may be converted to  $\beta\text{-HgS}$  according to the thermodynamically favorable reaction proposed by  
479 Manceau et al. (2015) for oxic soils. The formation of HgSe may further stabilize particulate Hg  
480 under suboxic conditions, as reported in other Mediterranean abyssal sediments (Merceone et al.,  
481 1999). We conclude that in the low  $C_{\text{org}}$  and low sedimentation rate BAP environment, Hg  
482 sedimentary profiles in  $\sim 30 \text{ cm}$  cores are exploitable as chronological records of Hg deposition  
483 during the Late Holocene Period. In brief, owing to negligible diagenetic Hg remobilization and  
484 despite significant smoothing of the temporal variations of the Hg-ARs, the abyssal sediments of  
485 the Western Mediterranean preserve the imprints of major natural and anthropogenic Hg  
486 deposition. The Hg-AR rose from background values of  $0.7 \pm 0.2 \mu\text{g m}^{-2} \text{y}^{-1}$  in sediments  
487 deposited more than 5000 years ago, to  $8.9 \pm 1.4 \mu\text{g m}^{-2} \text{y}^{-1}$  in sediments deposited over the last  
488 century. The geochronological records highlight the imprints of the Iron Age, the Roman Empire,

489 a gradual increase of Hg depositions during the Medieval Period as well as the large contribution  
490 of the Industrial Era.

491 As a semi-enclosed sea, the Mediterranean receives Hg onto its surface waters and transfers it  
492 at depth at a higher rate than in the Pacific Ocean (Munson et al., 2015 and section 4.1.) and,  
493 consequently, its deep-sea sediments are more likely to provide a record of anthropogenic inputs.  
494 In contrast, the deep surficial sediments of the Arctic Ocean, another semi-enclosed sea, fail to  
495 show clear evidence of anthropogenic Hg contamination (Gobeil et al., 1999), although both  
496 systems export Hg to the North Atlantic Ocean (Cossa et al., 2018a; 2018b). This discrepancy most  
497 likely results from the relative strength of local Hg sources, the enhanced efficiency of Hg  
498 ballasting by aggregation of the biogenic carrier phase with Saharan dust, as well as the absence of  
499 significant Hg diagenetic rearrangement on the deep-sea Holocene sediments of the Mediterranean.

500

501

## REFERENCES

- 502 ADIOS (2004) *Atmospheric deposition and Impact of Pollutants, key elements, and nutrients on*  
503 *the open Mediterranean Sea*. Final Report, Section 6: detailed report related to overall project  
504 duration. 93p. European Communities. Contract number: EVK3-CT-2000-00035 Coordinator:  
505 S. Heussner (CNRS, France).
- 506 Ait Brahim Y., Wassenburg J. A., Sha L., Cruz F. W., Deininger M., Sifeddine A., Bouchaou L.,  
507 Spötl C., Edwards R. L. and Cheng H. (2019) North Atlantic Ice-Rafting, Ocean and  
508 Atmospheric Circulation During the Holocene: Insights From Western Mediterranean  
509 Speleothems. *Geophys. Res. Lett.* **46**, 7614-7623.
- 510 Aksentov K. I. and Sattarova V. V. (2020) Mercury geochemistry of deep-sea sediment cores from  
511 the Kuril area, northwest Pacific. *Progr. Oceanogr.* **180**, 102235.

- 512 Angelidis M. O., Radakovitch O., Veron A., Aloupi M., Heussner S., Price B. (2011)  
513 Anthropogenic metal contamination and sapropel imprints in deep Mediterranean sediments.  
514 *Mar. Pollut. Bull.* **62**, 1041-1052.
- 515 Azoury, S., Tronczynski J., Chiffolleau J.-F., Cossa D., Nakhlé K., Schmidt S. and Khalaf G. (2013)  
516 Historical Records of Mercury, Lead, and Polycyclic Aromatic Hydrocarbons Depositions in a  
517 Dated Sediment Core from the Eastern Mediterranean. *Environ. Sci. Technol.* **47**, 7101–7109.
- 518 Azuara J., Sabatier P., Lebreton V., Jalali B., Sicre M. A., Dezileau L., Bassetti M.A., Frigola J.  
519 and Coumbourieu-Nebout N. (2020) Mid- to Late-Holocene Mediterranean climate variability:  
520 Contribution of multi-proxy and multi-sequence comparison using wavelet analysis in the  
521 northwestern Mediterranean basin. *Earth Sci. Rev.* **208**, 103232.
- 522 Bagnato E., Oliveri E., Covelli S., Petranich E., Barra M., Italiano F., Prelo F. and Sprovieri M.  
523 (2017) Hydrochemical mercury distribution and air-sea exchange over the submarine  
524 hydrothermal vents off-shore Panarea Island (Aeolian arc, Tyrrhenian Sea). *Mar. Chem.* **194**,  
525 63-78.
- 526 Bailey N. (2021) Saharan Dust as a Mercury Transport Vector. M.Sc. thesis, Department of  
527 Environment and Geography, University of Manitoba, Winnipeg, Canada.
- 528 Bertine K. K. and Goldberg E. D. (1977) History of Heavy Metal Pollution in Southern California  
529 Coastal Zone-Reprise. *Environ. Sci. Technol.* **11**, 297-299.
- 530 Callender E. (2003) *Heavy Metals in the Environment—Historical Trends*. Treatise on  
531 Geochemistry, Vol. 9.03, 67-105. Turekian K. K., Holland H. D. editors. Elsevier Sciences.
- 532 Cattaneo A., Badhani S., Caradonna C., Bellucci M., Leroux E., Babonneau N., Garziglia S., Poort  
533 J., Akhmanov G. G., Bayon G., Dennielou B., Jouet G., Migeon S., Rabineau M., Droz L. and  
534 Clare M. (2020) The Last Glacial Maximum Balearic Abyssal Plain Megabed revisited. *Geol.*  
535 *Soc. Lond. Sp. Publ.* **500**, 341-357.
- 536 Cooke C. A., Wolfe A. P. and Hobbs W. O. (2009) Lake-sediment geochemistry reveals 1400 years  
537 of evolving extractive metallurgy at Cerro de Pasco, Peruvian Andes. *Geology* **37**, 1019–1022.
- 538 Cooke C. A., Martínez-Cortizas A., Bindler R. and Gustin M. S. (2020) Environmental archives of  
539 atmospheric Hg deposition – A review. *Sci. Total Environ.* **709**, 134800.

- 540 Corella J. P., Valero-Garcés B. L., Wang F., Martínez-Cortizas A., Cuevas C. A. and Saiz-Lopez  
541 A. (2017) 700 years reconstruction of mercury and lead atmospheric deposition in the Pyrenees  
542 (NE Spain). *Atmos. Environ.* **155**, 970–1107.
- 543 Cossa D., Elbaz-Poulichet F. and Nieto J. M. (2001) Mercury in the Tinto-Odiel Estuarine System  
544 (Gulf of Cadiz, Spain): Sources and Dispersion. *Aquat. Geochem.* **7**, 1-12.
- 545 Cossa, D., Averty B. and Pirrone N. (2009) The origin of methylmercury in the open Mediterranean  
546 water column. *Limnol. Oceanogr.* **54**, 837–844.
- 547 Cossa D., Heimbürger L.-E., Sonke J. E., Planquette H., Lherminier P., García-Ibáñez M. I., Pérez  
548 F. F. and Sarthou G. (2018a) Sources, recycling and transfer of mercury in the Labrador Sea  
549 (Geotraces-Geovide cruise). *Mar. Chem.* **198**, 64-69.
- 550 Cossa, D., Heimbürger L.-E., Pérez F. F., García-Ibáñez M. I., Sonke J. E., Planquette H.,  
551 Lherminier P., Boutorh J., Cheize M., Menzel Barraqueta J. L., Shelley R. and Sarthou G.  
552 (2018b) Mercury distribution and transport in the North Atlantic Ocean along the Geotraces-  
553 GA01 transect. *Biogeosciences* **15**, 2309-2323.
- 554 Cossa D., Knoery J., Boye M., Maruszczak N., Thomas B., Courau P. and Sprovieri S. (2020)  
555 Oceanic mercury concentrations on both sides of the Strait of Gibraltar decreased between 1989  
556 and 2012. *Anthropocene* **29**, 100230.
- 557 Crusius J. and Thomson J. (2003) Mobility of authigenic rhenium, silver, and selenium during  
558 postdepositional oxidation in marine sediments *Geochim. Cosmochim. Acta* **67**, 265-273.
- 559 Edgington D. N. and Robbins J. A. (1976) Records of Lead Deposition in Lake Michigan  
560 Sediments Since 1800. *Environ. Sci. Technol.* **10**, 266-274.
- 561 Elbaz-Poulichet, F., Dezileau L., Freydier R., Cossa D. and Sabatier P. (2011) A 3500-year record  
562 of Hg and Pb contamination in a Mediterranean sedimentary archive (the Pierre Blanche  
563 Lagoon, France). *Environ. Sci. Technol.* **45**, 8642-8647.
- 564 Elbaz-Poulichet F., Guédron S., Anne-Lise D., Freydier R., Perrot V., Rossi M., Piot C., Delpoux  
565 S. and Sabatier P. (2020) A 10,000-year record of trace metal and metalloid (Cu, Hg, Sb, Pb)  
566 deposition in a western Alpine lake (Lake Robert, France): Deciphering local and regional  
567 mining contamination. *Quat. Sci. Rev.* **228**, 106076.

- 568 EPA (2007) Method 7473: *Mercury in Solids and Solutions by Thermal Decomposition,*  
569 *Amalgamation, and Atomic Absorption Spectrophotometry* (17 pp).  
570 <https://www.epa.gov/sites/production/files/2015-12/documents/7473.pdf>
- 571 EURACHEM/CITAC (2000) Quantifying uncertainty in analytical measurement. Tech. Rep. Guide  
572 CG4, EU-RACHEM/CITEC, EURACHEM/CITAC Guide. Second edition.
- 573 Feyte S., Tessier A., Gobeil C. and Cossa D. (2010) *In situ* adsorption of mercury, methylmercury  
574 and other elements by iron oxyhydroxides and associated organic matter in lake sediments. *Appl.*  
575 *Geochem.* **25**, 984-995.
- 576 Feyte S., Gobeil C., Tessier A. and Cossa D. (2012) Mercury dynamics in lake sediments *Geochim.*  
577 *Cosmochim. Acta* **82**, 92-112.
- 578 Fitzgerald W. F. and Lamborg C. H. (2005) *Geochemistry of mercury in the environment*. In:  
579 Lollar, B.S. Editor, Environmental Geochemistry. Elsevier–Pergamon, Oxford, pp. 107–148.
- 580 Fitzgerald W. F., Engstrom D. R., Hammerschmidt C. R., Lamborg C. H., Balcom P. H., Lima-  
581 Braun A. L., Bothner M. H. and Reddy C. M. (2018) Global and Local Sources of Mercury  
582 Deposition in Coastal New England Reconstructed from a Multiproxy, High-Resolution,  
583 Estuarine Sediment Record. *Environ. Sci. Technol.* **52**, 7614–7620.
- 584 Garcia-Orellana J., Pates J. M., Masqué P., Bruach J. and Sanchez-Cabeza J. (2009) Distribution  
585 of artificial radionuclides in deep sediments of the Mediterranean Sea. *Sci. Total Environ.* **407**,  
586 887-898.
- 587 Gencarelli C. N., De Simone F., Hedgecock I. M., Sprovieri F. and Pirrone N. (2014) Development  
588 and application of a regional-scale atmospheric mercury model based on WRF/Chem: a  
589 Mediterranean area investigation. *Environ. Sci. Pollut. Res. Int.* **21**, 4095-109.
- 590 Genovesi L., de Vernal A., Thibodeau B., Hillaire-Marcel C., Mucci A. and Gilbert D. (2011)  
591 Recent changes in bottom water oxygenation and temperature in the Gulf of St. Lawrence:  
592 micropaleontological and geochemical evidence. *Limnol. Oceanogr.* **56**, 1319-1329.
- 593 Gobeil C., Macdonald R. W. and Smith J. N. (1999) Mercury profiles in sediments of the Arctic  
594 Ocean basins. *Environ. Sci. Technol.* **33**, 4194-4198.
- 595 Grasby S. E., Sanei, H. and Beauchamp B. (2013) Mercury deposition through the Permo-triassic  
596 Crisis. *Chem. Geol.* **351**, 209-216.

- 597 Guédron S., Amouroux D., Sabatier P., Desplanque C., Develle A.-L., Barre J., Feng, C., Guiter  
598 F., Arnaud F., Reyss J.-L. and Charlet L. (2016) A hundred year record of industrial and urban  
599 development in French Alps combining Hg accumulation rates and isotope composition in  
600 sediment archives from Lake Luitel. *Chem. Geol.* **431**, 10–19.
- 601 Guédron S., Ledru M.-P., Escobar-Torrezd K., Devellee A. L. and Brisseta E. (2018) Enhanced  
602 mercury deposition by Amazonian orographic precipitation: Evidence from high-elevation  
603 Holocene records of the Lake Titicaca region (Bolivia). *Palaeogeogr. Palaeoclimatol.*  
604 *Palaeoeco.* **511**, 577-587.
- 605 Guédron S., Tolu J., Brisset E., Sabatier P., Perrot V., Bouchet S., Develle A. L., Bindler R., Cossa  
606 D. and Fritz S. C. (2019) Late Holocene volcanic and anthropogenic mercury deposition in the  
607 western Central Andes (Lake Chungará, Chile). *Sci. Tot. Environ.* **662**, 903-914.
- 608 Guédron S., Audry S., Acha D., Bouchet S., Point D., Condom T., Heredia C., Campillo S., Baya  
609 P. A., Groleau A., Amice E. and Amouroux D. (2020) Diagenetic production, accumulation and  
610 sediment-water exchanges of methylmercury in contrasted sediment facies of Lake Titicaca  
611 (Bolivia). *Sci. Total Environ.* **723**, 138088.
- 612 Haitzer M., Aiken G. R. and Ryan J. N. (2003) Binding of Mercury(II) to Aquatic Humic  
613 Substances: Influence of pH and Source of Humic Substances. *Environ. Sci. Technol.* **37**, 2436-  
614 2441.
- 615 Hamilton E. L. (1976) Variations of density and porosity with depth in deep-sea sediments. *J.*  
616 *Sediment. Res.* **46**, 280-300.
- 617 Hare, A. A., Stern G. A., Kuzyk Z. Z. A., Macdonald R. W., Johannessen S.L. and Wang F. (2010)  
618 Natural and Anthropogenic Mercury distribution in Marine Sediments from Hudson Bay,  
619 Canada. *Environ. Sci. Technol.* **44**, 5805-5811.
- 620 Heimbürger L. E., Cossa D., Thibodeau B., Khripounoff A., Mas V., Chiffolleau J.-F., Schmidt S.  
621 and Migon C. (2012) Natural and anthropogenic trace metals in sediments of the Ligurian Sea  
622 (Northwestern Mediterranean). *Chem. Geol.* **291**, 141-151.
- 623 Heussner S., Ratti C. and Carbonne J. (1990) The PPS3 sediment trap and trap sample processing  
624 techniques used during the ECOMARGE experiment. *Cont. Shelf Res.* **10**, 943-958.

- 625 Hylander L. D. and Meili M. (2003) 500 years of mercury production: global annual inventory by  
626 region until 2000 and associated emissions. *Sci. Tot. Environ.* **304**, 13-27.
- 627 John S. G. and Conway T. M. (2014) A role for scavenging in the marine biogeochemical cycling  
628 of zinc and cadmium isotopes. *Earth Planet. Sci. Lett.* **394**, 159-167.
- 629 Kassianidou V. and Knapp A. B. (2005) *Archeometallurgy in the Mediterranean: The Social*  
630 *Context of Mining, Technology, and Trade*. Chap. 9. pp. 215-251. In: *The archaeology of*  
631 *Mediterranean prehistory*. Blake E. and A.B. Knapp editors. Blackwell Studies in global  
632 archaeology, Blackwell Publish. 333 p. Oxford, UK. ISBN 0-631-23267-2.
- 633 Kita I., Kojima M., Hasegawa H. et al. (2013) Mercury content as a new indicator of ocean  
634 stratification and primary productivity in Quaternary sediments off Bahama Bank in the  
635 Caribbean Sea. *Quater. Res.* **80**, 606–613.
- 636 Kita I., Yamashita T., Hasegawa H., Sato T. and Kuwahara Y. (2016) Mercury content in Atlantic  
637 sediments as a new indicator of the enlargement and reduction of Northern Hemisphere ice  
638 sheets. *J. Quaternary Sci.* **31**, 167-177.
- 639 Kostka J. E. and Luther G. W. (1994) Partitioning and speciation of solid phase iron in saltmarsh  
640 sediments *Geochim. Cosmochim. Acta* **58**, 1701-1710.
- 641 Kota F. S. (2004) Mercury in chemical fractions of recent pelagic sediments of the Sea of Japan.  
642 *J. Environ. Monit.* **6**, 689-695.
- 643 Lamborg C. H., Fitzgerald W. F., Damman A. W. H., Benoit J. M., Balcom P. H. and Engstrom D.  
644 R. (2002) Modern and historic atmospheric mercury fluxes in both hemispheres: Global and  
645 regional mercury cycling implications. *Global Biogeochem. Cycles* **16**, 1104.
- 646 Liang X., Lu X., Zhao J., Liang L., Zeng E. Y. and Gu B. (2019) Stepwise Reduction Approach  
647 Reveals Mercury Competitive Binding and Exchange Reactions within Natural Organic Matter  
648 and Mixed Organic Ligands. *Environ. Sci. Technol.* **53**, 10685–10694.
- 649 Lim D., Kim J., Xu Z. K., Jeong K. and Jung, H. (2017) New evidence for Kuroshio inflow and  
650 deepwater circulation in the Okinawa Trough, East China Sea: Sedimentary mercury variations  
651 over the last 20kyr. *Paleoceanography* **32**, 571-579.

- 652 Liotta M., Rizzo A., Paonita A., Caracausi A. and Martelli M. (2012) Sulfur isotopic compositions  
653 of fumarolic and plume gases at Mount Etna (Italy) and inferences on their magmatic source,  
654 *Geochem. Geophys. Geosyst.*, **13**, Q05015.
- 655 Mackie E. A. V., Lloyd J. M. and Leng M. J. (2007) Assessment of  $\delta^{13}\text{C}$  and C/N ratios in bulk  
656 organic matter as palaeosalinity indicators in Holocene and Late glacial isolation basin  
657 sediments, northwest Scotland. *J. Quat. Sci.* **22**, 579–591.
- 658 Manceau A., Lemouchi C., Enescu M., Gaillot A. C., Lanson M., Magnin V., Glatzel P., Poulin B.  
659 A., Ryan J. N., Aiken G. R., Gautier-Luneau I. and Nagy K. L. (2015) Formation of Mercury  
660 Sulfide from Hg(II)–Thiolate Complexes in Natural Organic Matter. *Environ. Sci. Technol.* **49**,  
661 9787-9796.
- 662 Martinez-Cortizas A., Pontevedra-Pombal X., Munoz J. N. and García-Rodeja E. (1997) Four  
663 thousand years of atmospheric Pb, Cd and Zn deposition recorded by the ombrotrophic peat bog  
664 of Penido Vello (Northwestern Spain). *Water Air Soil Pollut.* **100**, 387-403.
- 665 Martinez-Cortizas A., Pontevedra-Pombal X., Garcia-Rodeja E., Novoa-Munoz J. C. and Shotyk  
666 W. (1999) Mercury in a Spanish peat bog: archive of climate change and atmospheric metal  
667 deposition. *Science* **284**, 939-942.
- 668 Mason R. P., Choi A. L., Fitzgerald W. F., Hammerschmidt C. R., Lamborg C. H., Soerensen A.  
669 L. and Sunderland E. M. (2012) Mercury biogeochemical cycling in the ocean and policy  
670 implications. *Environ. Res.* **119**, 101-117.
- 671 Mercone D., Thomson J., Croudace I. W. and Troelstra S. R. (1999) A coupled natural  
672 immobilisation mechanism for mercury and selenium in deep-sea sediments  
673 *Geochim. Cosmochim. Acta* **63**, 1481-1488.
- 674 Meyers P. A. (1994) Preservation of elemental and isotopic source identification of sedimentary  
675 organic matter. *Chem. Geol.* **114**, 289–302.
- 676 Mikac N., Niessen S., Ouddane B. and Fisher J.-C. (2000) Effects of Acid Volatile Sulfides on the  
677 Use of Hydrochloric Acid for Determining Solid-Phase Associations of Mercury in Sediments.  
678 *Environ. Sci. Technol.* **34**, 1871-1876.
- 679 Mishra B., Shoenfelt E., Yu Q., Yee N., Fein J. B., Myneni S. C. B. (2017) Stoichiometry of  
680 mercury-thiol complexes on bacterial cell Envelopes. *Chem. Geol.* **464**, 137-146.

681 Moreno T., Higuera P., Jones T., McDonald I. and Gibbons W. (2005) Size fractionation in  
682 mercury-bearing airborne particles (HgPM<sub>10</sub>) at Almadén, Spain: Implications for inhalation  
683 hazards around old mines. *Atmos. Environ.* **39**, 6409-6419.

684 Mucci A., Boudreau B. and Guignard C. (2003) Diagenetic mobility of trace elements in sediments  
685 covered by a flash flood deposit: Mn, Fe and As. *Appl. Geochem.* **18**, 1011-1026.

686 Mucci A., Bernier G. and Guignard C. (2015) Mercury remobilization in Saguenay Fjord (Quebec,  
687 Canada) sediments: Insights following a mass-flow event and capping efficiency. *Appl.*  
688 *Geochem.* **54**, 13-26.

689 Muir D. C. G., Wang X. Yang F., Nguyen N., Jackson T. A., Evans M. S., Douglas M., Köck, G.,  
690 Lamoureux S., Pienitz R., Smol J. P., Vincent W. F. and Dastoor A. (2009) Spatial Trends and  
691 Historical Deposition of Mercury in Eastern and Northern Canada Inferred from Lake Sediment  
692 Cores. *Environ. Sci. Technol.* **43**, 4802-4809.

693 Munson K. M., Lamborg C. H., Swarr G. J. and Saito M. A. (2015) Mercury species  
694 concentrations and fluxes in the Central Tropical Pacific Ocean. *Global Biogeochem. Cycle* **29**,  
695 656-676.

696 Nriagu J. O. (1983) Occupational exposure to lead in ancient times. *Sci. Total Environ.* **31**, 105-  
697 116.

698 Polonia A., Bonatti E., Camerlenghi A., Lucchi R. G., Panieri G. and Gasperini L. (2013)  
699 Mediterranean megaturbidite triggered by the AD 365 Crete earthquake and tsunami. *Sci. Rep.-*  
700 *UK* **3**, 1285.

701 Outridge P. M., Sanei H., Stern G. A., Hamilton P. B. and Goodarzi F. (2007) Evidence for control  
702 of mercury accumulation in sediments by variations of aquatic primary productivity in Canadian  
703 High Arctic lakes. *Environ. Sci. Technol.* **41**, 5259–5265.

704 Outridge P. M., Mason R. P., Wang F., Guerrero S. and Heimbürger-Boavida L. E. (2018) Updated  
705 Global and Oceanic Mercury Budgets for the United Nations Global Mercury Assessment 2018.  
706 *Environ. Sci. Technol.* **52**, 12968–12977.

707 Ravichandran M. (2003) Interactions between mercury and dissolved organic matter, A Review.  
708 *Chemosphere* **55**, 319-331.

- 709 Rees C. E., Jenkins W. J., Monster J. (1978) The sulphur isotopic composition of ocean water  
710 sulphate. *Geochim. Cosmochim. Acta* **42**, 377–381.
- 711 Reimer P. J., Austin W. E. N., Bard E., Bayliss A., Blackwell P. G., Bronk Ramsey C., Butzin M.,  
712 Cheng H., Edwards R. L., Friedrich M., Grootes P. M., Guilderson T. P., Hajdas I., Heaton T.  
713 J., Hogg A. G., Hughen K. A., Kromer B., Manning S. W., Muscheler R., Palmer J. G., Pearson  
714 C., van der Plicht J., Reimer R. W., Richards D. A., Scott E. M., Southon J. R., Turney C. S.  
715 M., Wacker L., Adolphi F., Büntgen U., Capano M., Fahrni S. M., Fogtmann-Schulz A.,  
716 Friedrich R., Köhler P., Kudsk S., Miyake F., Olsen J., Reinig F., Sakamoto M., Sookdeo A.  
717 and Talamo S. (2020) The IntCal20 Northern Hemisphere Radiocarbon Age Calibration Curve  
718 (0–55 cal kBP). *Radiocarbon* **62**, 725-757.
- 719 Rothwell R. G., Hoogakker B., Thomson J., Croudace I. W. and Frenz M. (2006) *Turbidite*  
720 *emplacement on the southern Balearic Abyssal Plain (western Mediterranean Sea) during*  
721 *Marine Isotope Stages 1-3: an application of ITRAX XRF scanning of sediment cores to*  
722 *lithostratigraphic analysis*. Geological Society, London, Special Publications **267**, 79-98.
- 723 Sanei H., Grasby S. E. and Beauchamp B. (2012) Latest Permian mercury anomalies. *Geology* **40**,  
724 63–66.
- 725 Serrano O., Martínez-Cortizas A., Mateo M. A., Biester, H. and Bindler R. (2013) Millennial scale  
726 impact on the marine biogeochemical cycle of mercury from early mining on the Iberian  
727 Peninsula. *Global Biogeochem. Cycles* **27**, 21-30.
- 728 Siani G., Paterne M., Arnold M., Bard E., Métivier B., Tisnerat N. and Bassinot F. (2000)  
729 Radiocarbon Reservoir Ages in the Mediterranean Sea and Black Sea. *Radiocarbon* **42**, 271-  
730 280.
- 731 de Simone F., Gencarelli C. N., Hedgecock I. M. and Pirrone N. (2016) A Modeling Comparison  
732 of Mercury Deposition from Current Anthropogenic Mercury Emission Inventories. *Environ.*  
733 *Sci. Technol.* **50**, 5154-5162.
- 734 Skrobonja A., Gojkovic Z., Soerensen A. L., Westlund P. O., Funk C. and Bjorn E. (2019) Uptake  
735 Kinetics of Methylmercury in a Freshwater Alga Exposed to Methylmercury Complexes with  
736 Environmentally Relevant Thiols. *Environ. Sci. Technol.* **53**, 13757-13766.

- 737 Skyllberg U., Bloom P. R., Qian J., Lin C.-M. and Bleam W. F. (2006) Complexation of  
738 Mercury(II) in Soil Organic Matter: EXAFS Evidence for Linear Two-Coordination with  
739 Reduced Sulfur Groups. *Environ. Sci. Technol.* **40**, 4174-4180.
- 740 Smith J. N. and Loring D. H. (1981) Geochronology for mercury pollution in the sediments of the  
741 Saguenay Fjord, Quebec. *Environ. Sci. Technol.* **15**, 944-951.
- 742 Song Y., Adediran G. A., Jiang T., Hayama S., Björn E. and Skyllberg U. (2020) Toward an  
743 Internally Consistent Model for Hg(II) Chemical Speciation Calculations in Bacterium–Natural  
744 Organic Matter–Low Molecular Mass Thiol Systems. *Environ. Sci. Technol.* **54**, 8094–8103.
- 745 Ternon E., Guieu C., Loÿe-Pilot M.-D., Leblond N., Bosc E., Gasser B., Miquel J.-C. and Martín  
746 J. (2010) The impact of Saharan dust on the particulate export in the water column of the North  
747 Western Mediterranean Sea. *Biogeosciences* **7**, 809–826.
- 748 Terpstra T. T. (2021) Mediterranean silver production and the site of Antas, Sardina. *Oxf. J.*  
749 *Archaeol.* **40**, 176-190.
- 750 Thevenon F., Guédron S., Chiaradia M., Loizeau J.-L. and Poté J. (2011) (Pre-) historic changes  
751 in natural and anthropogenic heavy metals deposition inferred from two contrasting Swiss  
752 Alpine lakes. *Quaternary Sci. Rev.* **30**, 224-233.
- 753 Thibodeau A. M., Ritterbush K., Yager J. A., West A. J., Ibarra Y., Bottjer D. J., Berelson W. M.,  
754 Bergquist B. A. and Corsetti F. A. (2016) Mercury anomalies and the timing of biotic recovery  
755 following the end-Triassic mass extinction: *Nature Com.* **7**, 1–8.
- 756 Thibodeau A. M. and Bergquist B. A. (2017) Do mercury isotopes record the signature of massive  
757 volcanism in marine sedimentary records? *Geology* **45**, 95–96.
- 758 Thomson J., Jarvis I., Green D. R. H., Green, D. A. and Clayton T. (1998) Mobility and immobility  
759 of redox-sensitive elements in deep-sea turbidites during shallow burial. *Geochim. Cosmochim.*  
760 *Acta* **62**, 643–656.
- 761 Tribovillard N., Algeo T. J., Lyons T. and Riboulleau A. (2006) Trace metals as paleoredox and  
762 paleoproductivity proxies: an update. *Chem. Geol.* **232**, 12–32.
- 763 UN-Environment 2019. *Global Mercury Assessment 2018*. United Nation Environmental  
764 Programme, Chemicals and Health Branch, Programme Chemicals and Health Branch Geneva

765 Switzerland. ISBN 978-92-807-3744-8. [https://www.unenvironment.org/resources/publication/](https://www.unenvironment.org/resources/publication/global-mercury-assessment-2018)  
766 [global-mercury-assessment-2018](https://www.unenvironment.org/resources/publication/global-mercury-assessment-2018).

767 USGS (2001) African Dust Causes Widespread Environmental Distress. *Open-File Report 01-246*,  
768 U.S. Geological Survey, July 2001.

769 Žagar D., Sirnik N., Četina M., Horvat M., Kotnik J., Ogrinc N., Hedgecock I. M., Cinnirella S.,  
770 de Simone F., Gencarelli C. N. and Pirrone N. (2014) Mercury in the Mediterranean. Part 2:  
771 processes and mass balance. *Environ. Sci. Pollut. Res.* **21**, 4081–4094.

772 Zhang Y., Jacob D. J., Horowitz H. M., Chen L., Amos H. M., Krabbenhoft D. P., Slemr F., St.  
773 Louis V. L. and Sunderland E.M. (2016) Observed decrease in atmospheric mercury explained  
774 by global decline in anthropogenic emissions. *Proc. Natl. Acad. Sci. U.S.A.* **113**, 526-531.

775 Zúñiga D., Calafat A. Sanchez-Vidal A., Canals M., Price N. B., Heussner S. and Miserocchi S.  
776 (2007a) Particulate organic carbon budget in the open Algero-Balearic Basin (Western  
777 Mediterranean): Assessment from a one-year sediment trap experiment. *Deep-Sea Res. I* **54**,  
778 1530-1548.

779 Zúñiga D., Garcia-Orellana J., Calafat A., Price N. B., Adatte T., Sanchez-Vidal A., Canals M.,  
780 Sanchez-Cabeza J. A., Masque P. and Fabres J. (2007b) Late Holocene fine-grained sediments  
781 of the Balearic Abyssal Plain, Western Mediterranean Sea. *Mar. Geol.* **237**, 25–36.

782

### 783 **Declaration of Competing Interest**

784 The authors declare that they have no known competing financial interests or personal  
785 relationships that could have appeared to influence the work reported in this paper.

786

### 787 **ACKNOWLEDGEMENTS**

788 This work was supported financially by the European Community in the framework of the ADIOS  
789 MAST program (EVK3-CT-2000-00035, Atmospheric deposition and impact of pollutants on  
790 the open Mediterranean Sea). We would like to thank Jean-Francois Hélie and Bassam Ghaleb  
791 at GEOTOP-UQAM for carrying out the total sulfur,  $\delta^{34}\text{S}$  and complementary  $^{210}\text{Pb}$  analyses.  
792 These analyses were subsidized by a Regroupement Stratégique grant from the Fonds Québécois  
793 de Recherche Nature et Technologies (FQRNT) to GEOTOP as well as an NSERC Discovery

794 grant to A.M. We would also like to thank Pascale Occhipinti and Laurent Nectoux for the Hg  
795 analyses performed at the INERIS, and Roselyne Buscail for providing the C and N data. Thanks  
796 are due to Neal Bailey and Feiyue Wang (University of Manitoba, Center for Earth Observation  
797 Science, Winnipeg, Canada) for providing Hg concentration levels in the Saharan dust collected  
798 in the Canary Islands and Cape Verde. The comments of reviewers allowed to improve the  
799 manuscript, their anonymous authors are sincerely thanked.  
800

801

## TABLES

802 *Table 1. Location, water depths of the multicore stations, and sediment core lengths in the Balearic Abyssal*803 *Plain of the Western Mediterranean.*

Station (core)	Latitude N	Longitude E	Depth (m)	Core length (cm)
A	39°28.30'	5°57.37'	2850	22
B	39°29.51'	6°10.88'	2854	32
C	39°18.81'	6°04.22'	2854	30

804

805

806 *Table 2. Mercury concentrations (mean ± standard deviation) in material recovered from sediment traps*807 *deployed at site C (Fig. 1, Table 1) between April 2001 and April 2002. Particulate organic carbon (POC)*808 *data are from Zúñiga et al. (2007a). Water column depth above sediments: 2854 m. Average atmospheric*809 *Hg deposition onto Mediterranean Sea surface waters is ca. 34 ng m<sup>-2</sup> d<sup>-1</sup> (Gencarelli et al., 2014).*

Depth (m)	Hg (ng g <sup>-1</sup> )	C <sub>org</sub> (%)	Hg/C <sub>org</sub> (molar ratio 10 <sup>-6</sup> )	POC flux (mg m <sup>-2</sup> d <sup>-1</sup> )	Hg flux (ng m <sup>-2</sup> d <sup>-1</sup> )
250	127 ± 30	13.4 ± 5.2	0.057	9.9	12.2 ± 8.2
1440	126 ± 19	6.7 ± 2.3	0.112	3.8	8.8 ± 5.5
2820	130 ± 20	5.1 ± 1.3	0.152	2.9	8.6 ± 6.2

810

811

## FIGURE CAPTIONS

812  
813 **Figure 1.** *Sampling location of sediment cores A, B, and C in the Balearic Abyssal Plain of the*  
814 *Western Mediterranean (see also Table 1).*

815 **Figure 2.** *Temporal variation of Hg concentrations in the material recovered from the sediment*  
816 *traps moored at station C between April 2001 and April 2002. Average biogenic content*  
817 *(organic matter, calcium carbonate, and opal) modified from figure 6 in Zúñiga et al. (2007a).*

818 **Figure 3.** *Information logs of sediment cores A, B, and C, showing geological units according to*  
819 *Zúñiga et al. (2007b): Pteropod ooze layers (U2 and U5), foraminifer–pteropod oozes (U1 and*  
820 *U4), and turbidite unit (U3) between 7-13 cm, 9-15 cm, and 8-14 cm, for cores A, B, and C,*  
821 *respectively. See text for details. Note that several multicorer samplings were performed at each*  
822 *site during the R/V Urania cruise in 2001. Hence, core B analyzed in this study is the same as*  
823 *the one described by Angelidis et al. (2011), but different from core B described by Zúñiga et*  
824 *al. (2007b).*

825 **Figure 4.** *Elemental composition of sediment core B.*

826 **Figure 5.** *Total mercury (Hg), Hg accumulation rate (Hg-AR), and Hg:C<sub>org</sub> ratio profiles in*  
827 *sediment cores A, B, and C.*

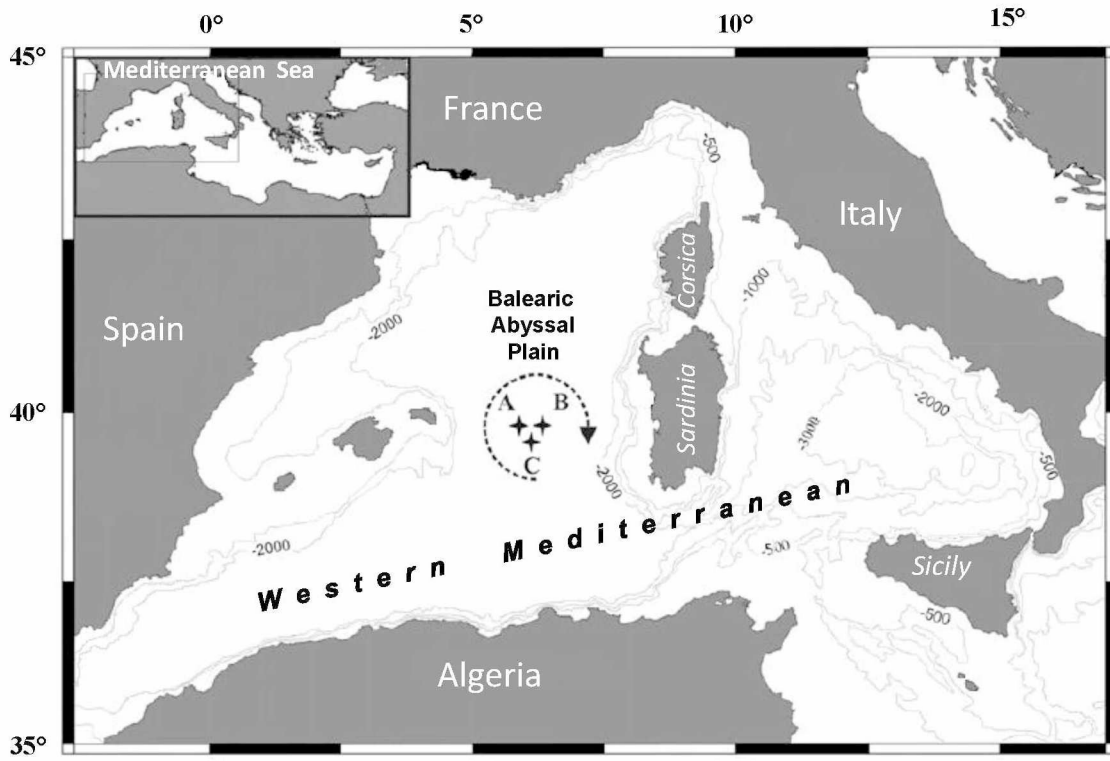
828 **Figure 6.** *Mercury (Hg) versus sulfur (S) concentrations in core B. The Hg:S ratio profile in*  
829 *sediment core B is given in the insert.*

830 **Figure 7.** *Hg accumulation rates (Hg-AR) for marine, lacustrine, and mire sediment historical*  
831 *records. Records are presented according to their geographical location from west to east*  
832 *following the trade wind direction (westerlies) from bottom to top: Penido Vello mire (Spain,*  
833 *Martínez-Cortizas et al., 1999), Portlligat Bay marine sediment (Spain, Serrano et al., 2013),*  
834 *cores A, B, and C marine sediment from the Balearic Abyssal plain (this study), and two*  
835 *headwater catchment lake records from the western (Robert, France, Elbaz-Poulichet et al.,*  
836 *2020) and central Alps (Meidsee, Switzerland, Thevenon et al., 2011).*

837

838

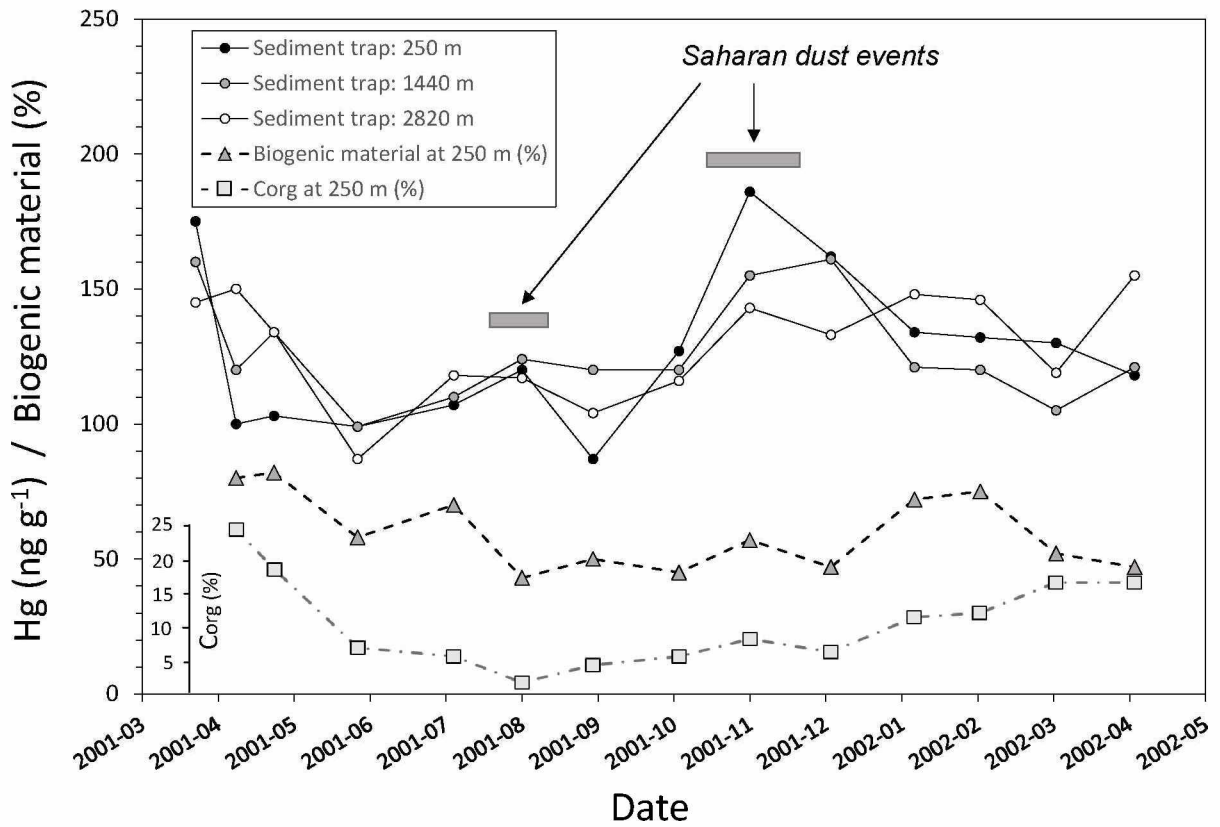
839



840

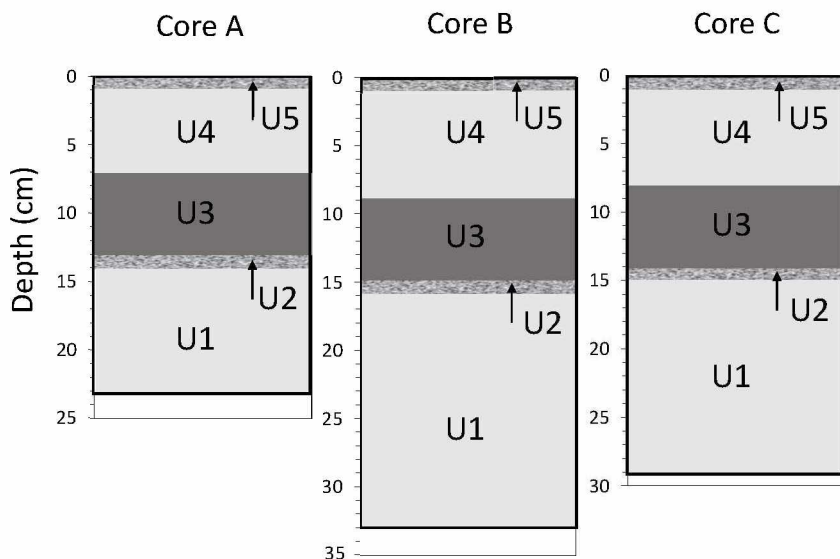
841 Fig. 1

842



843

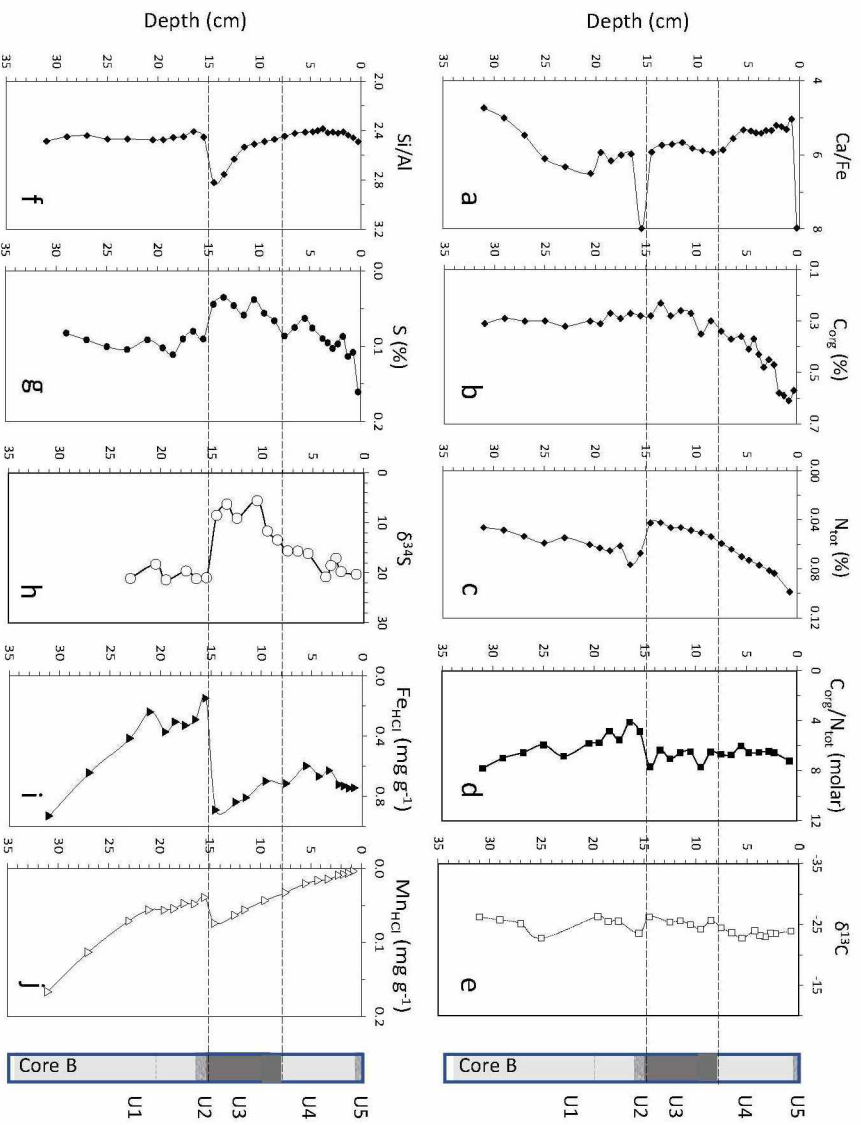
844 Fig. 2



845

846 Fig. 3

847

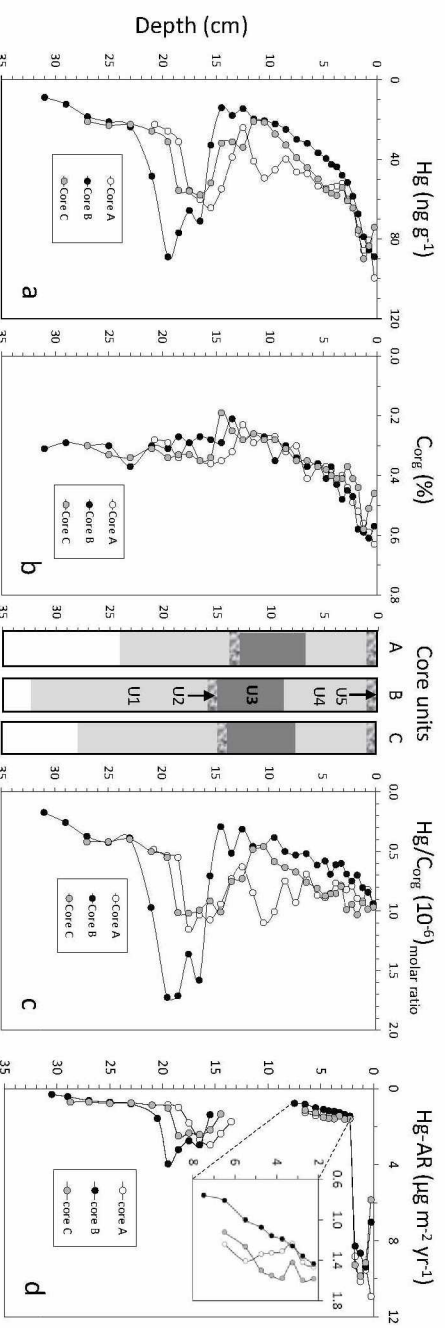


848

849 Fig. 4

850

851

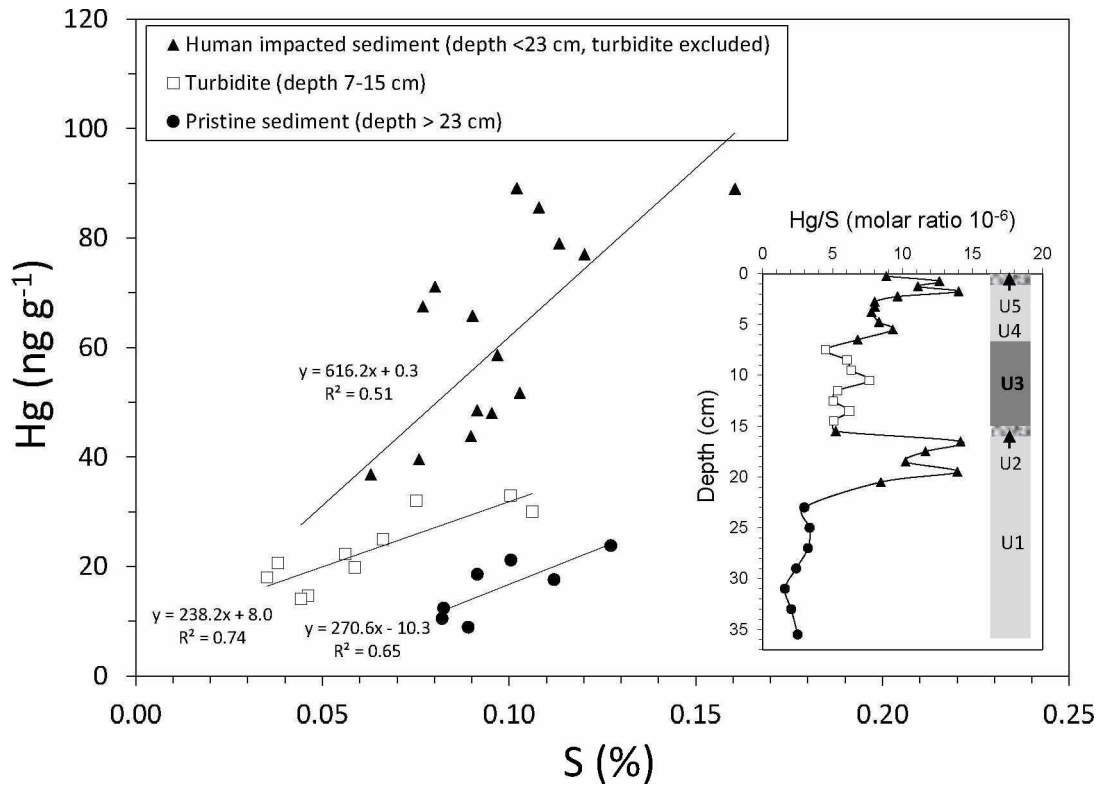


852

853 Fig. 5

38

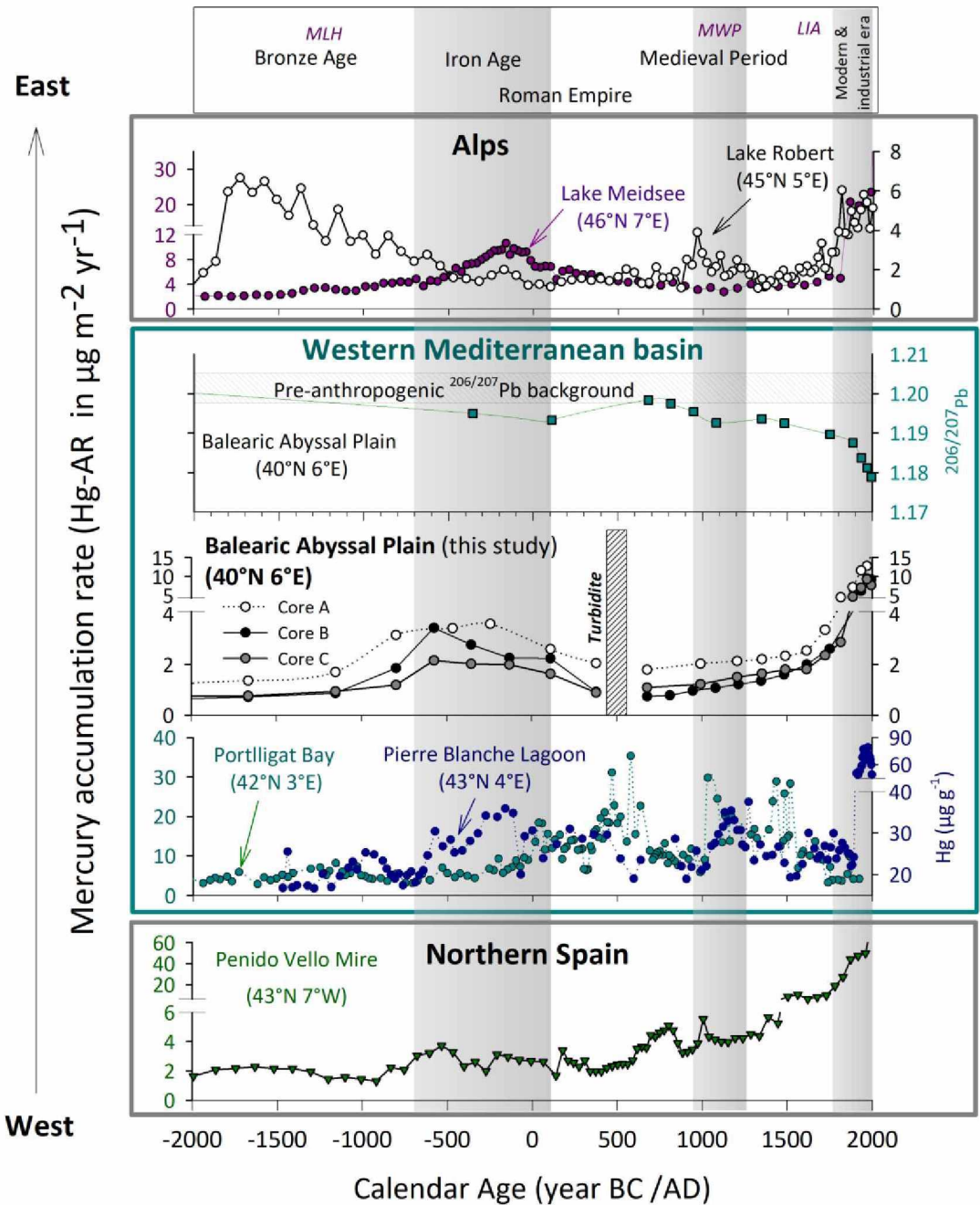
854



855

856 Fig. 6

857



858

859 Fig. 7

1 *Running title: Hg in abyssal Western Mediterranean sediments*

2 **Changes highlighted in yellow**

3 **Mercury accumulation in the sediment of the Western Mediterranean abyssal**  
4 **plain: A reliable archive of the late Holocene**

5 Cossa, D.<sup>1,2\*</sup>, Mucci A.<sup>3</sup>, Guédron S.<sup>1</sup>, Coquery M.<sup>4</sup>, Radakovich O.<sup>5,6</sup>, Escoube R.<sup>2,7</sup>, Campillo,  
6 S.<sup>1</sup>, Heussner, S.<sup>8</sup>

7 <sup>1</sup>*Université Grenoble Alpes, ISTERre, CS 40700, F-38058 Grenoble Cedex 9, France*

8 <sup>2</sup>*IFREMER, Atlantic Center, LBCM, F-44031 Nantes, France*

9 <sup>3</sup>*Geotop and Department of Earth and Planetary Sciences, McGill University, 3450 University St.,*  
10 *Montreal, QC, H3A 0E8 Canada*

11 <sup>4</sup>*INRAE, UR RiverLy, 5 rue de la Doua CS 20244, F-69625 Villeurbanne, France*

12 <sup>5</sup>*IRSN (Institut de Radioprotection et de Sécurité Nucléaire), PSE-ENV/SRTE/LRTA, F-13115 Saint-Paul-*  
13 *lès-Durance, France.*

14 <sup>6</sup>*Aix Marseille Université, CNRS, IRD, INRAE, Coll France, CEREGE, F-13545 Aix-en-Provence, France*

15 <sup>7</sup>*Université de Lyon, ESN Lyon, Earth Sciences Department, BP 7000, F-69342 Lyon Cedex 07, France*

16 <sup>8</sup>*Univeristé de Perpignan Via Domitia, CEFREM, UMR 5110, F-66860 Perpignan Cedex, France*

17 *\*Corresponding author: dcossa@ifremer.fr*

18

19

20 **Abstract**

21 **Temporal reconstruction of Hg deposition from sediment archives is relatively straightforward**

22 **in organic-rich or high sedimentation rate environments, such as lakes and ocean margins. To**

23 **retrieve long-term records at regional or global scales, deep-sea sediments are more appropriate,**

24 **but such records are scarce and their reliability has been questioned because of possible post-**

25 **depositional Hg diagenetic remobilization. Here, we investigated the accumulation of Hg in the**

26 **Balearic Abyssal Plain (2850 m deep) of the Western Mediterranean through a comprehensive**

27 **characterization of the chemical and isotopic composition (organic carbon, nitrogen, sulfur, major**

28 **and redox-sensitive elements) of sediment trap material and sediment cores. The analysis of**

29 **material collected in the sediment traps, deployed at 250, 1440, and 2820 m, indicates that Hg is**

30 **(i) partially re-emitted to the atmosphere and mobilized in the twilight zone and that (ii) the Hg**

31 downward flux depends on the primary production in surface waters, suggesting that organic matter  
32 (OM) acts as the main Hg-carrier phase. As the Hg concentrations of material collected in the traps  
33 vary little with depth but the Hg:C<sub>org</sub> ratio of the settling particulate matter decreases with depth,  
34 Hg must be re-adsorbed onto the more refractory fraction of the settling OM. Results of selective  
35 chemical extractions of the sediment indicate that Hg is very weakly coupled to the iron cycle but  
36 strongly associated with sulfur, supporting the assumption that its vertical distribution was only  
37 weakly altered by diagenetic remobilization. In addition, the distributions of S and  $\delta^{34}\text{S}$  in the  
38 sedimentary column exclude the possibility that local volcanism impacted on Hg enrichment of the  
39 sediments. Accordingly, a reconstruction of Hg accumulation rates (Hg-AR) during the Late  
40 Holocene is readily achieved. Biological mixing and smoothing of the sediment record, as revealed  
41 by the distribution of radionuclides in surface sediments, was considered in the interpretation of  
42 the Hg-AR record. The first anthropogenic Hg signal recorded in the studied cores corresponds to  
43 the Iron Age and the Roman Empire period, as Hg-ARs rose from the baseline ( $0.7 \pm 0.2 \mu\text{g m}^{-2}$   
44  $\text{yr}^{-1}$ ) to an average value of  $2.2 \pm 0.5 \mu\text{g m}^{-2} \text{yr}^{-1}$ . The Hg-ARs return to baseline values at the  
45 decline of the Roman Empire, display a small increase during the Medieval Period ( $1.5 \pm 0.5 \mu\text{g}$   
46  $\text{m}^{-2} \text{yr}^{-1}$ ), increase abruptly at the onset of the Industrial Era, leading to a ~10-fold increase in Hg  
47 deposition in the last 120 years ( $8.9 \pm 1.4 \mu\text{g m}^{-2} \text{yr}^{-1}$ ), and retreat progressively over the past 50  
48 years.

49

50 *Keywords:* Mercury, Abyssal sediment, Holocene, Western Mediterranean

51

52

## 1. INTRODUCTION

53 Aquatic sediments can provide a record of trace element deposition from atmospheric and  
54 riverine sources, including evidence of natural and anthropogenic forcing (Bertine and Goldberg,  
55 1977; Callender, 2003; Tribovillard et al., 2006). Historical reconstructions of trace element  
56 deposition from sediment archives are relatively straightforward if the element is not subject to  
57 strong diagenetic remobilization, of which Hg is a good example at least in organic-rich or high  
58 sedimentation rate environments such as lakes and marine coastal zones (Edgington and Robbins,  
59 1976; Smith and Loring, 1981; Fitzgerald et al., 2018; Guédron et al., 2016). Natural sources of  
60 Hg to sediments are mainly from atmospheric and submarine volcanism, wildfires, and low-  
61 temperature volatilization from soils and some continental rocks (Fitzgerald and Lamborg, 2005;  
62 Mason et al., 2012). Anthropogenic Hg sources include high-temperature processes (fossil fuel and  
63 biomass burning, municipal waste incineration, etc.), mining activities, deforestation/erosion,  
64 industrial processes, and past domestic uses (Outridge et al., 2018; UN-Environment, 2019).  
65 Variations of Hg accumulation rates (Hg-AR) from natural and anthropogenic sources have been  
66 reported in sediment cores. The volcanic origin of Hg in sediments of the Triassic-Jurassic Muller  
67 Canyon (Nevada, USA) (Thibodeau et al., 2016; Thibodeau and Bergquist, 2017) and Permian  
68 Buchanan Lake (Canada) (Sanei et al., 2012) was well illustrated, whereas seafloor hydrothermal  
69 activity was revealed by elevated Hg concentrations in Holocene sediments of the northwestern  
70 Pacific (Lim et al., 2017). The impact of climate on Hg deposition, in response to changes in  
71 precipitation or biological productivity, has been identified in lakes and marine sediments  
72 (Outridge et al., 2007; Grasby et al., 2013; Kita et al., 2013, 2016; Guédron et al., 2018). Sediment  
73 records of anthropogenic Hg deposition in freshwater lakes as well as near-shore and ocean margin  
74 environments are numerous and have been used to document increases in global or local sources

75 (Cossa et al., 2001; Muir et al., 2009; Hare et al., 2010; Mucci et al., 2015). Several studies  
76 underscore the rapid increase in Hg deposition starting at the beginning of the Industrial Era, i.e.,  
77 after AD 1850 (Azoury et al., 2013; Fitzgerald et al., 2018; Cooke et al., 2020). Enhanced Hg-ARs,  
78 linked to pre-industrial human activities, have been documented in strata of a Mediterranean lagoon  
79 sediment core dated to before ~AD 1850 (Elbaz-Poulichet et al. 2011). These authors highlighted  
80 two periods of increasing Hg deposition: the Middle Age, probably due to deforestation and  
81 biomass burning, and the XVI-XVII<sup>th</sup> Centuries, most likely associated with the increase in Hg  
82 mining activities resulting from the development of the Hg amalgamation process for the recovery  
83 of silver and gold. Evidence of (pre-)historical anthropogenic Hg emissions has also been identified  
84 in lake sediments (Thevenon et al., 2011; Guédron et al., 2016; Cooke et al., 2009; Corella et al.,  
85 2017), including those associated with mining and metal treatment during the Bronze and Iron  
86 Ages (Elbaz-Poulichet et al., 2020). These results bolster the adequacy of aquatic sediments as  
87 geochronological records of Hg deposition.

88 Deep-sea sediments are of particular interest in this context since, given their slow  
89 accumulation rates, they can potentially provide an entire record of Holocene deposition even in  
90 short cores. Episodic depositional events (e.g., mass-wasting) or/and changes in redox conditions  
91 in response to a gradual or sudden modification of the sedimentation regime may, however, modify  
92 the sedimentary records of multivalent elements (Thomson et al., 1998; Crusius and Thomson,  
93 2003). Mercury remobilization was documented at the oxic/suboxic boundary in deep-sea  
94 sediments where oxidation of pre-existing sulfides occurred (Mercone et al., 1999). Furthermore,  
95 chemical gradients across or near the sediment-water interface (SWI) can trigger a post-  
96 depositional redistribution of trace elements. Mercury enrichment at, or slightly below, the  
97 sediment-water interface (SWI) as well as downcore-decreasing concentrations were observed in

98 Arctic deep-sea sediments (Gobeil et al., 1999). Whereas increased anthropogenic Hg deposition  
99 was considered, the authors underlined that these profiles resulted from early diagenetic  
100 rearrangements of Hg in response to its affinity for authigenic Fe-oxyhydroxides that accumulate  
101 in the oxic layer. The effect of diagenetic remobilization was promoted by active bioturbation and  
102 low sedimentation rates, sedimentary conditions that are common to abyssal environments. In  
103 pelagic sediments of the Sea of Japan, Hg distributions display peaks near the SWI as well as in  
104 buried, brown “oxidized” sediment layers, also suggesting redox-driven diagenetic Hg  
105 redistribution (Kota, 2004). Conversely, in the sediment of the trench system and adjacent abyssal  
106 plain off the Kuril Islands, Hg burial is governed by atmospheric deposition and biological  
107 productivity. A Hg profile at this site, recording the last 120 years of deposition, features a  
108 maximum Hg flux corresponding to the second part of the XX<sup>th</sup> Century (Aksentov and Sattarova,  
109 2020). Irrespective, biological mixing (bioturbation and bioirrigation) can smooth the sediment  
110 records resulting from marked changes in Hg deposition rates. To sum up, records of Hg  
111 accumulation in deep-sea sediments have been shown to reflect the chronology of paleo and (pre-  
112 )historical Hg deposition, but post-depositional Hg redistribution cannot be ruled out.

113 High-resolution vertical profiles of Hg concentrations were determined in three ~30-cm  
114 sediment cores recovered from the Balearic Abyssal Plain (BAP), covering the Late Holocene  
115 Period, in the Western Mediterranean (Fig. 1). These data, combined with analyses of settling  
116 particulate material collected at various depths in the water column, allowed us to interpret the Hg  
117 sedimentary records in terms of post-depositional dynamic and depositional chronology. Results  
118 show that post-depositional remobilization of Hg is minor and that, despite significant biological  
119 mixing, the Hg accumulation rates record the impact of the Iron Age, the Roman Empire, and the  
120 onset of the Industrial Era.

121

122

## 2. MATERIAL AND METHODS

### 123 *2.1. Sampling*

124 Undisturbed sediment cores (24-33 cm long) were obtained from three stations (A, B, C),  
125 roughly 25 km apart from each other, in the BAP (also called Algero-Balearic or Algero-Provencal  
126 Basin) of the Western Mediterranean Basin during a cruise onboard the R/V Urania in March 2001  
127 (Fig. 1, Table 1). Cores were collected using a Wuttke-type multicorer and treated on-board  
128 immediately after recovery. Each core was sliced at 0.5 cm intervals over the first 5 cm, at 1 cm  
129 intervals from 5 to 20 cm, and at 2 cm intervals from 20 cm to the bottom.

130 At station C, three sediment traps (Technicap®, 0.125 m<sup>2</sup> diameter) were deployed along a  
131 mooring line at 250, 1440, and 2820 m depth, allowing the collection of 14 samples from each trap  
132 between April 2001 and April 2002 (Heussner et al., 1990; Zúñiga et al., 2007a). The samples were  
133 frozen immediately upon recovery, then freeze-dried, homogenized, and sub-sampled for various  
134 subsequent chemical analyses. Detailed descriptions of the cores and trapped material are given in  
135 the project final report (ADIOS, 2004).

### 136 *2.2. Chemical analyses*

137 Total Hg analyses were performed using an automatic atomic absorption spectrophotometer  
138 (AAS; Altec®, model AMA-254), according to the protocol described by EPA (2007). Briefly,  
139 weighed aliquots of freeze-dried sediment were introduced into the analytical system where they  
140 were heated to 550°C. The volatilized Hg was carried by a stream of oxygen to a gold trap onto  
141 which Hg was concentrated by amalgamation, before being thermally dissociated and analyzed by  
142 atomic absorption spectrometry. The detection limit was 7 ng g<sup>-1</sup>, calculated as 3.3 times the  
143 standard deviation of the blanks. We used a marine sediment certified reference material (CRM)

144 (MESS-2 from the National Research Council of Canada) to ensure the accuracy of the analyses;  
145 the mean value obtained ( $92 \pm 2 \text{ ng g}^{-1}$ ) was always within the range of the certified value:  $92 \pm 9$   
146  $\text{ng g}^{-1}$ . The reproducibility, defined as the coefficient of variation of six replicate analyses of the  
147 same CRM was 1.8 %. The analytical uncertainty (EURACHEM/CITAC, 2000) is  $\sim 10$  %. Labile Fe  
148 (and associated Hg) concentrations were estimated upon partial dissolution of the sediment with  
149 buffered ascorbate (pH 8.0) and dilute HCl (0.5 M) solutions according to protocols described by  
150 Kostka and Luther (1994). The ascorbate extraction is believed to dissolve only amorphous oxides,  
151 whereas the HCl extraction dissolves carbonates, crystalline Fe-oxyhydroxides, and acid volatile  
152 sulfides (AVS). It should be noted that the 0.5 M HCl extraction does not dissolve HgS (Mikac et  
153 al., 2000). To avoid losing the  $\text{Hg}^0$  formed during the ascorbate extraction, the sample was not  
154 stirred continuously during the 24 h extraction, as the original protocol prescribes, but gently mixed  
155 a few times, and the resulting solution was analyzed immediately after the extraction and  
156 centrifugation.

157 The activities of  $^{210}\text{Pb}$  in these cores were measured by alpha spectrometry of its daughter  
158 product  $^{210}\text{Po}$  (see details in Angelidis et al., 2011). An additional set of  $^{210}\text{Pb}$  activities were also  
159 obtained to refine the age-depth model between 13 and 20 cm in core B. They were acquired  
160 indirectly from the freeze-dried sediments by measuring the decay rate of its daughter isotope  $^{210}\text{Po}$   
161 by alpha spectrometry at the GEOTOP-UQAM Geochronology Laboratory. Uncertainties were  
162 estimated as two standard deviations (2s) for counting statistics, which is 4-8 % of the value  
163 obtained. A detailed description of the method can be found in Genovesi et al. (2011).

164 The total sulfur (S) and sulfur isotopic ratio ( $^{34}\text{S}:^{32}\text{S}$ ) of the solids were measured on an  
165 Isoprime model VisIon isotope ratio mass spectrometer coupled to an Elementar Vario PyroCube  
166 elemental analyzer running in continuous flow mode at the Geotop-UQAM Light Stable Isotope  
167 Geochemistry Laboratory. The freeze-dried and crushed sediment samples were weighted in tin

168 cups to obtain similar amounts of SO<sub>2</sub> for all samples and reference materials. The elemental  
169 analyzer was calibrated against known amounts of sulfanilamide. Two internal reference materials  
170 (IAEA-S2 & IAEA-S3;  $\delta^{34}\text{S} = +22.62 \pm 0.16 \text{ ‰}$ , and  $\delta^{34}\text{S} = -32.49 \pm 0.16 \text{ ‰}$ , respectively) were  
171 used to normalize the isotope ratios to the Vienna-Canyon Diablo Troilite (*VCDT*). A third  
172 reference material (IAEA-S1;  $\delta^{34}\text{S} = -0.3 \pm 0.00 \text{ ‰}$ ) was analyzed as an unknown to assess the  
173 exactness of the normalization. Results are reported in delta units ( $\delta$ ) in ‰ vs VCDT. The overall  
174 analytical uncertainty (2s), based on the propagation of uncertainties of the normalization of the  
175 internal reference materials and the samples, is better than  $\pm 0.2 \text{ ‰}$ , but it does not account for the  
176 homogeneity nor the representativity of the sample. Total sulfur concentrations and  $\delta^{34}\text{S}$  values  
177 were corrected for the porewater sulfate contributions, using porosity values (Suppl. Info., Table  
178 S1) and assuming  $[\text{SO}_4^{2-}]$  was  $0.0282 \text{ mole kg}^{-1}$  and a 21 ‰ VCDT value for the modern ocean  
179  $\delta^{34}\text{S-SO}_4^{2-}$  (Rees et al., 1978).

180 Major elements were analyzed by X-ray fluorescence spectrometry and results were published  
181 earlier (Angelidis et al., 2011). Total organic carbon ( $\text{C}_{\text{org}}$ ) content and its isotopic composition  
182 ( $\delta^{13}\text{C}_{\text{org}}$ ) were measured, after decarbonation (Suppl. Info., S1.2), by Cavity Ring-Down  
183 Spectrometry (Picarro Inc.<sup>®</sup>) coupled to a Combustion Module (Costech Inc.<sup>®</sup>) (CM-CRDS) using  
184 previously reported analytical methods, calibration and sample preparation (Guédron et al., 2019  
185 and references therein).

### 186 2.3. Age model and Hg accumulation rate calculation

187 The Hg-ARs within the 3 cores were obtained after computation of an age-depth model based  
188 on the <sup>210</sup>Pb activity data and the four radiocarbon ages reported in core C by Zúñiga et al. (2007b).  
189 The age-depth model was derived using the IntCal20 calibration curve (Reimer et al., 2020) with  
190 consideration of the marine reservoir [ $R(t) = 390 \pm 85 \text{ y BP}$ ] age of the Mediterranean Sea (Siani

191 et al., 2000). Details of the derivation of the age-depth model can be found in Suppl. Info. (SI.3).

192 Hg-ARs were computed with consideration of the sediment compaction following the equation:

$$193 \quad \text{Hg-ARs} = 10 * [\text{THg}] * \text{SR} * (1 - \phi) * d \quad (1)$$

194 where [THg] is the Hg concentration ( $\text{ng g}^{-1}$ , Fig. 5a), SR the sedimentation rate ( $\text{cm yr}^{-1}$ , Suppl.

195 Info., SI.3),  $\phi$  the porosity of the sediment (Suppl. Info., Table S1), and d the average grain

196 sediment density,  $2.65 \text{ g cm}^{-3}$  according to Hamilton et al. (1976).

197

198

### 3. RESULTS

#### 199 **3.1. Sediment traps**

200 The Hg and  $C_{\text{org}}$  concentrations of the particulate material collected by the sediment traps at

201 Station C are reported in Table 2. Year-long Hg records displayed similar seasonal variations,

202 irrespective of the trap/sampling depth, with the highest concentrations in spring and autumn, and

203 the lowest in summer (Fig. 2). Interesting to note are the relatively high Hg concentrations during

204 the Saharan dust events identified in July and November 2001 (ADIOS, 2004). Most striking are

205 the nearly constant, mean particulate Hg concentrations throughout the water column (averaging

206  $128 \pm 23 \text{ ng g}^{-1}$ ,  $n = 42$ ) whereas mean  $C_{\text{org}}$  concentrations decreased by a factor of  $\sim 3$  between 250

207 and 2820 m depth (Table 2). In other words, the Hg concentrations in settling particles remain the

208 same during their transit through the water column while particulate organic carbon is

209 remineralized or dissolved. Accordingly, the Hg: $C_{\text{org}}$  molar ratios increased from 0.06 to  $0.15 \times 10^{-6}$

210 between 250 and 2820 m.

#### 211 **3.2. Sediment cores**

##### 212 **3.2.1 Sedimentary facies and geological settings**

213 Several cores sampled at stations A, B, and C in the BAP during the same cruise (ADIOS,  
214 2004) were described in two previous publications: one includes a description of their sequence  
215 stratigraphy and sediment lithology (Zúñiga et al., 2007b), whereas the other focusses on their trace  
216 element (Cu, Cd, Pb, Zn) composition (Angelidis et al., 2011). All the cores cover the Late  
217 Holocene Period and consist mainly of yellowish-brown, calcareous pelitic muds. They comprise  
218 five units (Fig. 3) referred to as U1 to U5 from the bottom to the top: two foraminifer-pteropod  
219 oozes (U1 and U4), two pteropod ooze layers (U2 and U5), and a turbidite deposit (U3). According  
220 to Zúñiga et al. (2007b), U3 is a zeolite-rich turbidite that likely originated from pyroclastic  
221 deposits derived from the Sardinian continental margin. For the three cores investigated in this  
222 study, U1 extended from the bottom of the cores to 14-16 cm below the sediment surface, whereas  
223 U5 occupied the top centimeter. The position of the other units in the sedimentary column varied  
224 slightly depending on the core: U2 was a 1-cm thick unit located between 13 and 16 cm from the  
225 surface, U3 was ~6-cm thick and found between 6 and 15 cm from the surface (7-13 cm, 9-15 cm,  
226 and 8-14 cm, for cores A, B, and C, respectively), and U4 was 6-8 cm thick and sat between 1 and  
227 9 cm from the surface (Fig. 3).

### 228 3.2.2 *Elemental distribution in the sedimentary column*

229 At station B, the elemental composition of one core was determined to detail the chemo-  
230 stratigraphy of the sedimentary column (Fig. 4). Two notable features appear (i) high Ca/Fe values  
231 in U2 and U5, and (ii) a spike in Si/Al at the U2-U3 boundary (Fig. 4a, f). The first feature is  
232 coincident with a positive excursion of the CaCO<sub>3</sub> content (Suppl. Info., Fig. S3) which reflects the  
233 abundance of pteropods in units U2 and U5, whereas the Ca/Fe distinguishes turbidites from  
234 pelagites because of the higher Fe and lower Ca contents of turbidites in the BAP (Rothwell et al.,  
235 2006). On the other hand, high Si/Al and K/Al (Fig. 4f and Suppl. Info., Fig. S3) clearly indicate

236 the presence of a lithogenic layer that characterizes the turbiditic layer (U3) (Zúñiga et al., 2007b).  
237 Below the turbidite unit, several parameters abruptly increase, namely  $N_{\text{tot}}$  (and associated  $C_{\text{org}}/N_{\text{tot}}$   
238 decrease),  $\delta^{13}\text{C}_{\text{org}}$ , S, and  $\delta^{34}\text{S}$  (Fig. 4c, e, g, and h), whereas, HCl-extractible Fe and Mn decrease  
239 sharply (Fig. 4i and j). The  $C_{\text{org}}:N_{\text{tot}}$  molar ratios (<8) and  $\delta^{13}\text{C}_{\text{org}}$  (>-25‰) indicate that the  
240 sedimentary organic carbon is mostly of marine (algal) origin (Meyers, 1994; Mackie et al., 2007).  
241 The  $\delta^{34}\text{S}$  values in units U1, U2, U4, and U5 are close to the modern seawater value (~21 ‰), with  
242 lower values (<10 ‰) in unit U3 (Fig. 4g). The sharp, positive gradient of  $\text{Fe}_{\text{HCl}}$  and  $\text{Mn}_{\text{HCl}}$   
243 concentrations at the interface of the U2-U3 units suggests that some Fe and Mn remobilization  
244 has occurred at this level despite the current oxic or suboxic redox conditions throughout the core  
245 ( $E_{\text{h}} > 180$  mV, ADIOS, 2004). This gradient most likely developed (temporary suboxic or anoxic  
246 conditions in response to the respiration of fresh OM at the SWI) in response to the turbidite (U3)  
247 depositional event, which buried the former SWI, as previously suggested by Zúñiga et al. (2007b).  
248 The S and  $\delta^{34}\text{S}$  sediment profiles (Fig. 4g and h) exhibit a slight decrease within the turbidite unit,  
249 a distinctive characteristic of the hosting zeolite mineral, an alteration product of volcanic material  
250 (Zúñiga et al., 2007b). A magmatic origin argues for low  $\delta^{34}\text{S}$  values (Liotta et al., 2012).

### 251 3.2.3 Mercury distribution in the sedimentary column

252 Mercury profiles in the three sediment cores are shown in figure 5a. The Hg concentrations  
253 varied from 9 to 100 ng g<sup>-1</sup>, with the highest values observed within the first 2 cm of the SWI and  
254 the lowest values at the bottom of the cores. The three Hg profiles exhibited the same vertical  
255 distribution patterns, characterized by an exponential decrease of Hg concentrations from the  
256 surface to the bottom of the cores, interrupted by a broad bump between 12 and 22 cm. These  
257 bumps reach 64, 89, and 58 ng g<sup>-1</sup> in cores A, B, and C, respectively. Mercury concentrations  
258 covary with  $C_{\text{org}}$  ( $R^2 = 0.52$ ,  $n = 81$ ,  $p < 0.01$ ). Notwithstanding the bumps (between 12-22 cm) over

259 which the Hg:C<sub>org</sub> molar ratios reach their highest value, the ratios decrease from  $\sim 1 \times 10^{-6}$  at the  
260 sediment surface down to  $0.17 \times 10^{-6}$  at the bottom (Fig. 5c).

261 Vertical profiles of Hg-AR exhibited similar patterns for the 3 cores, with the lowest average  
262 Hg-AR values ( $0.7 \pm 0.2 \mu\text{g}\cdot\text{m}^{-2}\cdot\text{yr}^{-1}$ ) in the basal unit (depth > 23 cm in U1) (Fig. 5d). The Hg-  
263 AR background in marine sediments is poorly documented (see review by Cooke et al., 2020), but  
264 our minimum value is of the same order of magnitude as the background Hg-AR (ca.  $1\text{-}2 \mu\text{g}\cdot\text{m}^{-2}\cdot\text{yr}^{-1}$ )  
265 recorded in various sediment archives (Lamborg et al., 2002; Serrano et al., 2013; de Simone  
266 et al., 2016; Cooke et al., 2020). Above 23 cm in U1, Hg-ARs increase up to 3.20, 3.95, and 2.47  
267  $\mu\text{g}\cdot\text{m}^{-2}\cdot\text{yr}^{-1}$  in core A, B, and C respectively, followed by a rapid decline in U4 above the turbidite  
268 (averaging  $1.0 \pm 0.2 \mu\text{g}\cdot\text{m}^{-2}\cdot\text{yr}^{-1}$  for the 3 cores). In U4, a low-amplitude “shoulder” is also visible  
269 between 3.5 and 6 cm in cores A and C (Fig. 5c, insert). Finally, the highest Hg-ARs ( $8.9 \pm 1.4$   
270  $\mu\text{g}\cdot\text{m}^{-2}\cdot\text{yr}^{-1}$ ) are observed in the surface unit (U5), which includes the last  $\sim 120$  years of deposition  
271 and is affected by mixing processes (Angelidis et al., 2011).

272

273

## 4. DISCUSSION

### 4.1. Mercury transfer from the atmosphere to the sediment

275 Despite the semi-enclosed nature of the Mediterranean Sea, the main Hg input to the open  
276 surface waters is, by far, from atmospheric deposition (e.g., Žagar et al., 2014). Little is known  
277 about the contributions of continental and hydrothermal inputs, except that mass-wasting events  
278 may reach the BAP (e.g., Cattaneo et al., 2020) and that hydrothermal fluxes, mostly located in the  
279 Tyrrhenian Sea, are rapidly transferred to the atmosphere (Bagnato et al., 2017). According to the  
280 data presented in Table 2, only 35 % of the atmospheric deposition flux ( $\sim 34 \text{ ng m}^{-2} \text{ d}^{-1}$  according

281 to Gencarelli et al., 2014) is found in large particles collected in the 250-m deep sediment trap.  
282 Hence, these observations suggest that a significant (~65 %) amount of the Hg is re-emitted to the  
283 atmosphere, in agreement with results of global air-sea exchange oceanic budgets and models (e.g.,  
284 Mason et al., 2012).

285 The Hg flux associated with settling particles collected at 250 m varied from 1.9 to 24.0 ng m<sup>-2</sup>  
286 d<sup>-1</sup> over the deployment period (Fig. 2); the range of this one-year-long record range is predictably  
287 broader than the range of Hg fluxes recorded in the Central Pacific during 24-hour sediment trap  
288 deployments (3.6 to 8.4 ng m<sup>-2</sup> d<sup>-1</sup> according to Munson et al., 2015). In the settling particles  
289 collected at 250 m during the sediment trap deployment above the BAP, the biogenic fraction was  
290 dominant (averaging 57 %). The concomitant, temporal variations of Hg concentrations and  
291 biogenic contents of the material collected in this trap (Fig. 2) as well as the positive correlation  
292 ( $R^2 = 0.60$ ,  $p < 0.01$ ) between Hg concentrations and the monthly average Chlorophyll-a  
293 concentrations in surface waters (data from Zúñiga et al., 2007a) support the hypothesis that the  
294 vertical transfer of Hg through the water column is governed by phytoplanktonic uptake in the  
295 euphotic zone and the subsequent formation and settling of large biogenic particles in response to  
296 zooplankton grazing and excretion. However, irrespective of depth, there is no significant  
297 correlation between Hg and C<sub>org</sub> concentrations in the trapped material. Biogenic material present  
298 in the settling particles of the Western Mediterranean consists of OM, calcium carbonates, and opal  
299 (Zúñiga et al 2007a), each component having a distinct affinity for Hg. In addition, the downward  
300 Hg flux is modulated by the lithogenic contribution (8-67 % according to Zúñiga et al., 2007a) to  
301 settling particles in the Mediterranean, ballasting biogenic material, especially during Saharan dust  
302 storms (Ternon et al., 2010). It is not surprising, owing to the diversity of settling particle  
303 composition, that its association with Hg is not directly accounted for by the C<sub>org</sub> proxy. Binding

304 sites on OM are numerous and the stability of Hg complexes increases from carboxylic to thiolic  
305 groups (Haitzer et al., 2003; Ravichandran, 2003; Skyllberg et al., 2006; Liang et al., 2019). Using  
306 synchrotron-based X-ray Absorption Near-Edge Structure (XANES) and Extended X-ray  
307 Absorption Fine Structure (EXAFS) spectroscopy, it was discovered that, in laboratory bacterial  
308 cell suspensions, all divalent Hg ions were complexed to cell-bound thiolic functional groups  
309 (Mishra et al., 2017; Song et al., 2020). Complexation of methylmercury to phytoplanktonic cells  
310 may occur through the same mechanism (Skrobonja et al., 2019). In the absence of thiol and sulfur  
311 concentration data in the sediment trap material, the assumption that Hg is strongly associated to  
312 organic planktonic material and their debris is likely sound. This does not mean that the Hg  
313 concentration of settling particles is not, occasionally, affected by Saharan dust inputs. Very high  
314 Hg concentrations ( $\sim 2 \mu\text{g g}^{-1}$ ) have been measured in small particles of African dust collected in  
315 the Azores Islands as a result of emissions from open-pit Hg mines or the mined rock formations  
316 in Algeria (USGS, 2001). However, these findings are not confirmed by recent measurements  
317 performed on Saharan dust collected during a survey in the Canary Islands, where they are  $<100$   
318  $\text{ng g}^{-1}$  (Bailey, 2021). Additional results are needed to clarify this issue.

319 Mercury associated with particles collected in traps located at 1440 and 2820-m depth only  
320 accounts for ca. 70 % of the total flux at 250 m. This implies that ca. one-third of the Hg is  
321 remobilized from the settling material between 250 and 1440 m. This depth interval, the so-called  
322 “twilight zone”, which hosts heterotrophic activity, is the locus of net microbiological Hg  
323 methylation, with methylmercury (MeHg) accounting for up to 37 % of the THg (Cossa et al.,  
324 2009). Since MeHg has more affinity for the dissolved phase than inorganic Hg, Hg methylation  
325 is likely a critical mobilization process in the twilight zone. Below 1440 m, the Hg flux is invariant.  
326 Accordingly, the Hg:C<sub>org</sub> ratio nearly triples between 250 and 2820 m (Table 2). This increase

327 reflects the preferential removal of Hg from the surface ocean relative to C export, as observed in  
328 the Pacific Ocean water column (Munson et al., 2015), and implies that Hg released upon the  
329 remineralization of particulate OM during settling through the water column must re-adsorb onto  
330 the residual particulate matter. Culture experiments have shown that Zn released from degrading  
331 phytoplankton is rapidly scavenged back onto settling OM (John and Conway, 2014). Such a  
332 process is likely relevant for Hg since conditional stability constants for Hg complexed to dissolved  
333 and particulate OM are larger than those of Zn (e.g., Feyte et al., 2010). During the scavenging  
334 process, the nature of the particulate Hg-OM binding sites probably changes as C<sub>org</sub> is degraded  
335 during settling through the BAP water column, favoring the preferential binding of Hg to stronger  
336 ligands, such as thiol groups (Feyte et al., 2012; Liang et al., 2019; Guédron et al., 2020). Owing  
337 to the oxic conditions of the sediments, it can be expected that biogeochemical processes, similar  
338 to those occurring in the water column, control the Hg behavior in the sedimentary column.  
339 Nonetheless, the contrasting residence times in the two environments must be considered: the  
340 settling time of particles through a 2850 m water column is on the order of weeks, whereas the  
341 accumulation of a 30 cm thick sediment column is counted in thousands of years.

#### 342 ***4.2. Diagenetic remobilization of mercury in the sediment column***

343 Three main differences in the Hg and C<sub>org</sub> geochemical behaviors are observed between  
344 sediment and settling particles collected in the traps. First, except for units U1 and U2, a strong  
345 correlation is found between the two parameters in the three cores ( $R^2 = 0.80$ ,  $p < 0.01$ , Suppl. Info.  
346 Fig. S4). Second, the Hg:C<sub>org</sub> ratio in the sediments decreases with depth, in contrast to the particles  
347 that settles through the water column. Finally, whereas both Hg and C<sub>org</sub> exhibit their highest  
348 concentrations in the first cm below the SWI (Fig. 5a and b) and the C<sub>org</sub> concentrations decrease  
349 with increasing depth in the sediment (Fig. 5b) as a result of active microbial remineralization, the

350 decreasing Hg:C<sub>org</sub> ratio (Fig. 5c) reflects a faster decreasing rate of Hg deposition with depth. This  
351 interpretation rests on the hypothesis that diagenetic Hg remobilization is limited, and supports a  
352 rise in anthropogenic Hg deposition in surficial sediments.

353 It has been proposed that the vertical distribution of Hg in Arctic deep sediments may be  
354 modulated by diagenetic remobilization and shuttling with the Fe cycle (Gobeil et al., 1999). In  
355 order to explore this possibility, we analyzed the Hg associated with amorphous iron oxides or  
356 ascorbate-extractable Fe (Fe<sub>asc</sub>) in the BAP sediments. The Fe<sub>asc</sub> fraction accounts for  $0.7 \pm 0.4$  %  
357 of the total Fe, whereas the associated Hg (Hg<sub>asc</sub>) accounts for  $0.9 \pm 0.7$  % of the total Hg (Suppl.  
358 Info., Table S2). In addition, Hg<sub>asc</sub> and Fe<sub>asc</sub> are not correlated, except weakly in the first 5 cm of  
359 the sediments ( $R^2 = 0.51$ ,  $p < 0.10$ ). Thus, our results indicate that the Hg associated with the  
360 amorphous iron oxide fraction is very small, implying that the amount of Hg diagenetically  
361 recycled with Fe oxides in BAP sediments is very limited. This conclusion is consistent with results  
362 of *in situ* experiments at a lacustrine sediment-water interface and modeling that show Hg to be  
363 preferentially bound to functional groups of the OM rather than to the hydroxyl groups of Fe-  
364 oxy(hydro)oxide surfaces (Feyte et al., 2010). The occurrence of the turbidite layer (U3), which  
365 capped the underlying layers (U1 and U2), also brings complementary insights about the potential  
366 redistribution of Hg resulting from a transitory redox change in the sediment column. The  $\delta^{34}\text{S}$   
367 values below the turbidite fail to indicate the presence of significant sulfate reduction products  
368 (Fig. 4h). Nonetheless, the sharp drop in Fe<sub>HCl</sub> and Mn<sub>HCl</sub> concentrations (Fig. 4i and j) immediately  
369 below the turbidite (U3) could be evidence of transient suboxic or anoxic conditions that developed  
370 at the top of the pteropod ooze (U2), fueled by the rapid burial of fresh OM that had accumulated  
371 at the former SWI. Under these conditions, reactive Mn and Fe in these sediments would have been  
372 reductively dissolved and migrated from U1 to U3 where the Fe and Mn were oxidized and

373 reprecipitated as authigenic oxides by the oxygen advected with the porewaters of the turbidite  
374 (Fig. 4i and j). A similar process has been described in detail for cores collected in a coastal  
375 environment subjected to a mass-wasting event (Mucci et al., 2003). In the BAP, the reductive  
376 dissolution of iron oxides below the turbidite, which might have occurred after the U3 turbidite  
377 deposition, is not accompanied by a decrease in Hg concentration as Hg concentrations peak within  
378 U1 (Fig. 5a). In other words, despite the microbial decay of fresh OM and the transitory  
379 development of reducing conditions that lead to the reductive dissolution of Fe oxides, Hg  
380 remained mostly immobile or was rapidly re-adsorbed onto the solid sediment including OM, as in  
381 the water column, through binding to reduced sulfur compounds. Indeed, the strong affinity of Hg  
382 for reduced sulfur seems to modulate both (i) scavenging through the water column and (ii)  
383 sediment sequestration following diagenetic remobilization. This hypothesis is supported by the  
384 strong correlations between the distributions of Hg and sulfur in the sediment of Core B (Fig. 6).  
385 Most of the variability in Hg concentrations in the deepest part (>23 cm) of the core, and in the  
386 turbidite unit (U3) of the sediment, is explained by the sulfur content, as illustrated by their  
387 respective correlations ( $R^2 = 0.65$  and  $0.74$ ,  $p < 0.10$  and  $p < 0.05$ ). In these two layers, the Hg/S  
388 varies only slightly, whereas, in U1 (<23 cm), U2, U4, and U5, the regression coefficient of the  
389 Hg-S relationship is much higher (Fig. 6). It is interesting to note that in the turbidite (U3), in which  
390 a volcanic contribution has been ascertained (see section 3), there is no Hg anomaly that could hint  
391 at a geogenic origin (Fig. 6, insert). In other words, the distribution of Hg:S ratios through the core  
392 fails to reveal possible Hg inputs of volcanic or hydrothermal sources. The higher Hg:S ratio, in  
393 U1 (<23 cm), U2, U4, and U5 units (Fig. 6) could reflect the accumulation of fine cinnabar particles  
394 emitted to the Mediterranean atmosphere from the Almaden mines (Spain) since the beginning of  
395 their operation around 430 BC (Moreno et al., 2005).

396 At this stage, we can conclude that the participation of Hg in the diagenetic Fe-cycle in these  
397 abyssal sediments is limited and that a possible influence of local volcanism on Hg enrichment of  
398 the sediments is ruled out. Thus, the vertical distribution of Hg in the BAP likely provides an  
399 exploitable chronological record of Hg deposition during the Late Holocene Period, although  
400 smoothing by biological mixing must still be taken into consideration in the interpretation of this  
401 record.

### 402 ***4.3. Chronology of Hg fluxes and deposition***

#### 403 ***4.3.1. Modern deposition***

404 Computed Hg-ARs for the first 2 cm (based on radionuclide profiles), which represent the last  
405 120 years, averaged  $9.8 \pm 0.9$ ,  $8.3 \pm 1.0$ , and  $8.5 \pm 1.8 \mu\text{g m}^{-2} \text{yr}^{-1}$  in cores A, B, and C, respectively  
406 (Figs. 5d and 7). Although the  $^{210}\text{Pb}$  profile shows a classical decrease with depth (Suppl. Info.,  
407 Fig. S1), a previous study using artificial radionuclides ( $^{137}\text{Cs}$  and  $^{239,240}\text{Pu}$ ; Garcia-Orellana et al.,  
408 2009) divulges that the Hg signal has been smoothed by biological mixing. Even though they may  
409 carry large uncertainties, estimated surficial (0-1 cm) Hg-ARs ( $8.6 \pm 1.9 \mu\text{g m}^{-2} \text{yr}^{-1}$ ) for the last 50  
410 years in the three cores are consistent with those ( $8.4 \mu\text{g m}^{-2} \text{yr}^{-1}$ ) measured over the same period  
411 in the Ligurian Sea (Heimbürger et al., 2012). Although not directly comparable due to possible  
412 diagenetic processes in the nepheloid layer, these values are also consistent with those derived from  
413 the analysis of the sediment trap material recovered at 2820 m ( $3.1 \pm 0.5 \mu\text{g m}^{-2} \text{yr}^{-1}$ , Table 2),  
414 which integrates the Hg deposition between 2001 and 2002. These lower recent deposition rates  
415 concur with the reported  $\sim 30\%$  decrease of Hg concentrations in the western Mediterranean deep  
416 waters between 1989 and 2012 (Cossa et al., 2020) as well as with the reduced Hg emissions from  
417 utilities over the past two decades, that led to lower global anthropogenic emissions and associated  
418 deposition to ecosystems (Zhang et al., 2016). Overall, the observed sediment-surface Hg-

419 enrichment is consistent with the increasing global anthropogenic Hg emissions since the  
420 beginning of the Industrial Era (i.e., ~AD 1850 according to Outridge et al., 2018). The  
421 corresponding Hg-ARs are at least one order of magnitude larger than for the pre-Anthropocene  
422 epoch (i.e., before 1000 BC) background value ( $0.7 \pm 0.2 \mu\text{g m}^{-2} \text{yr}^{-1}$ ) in the three cores.

#### 423 4.3.2. Pre- and historical Hg deposition

424 The first rise in Hg-ARs recorded in the 3 cores recovered in the BAP appears during the Iron  
425 Age period (i.e., the upper part of U1, ~800 to 50 BC), as Hg-ARs increased from the baseline ( $0.7$   
426  $\pm 0.2 \mu\text{g m}^{-2} \text{yr}^{-1}$ ) to an average value of  $2.5 \pm 0.7 \mu\text{g m}^{-2} \text{yr}^{-1}$  (t-test,  $p < 0.01$ ). Because atmospheric  
427 circulation in the Mediterranean Basin is dominated by westerly winds (Ait Brahim et al., 2019;  
428 Azuara et al., 2020), the most probable source of Hg is the Iberian Peninsula where intense mining  
429 activities have been reported since the late Holocene period (Kassianidou and Knapp, 2005;  
430 Martínez-Cortizas et al., 1999), accounting for about half of the registered global Hg production in  
431 Europe (Hylander and Meili, 2003). Metal mining was also very active in Sardinia (Terpstra, 2021).  
432 This peak in Hg-AR is synchronous with the first  $^{206/207}\text{Pb}$  isotope anomaly (down to ~1.192)  
433 reported by Angelidis et al. (2011, Fig. 7, Suppl. Info., Fig. S1), and is consistent with known lead,  
434 silver, and cinnabar refining, smelting, and mining activities in Iberia during the Iron Age and  
435 Roman Empire (Nriagu, 1983). These activities are also recorded in other Mediterranean coastal  
436 sediments (Elbaz-Poulichet et al., 2011; Serrano et al., 2013), in a Spanish mire (Mártinez-Cortizas  
437 et al., 1997; 1999), and remote alpine lake sediments (Elbaz-Poulichet et al., 2020; Thevenon et  
438 al., 2011). In contrast to signals recorded in other archives, the dome-shaped Hg-AR record in the  
439 BAP sediments during the Iron Age and Roman Empire (Fig. 7) likely results from smoothing by  
440 biomixing of the geologically high-frequency variation of the anthropogenic signal. At the decline  
441 of the Roman Empire, ca. AD 200, Hg-ARs return to baseline values, just before the turbidite is

442 deposited (U3) (~AD 300). The latter was laid down at the same period as the Mediterranean  
443 megaturbidite was triggered by the AD 365 Crete earthquake and tsunami (Polonia et al., 2013).  
444 From that time on to ~AD 1800, Hg-ARs increase slightly and gradually from, on average,  $1.0 \pm$   
445  $0.2$  to  $1.5 \pm 0.5 \mu\text{g m}^{-2} \text{y}^{-1}$  in the 3 cores. Surprisingly, no marked peak was found corresponding  
446 to the Medieval Period (i.e., AD 500 to 1500), although this period is known for the massive  
447 development of metallurgy throughout Europe, including the intense metallurgical activities during  
448 the Islamic Period in Spain (AD 711 to 1492), a period documented by sharp increases in both Hg  
449 and Pb-ARs in almost all European records (Fig. 7, references herein). We consider that given the  
450 magnitude of the source, the low sedimentation rate, and the resolution of the BAP record,  
451 biomixing may have smoothed the signal and obliterated these short-duration mining peaks.

452

## 453 **5. SUMMARY AND CONCLUSIONS**

454 Temporal reconstruction of Hg deposition from sediment archives is relatively straightforward  
455 in organic-rich or high sedimentation rate environments since its diagenetic remobilization is  
456 limited compared to the large excursions in Hg emissions and deposition over the past 2000 years.  
457 Hg accumulation occurs mostly in areas, i.e., freshwater lakes or near-shore marine zones, close to  
458 point sources. To retrieve historical records on regional or global scales, deep-sea sediments are  
459 more appropriate. In addition, due to their slow accumulation rates, deep-sea sediments can provide  
460 deposition patterns over long periods, at least covering the Holocene. Such records are scarce, and  
461 their reliability has been questioned because of possible diagenetic remobilization, physical and  
462 biological mixing as well as post-depositional Hg redistribution resulting from mass-wasting  
463 processes (e.g., debris flows, submarine landslides/slumps, and turbidity currents). The sediment  
464 record of Hg deposition in the BAP of the Western Mediterranean - where sedimentation rates are

465 low ( $< 5 \text{ cm yr}^{-1}$ ) - is disrupted by episodic submarine slumps, transient redox gradients, and  
466 volcanic events. Nevertheless, our Hg sediment profiles, combined with analyses of sediment trap  
467 material recovered at different depths in the water column, allowed us to interpret its geochemical  
468 behavior through the water and sedimentary columns. Our results suggest that Hg deposited onto  
469 the ocean surface is (i) partially re-emitted from the surface waters to the atmosphere, (ii) taken up  
470 by plankton and sequestered mainly through complexation to thiolic functional groups of the  
471 biogenic material, (iii) partially mobilized and methylated in the twilight zone, and (iv) exported  
472 to the seafloor by the settling particulate organic matter. The vertical distributions of Hg,  $C_{\text{org}}$ , and  
473 S, as well as Fe speciation in the sediment, allow us to conclude that (i) a very limited amount of  
474 Hg is sorbed to amorphous Fe oxyhydroxides and, thus, the record of Hg deposition was not  
475 significantly affected by diagenetic remobilization, and (ii) hydrothermal or volcanic sources did  
476 not alter the Hg distribution. Hence, it is reasonable to propose that, in the Western Mediterranean,  
477 Hg is scavenged out of the water column and buried in the sediment as thiolate complexes, which  
478 may be converted to  $\beta$ -HgS according to the thermodynamically favorable reaction proposed by  
479 Manceau et al. (2015) for oxic soils. The formation of HgSe may further stabilize particulate Hg  
480 under suboxic conditions, as reported in other Mediterranean abyssal sediments (Mercone et al.,  
481 1999). We conclude that in the low  $C_{\text{org}}$  and low sedimentation rate BAP environment, Hg  
482 sedimentary profiles in  $\sim 30$  cm cores are exploitable as chronological records of Hg deposition  
483 during the Late Holocene Period. In brief, owing to negligible diagenetic Hg remobilization and  
484 despite significant smoothing of the temporal variations of the Hg-ARs, the abyssal sediments of  
485 the Western Mediterranean preserve the imprints of major natural and anthropogenic Hg  
486 deposition. The Hg-AR rose from background values of  $0.7 \pm 0.2 \mu\text{g m}^{-2} \text{y}^{-1}$  in sediments  
487 deposited more than 5000 years ago, to  $8.9 \pm 1.4 \mu\text{g m}^{-2} \text{y}^{-1}$  in sediments deposited over the last  
488 century. The geochronological records highlight the imprints of the Iron Age, the Roman Empire,

489 a gradual increase of Hg depositions during the Medieval Period as well as the large contribution  
490 of the Industrial Era.

491 As a semi-enclosed sea, the Mediterranean receives Hg onto its surface waters and transfers it  
492 at depth at a higher rate than in the Pacific Ocean (Munson et al., 2015 and section 4.1.) and,  
493 consequently, its deep-sea sediments are more likely to provide a record of anthropogenic inputs.  
494 In contrast, the deep surficial sediments of the Arctic Ocean, another semi-enclosed sea, fail to  
495 show clear evidence of anthropogenic Hg contamination (Gobeil et al., 1999), although both  
496 systems export Hg to the North Atlantic Ocean (Cossa et al., 2018a; 2018b). This discrepancy most  
497 likely results from the relative strength of local Hg sources, the enhanced efficiency of Hg  
498 ballasting by aggregation of the biogenic carrier phase with Saharan dust, as well as the absence of  
499 significant Hg diagenetic rearrangement on the deep-sea Holocene sediments of the Mediterranean.

500

501

## REFERENCES

502 ADIOS (2004) *Atmospheric deposition and Impact of Pollutants, key elements, and nutrients on*  
503 *the open Mediterranean Sea*. Final Report, Section 6: detailed report related to overall project  
504 duration. 93p. European Communities. Contract number: EVK3-CT-2000-00035 Coordinator:  
505 S. Heussner (CNRS, France).

506 Ait Brahim Y., Wassenburg J. A., Sha L., Cruz F. W., Deininger M., Sifeddine A., Bouchaou L.,  
507 Spötl C., Edwards R. L. and Cheng H. (2019) North Atlantic Ice-Rafting, Ocean and  
508 Atmospheric Circulation During the Holocene: Insights From Western Mediterranean  
509 Speleothems. *Geophys. Res. Lett.* **46**, 7614-7623.

510 Aksentov K. I. and Sattarova V. V. (2020) Mercury geochemistry of deep-sea sediment cores from  
511 the Kuril area, northwest Pacific. *Progr. Oceanogr.* **180**, 102235.

- 512 Angelidis M. O., Radakovitch O., Veron A., Aloupi M., Heussner S., Price B. (2011)  
513 Anthropogenic metal contamination and sapropel imprints in deep Mediterranean sediments.  
514 *Mar. Pollut. Bull.* **62**, 1041-1052.
- 515 Azoury, S., Tronczynski J., Chiffolleau J.-F., Cossa D., Nakhlé K., Schmidt S. and Khalaf G. (2013)  
516 Historical Records of Mercury, Lead, and Polycyclic Aromatic Hydrocarbons Depositions in a  
517 Dated Sediment Core from the Eastern Mediterranean. *Environ. Sci. Technol.* **47**, 7101–7109.
- 518 Azuara J., Sabatier P., Lebreton V., Jalali B., Sicre M. A., Dezileau L., Bassetti M.A., Frigola J.  
519 and Coumbourieu-Nebout N. (2020) Mid- to Late-Holocene Mediterranean climate variability:  
520 Contribution of multi-proxy and multi-sequence comparison using wavelet analysis in the  
521 northwestern Mediterranean basin. *Earth Sci. Rev.* **208**, 103232.
- 522 Bagnato E., Oliveri E., Covelli S., Petranich E., Barra M., Italiano F., Prelo F. and Sprovieri M.  
523 (2017) Hydrochemical mercury distribution and air-sea exchange over the submarine  
524 hydrothermal vents off-shore Panarea Island (Aeolian arc, Tyrrhenian Sea). *Mar. Chem.* **194**,  
525 63-78.
- 526 Bailey N. (2021) Saharan Dust as a Mercury Transport Vector. M.Sc. thesis, Department of  
527 Environment and Geography, University of Manitoba, Winnipeg, Canada.
- 528 Bertine K. K. and Goldberg E. D. (1977) History of Heavy Metal Pollution in Southern California  
529 Coastal Zone-Reprise. *Environ. Sci. Technol.* **11**, 297-299.
- 530 Callender E. (2003) *Heavy Metals in the Environment—Historical Trends*. Treatise on  
531 Geochemistry, Vol. 9.03, 67-105. Turekian K. K., Holland H. D. editors. Elsevier Sciences.
- 532 Cattaneo A., Badhani S., Caradonna C., Bellucci M., Leroux E., Babonneau N., Garziglia S., Poort  
533 J., Akhmanov G. G., Bayon G., Dennielou B., Jouet G., Migeon S., Rabineau M., Droz L. and  
534 Clare M. (2020) The Last Glacial Maximum Balearic Abyssal Plain Megabed revisited. *Geol.*  
535 *Soc. Lond. Sp. Publ.* **500**, 341-357.
- 536 Cooke C. A., Wolfe A. P. and Hobbs W. O. (2009) Lake-sediment geochemistry reveals 1400 years  
537 of evolving extractive metallurgy at Cerro de Pasco, Peruvian Andes. *Geology* **37**, 1019–1022.
- 538 Cooke C. A., Martínez-Cortizas A., Bindler R. and Gustin M. S. (2020) Environmental archives of  
539 atmospheric Hg deposition – A review. *Sci. Total Environ.* **709**, 134800.

- 540 Corella J. P., Valero-Garcés B. L., Wang F., Martínez-Cortizas A., Cuevas C. A. and Saiz-Lopez  
541 A. (2017) 700 years reconstruction of mercury and lead atmospheric deposition in the Pyrenees  
542 (NE Spain). *Atmos. Environ.* **155**, 970–1107.
- 543 Cossa D., Elbaz-Poulichet F. and Nieto J. M. (2001) Mercury in the Tinto-Odiel Estuarine System  
544 (Gulf of Cadiz, Spain): Sources and Dispersion. *Aquat. Geochem.* **7**, 1-12.
- 545 Cossa, D., Averty B. and Pirrone N. (2009) The origin of methylmercury in the open Mediterranean  
546 water column. *Limnol. Oceanogr.* **54**, 837–844.
- 547 Cossa D., Heimbürger L.-E., Sonke J. E., Planquette H., Lherminier P., García-Ibáñez M. I., Pérez  
548 F. F. and Sarthou G. (2018a) Sources, recycling and transfer of mercury in the Labrador Sea  
549 (Geotraces-Geovide cruise). *Mar. Chem.* **198**, 64-69.
- 550 Cossa, D., Heimbürger L.-E., Pérez F. F., García-Ibáñez M. I., Sonke J. E., Planquette H.,  
551 Lherminier P., Boutorh J., Cheize M., Menzel Barraqueta J. L., Shelley R. and Sarthou G.  
552 (2018b) Mercury distribution and transport in the North Atlantic Ocean along the Geotraces-  
553 GA01 transect. *Biogeosciences* **15**, 2309-2323.
- 554 Cossa D., Knoery J., Boye M., Maruszczak N., Thomas B., Courau P. and Sprovieri S. (2020)  
555 Oceanic mercury concentrations on both sides of the Strait of Gibraltar decreased between 1989  
556 and 2012. *Anthropocene* **29**, 100230.
- 557 Crusius J. and Thomson J. (2003) Mobility of authigenic rhenium, silver, and selenium during  
558 postdepositional oxidation in marine sediments *Geochim. Cosmochim. Acta* **67**, 265-273.
- 559 Edgington D. N. and Robbins J. A. (1976) Records of Lead Deposition in Lake Michigan  
560 Sediments Since 1800. *Environ. Sci. Technol.* **10**, 266-274.
- 561 Elbaz-Poulichet, F., Dezileau L., Freydier R., Cossa D. and Sabatier P. (2011) A 3500-year record  
562 of Hg and Pb contamination in a Mediterranean sedimentary archive (the Pierre Blanche  
563 Lagoon, France). *Environ. Sci. Technol.* **45**, 8642-8647.
- 564 Elbaz-Poulichet F., Guédron S., Anne-Lise D., Freydier R., Perrot V., Rossi M., Piot C., Delpoux  
565 S. and Sabatier P. (2020) A 10,000-year record of trace metal and metalloid (Cu, Hg, Sb, Pb)  
566 deposition in a western Alpine lake (Lake Robert, France): Deciphering local and regional  
567 mining contamination. *Quat. Sci. Rev.* **228**, 106076.

568 EPA (2007) Method 7473: *Mercury in Solids and Solutions by Thermal Decomposition,*  
569 *Amalgamation, and Atomic Absorption Spectrophotometry* (17 pp).  
570 <https://www.epa.gov/sites/production/files/2015-12/documents/7473.pdf>

571 EURACHEM/CITAC (2000) Quantifying uncertainty in analytical measurement. Tech. Rep. Guide  
572 CG4, EU-RACHEM/CITEC, EURACHEM/CITAC Guide. Second edition.

573 Feyte S., Tessier A., Gobeil C. and Cossa D. (2010) *In situ* adsorption of mercury, methylmercury  
574 and other elements by iron oxyhydroxides and associated organic matter in lake sediments. *Appl.*  
575 *Geochem.* **25**, 984-995.

576 Feyte S., Gobeil C., Tessier A. and Cossa D. (2012) Mercury dynamics in lake sediments *Geochim.*  
577 *Cosmochim. Acta* **82**, 92-112.

578 Fitzgerald W. F. and Lamborg C. H. (2005) *Geochemistry of mercury in the environment*. In:  
579 Lollar, B.S. Editor, Environmental Geochemistry. Elsevier–Pergamon, Oxford, pp. 107–148.

580 Fitzgerald W. F., Engstrom D. R., Hammerschmidt C. R., Lamborg C. H., Balcom P. H., Lima-  
581 Braun A. L., Bothner M. H. and Reddy C. M. (2018) Global and Local Sources of Mercury  
582 Deposition in Coastal New England Reconstructed from a Multiproxy, High-Resolution,  
583 Estuarine Sediment Record. *Environ. Sci. Technol.* **52**, 7614–7620.

584 Garcia-Orellana J., Pates J. M., Masqué P., Bruach J. and Sanchez-Cabeza J. (2009) Distribution  
585 of artificial radionuclides in deep sediments of the Mediterranean Sea. *Sci. Total Environ.* **407**,  
586 887-898.

587 Gencarelli C. N., De Simone F., Hedgecock I. M., Sprovieri F. and Pirrone N. (2014) Development  
588 and application of a regional-scale atmospheric mercury model based on WRF/Chem: a  
589 Mediterranean area investigation. *Environ. Sci. Pollut. Res. Int.* **21**, 4095-109.

590 Genovesi L., de Vernal A., Thibodeau B., Hillaire-Marcel C., Mucci A. and Gilbert D. (2011)  
591 Recent changes in bottom water oxygenation and temperature in the Gulf of St. Lawrence:  
592 micropaleontological and geochemical evidence. *Limnol. Oceanogr.* **56**, 1319-1329.

593 Gobeil C., Macdonald R. W. and Smith J. N. (1999) Mercury profiles in sediments of the Arctic  
594 Ocean basins. *Environ. Sci. Technol.* **33**, 4194-4198.

595 Grasby S. E., Sanei, H. and Beauchamp B. (2013) Mercury deposition through the Permo-triassic  
596 Crisis. *Chem. Geol.* **351**, 209-216.

597 Guédron S., Amouroux D., Sabatier P., Desplanque C., Develle A.-L., Barre J., Feng, C., Guiter  
598 F., Arnaud F., Reyss J.-L. and Charlet L. (2016) A hundred year record of industrial and urban  
599 development in French Alps combining Hg accumulation rates and isotope composition in  
600 sediment archives from Lake Luitel. *Chem. Geol.* **431**, 10–19.

601 Guédron S., Ledru M.-P., Escobar-Torrezd K., Devellee A. L. and Brisseta E. (2018) Enhanced  
602 mercury deposition by Amazonian orographic precipitation: Evidence from high-elevation  
603 Holocene records of the Lake Titicaca region (Bolivia). *Palaeogeogr. Palaeoclimatol.*  
604 *Palaeoeco.* **511**, 577-587.

605 Guédron S., Tolu J., Brisset E., Sabatier P., Perrot V., Bouchet S., Develle A. L., Bindler R., Cossa  
606 D. and Fritz S. C. (2019) Late Holocene volcanic and anthropogenic mercury deposition in the  
607 western Central Andes (Lake Chungará, Chile). *Sci. Tot. Environ.* **662**, 903-914.

608 Guédron S., Audry S., Acha D., Bouchet S., Point D., Condom T., Heredia C., Campillo S., Baya  
609 P. A., Groleau A., Amice E. and Amouroux D. (2020) Diagenetic production, accumulation and  
610 sediment-water exchanges of methylmercury in contrasted sediment facies of Lake Titicaca  
611 (Bolivia). *Sci. Total Environ.* **723**, 138088.

612 Haitzer M., Aiken G. R. and Ryan J. N. (2003) Binding of Mercury(II) to Aquatic Humic  
613 Substances: Influence of pH and Source of Humic Substances. *Environ. Sci. Technol.* **37**, 2436-  
614 2441.

615 Hamilton E. L. (1976) Variations of density and porosity with depth in deep-sea sediments. *J.*  
616 *Sediment. Res.* **46**, 280-300.

617 Hare, A. A., Stern G. A., Kuzyk Z. Z. A., Macdonald R. W., Johannessen S.L. and Wang F. (2010)  
618 Natural and Anthropogenic Mercury distribution in Marine Sediments from Hudson Bay,  
619 Canada. *Environ. Sci. Technol.* **44**, 5805-5811.

620 Heimbürger L. E., Cossa D., Thibodeau B., Khripounoff A., Mas V., Chiffoleau J.-F., Schmidt S.  
621 and Migon C. (2012) Natural and anthropogenic trace metals in sediments of the Ligurian Sea  
622 (Northwestern Mediterranean). *Chem. Geol.* **291**, 141-151.

623 Heussner S., Ratti C. and Carbonne J. (1990) The PPS3 sediment trap and trap sample processing  
624 techniques used during the ECOMARGE experiment. *Cont. Shelf Res.* **10**, 943-958.

- 625 Hylander L. D. and Meili M. (2003) 500 years of mercury production: global annual inventory by  
626 region until 2000 and associated emissions. *Sci. Tot. Environ.* **304**, 13-27.
- 627 John S. G. and Conway T. M. (2014) A role for scavenging in the marine biogeochemical cycling  
628 of zinc and cadmium isotopes. *Earth Planet. Sci. Lett.* **394**, 159-167.
- 629 Kassianidou V. and Knapp A. B. (2005) *Archeometallurgy in the Mediterranean: The Social*  
630 *Context of Mining, Technology, and Trade*. Chap. 9. pp. 215-251. In: *The archaeology of*  
631 *Mediterranean prehistory*. Blake E. and A.B. Knapp editors. Blackwell Studies in global  
632 archaeology, Blackwell Publish. 333 p. Oxford, UK. ISBN 0-631-23267-2.
- 633 Kita I., Kojima M., Hasegawa H. et al. (2013) Mercury content as a new indicator of ocean  
634 stratification and primary productivity in Quaternary sediments off Bahama Bank in the  
635 Caribbean Sea. *Quater. Res.* **80**, 606–613.
- 636 Kita I., Yamashita T., Hasegawa H., Sato T. and Kuwahara Y. (2016) Mercury content in Atlantic  
637 sediments as a new indicator of the enlargement and reduction of Northern Hemisphere ice  
638 sheets. *J. Quaternary Sci.* **31**, 167-177.
- 639 Kostka J. E. and Luther G. W. (1994) Partitioning and speciation of solid phase iron in saltmarsh  
640 sediments *Geochim. Cosmochim. Acta* **58**, 1701- 1710.
- 641 Kota F. S. (2004) Mercury in chemical fractions of recent pelagic sediments of the Sea of Japan.  
642 *J. Environ. Monit.* **6**, 689-695.
- 643 Lamborg C. H., Fitzgerald W. F., Damman A. W. H., Benoit J. M., Balcom P. H. and Engstrom D.  
644 R. (2002) Modern and historic atmospheric mercury fluxes in both hemispheres: Global and  
645 regional mercury cycling implications. *Global Biogeochem. Cycles* **16**, 1104.
- 646 Liang X., Lu X., Zhao J., Liang L., Zeng E. Y. and Gu B. (2019) Stepwise Reduction Approach  
647 Reveals Mercury Competitive Binding and Exchange Reactions within Natural Organic Matter  
648 and Mixed Organic Ligands. *Environ. Sci. Technol.* **53**, 10685–10694.
- 649 Lim D., Kim J., Xu Z. K., Jeong K. and Jung, H. (2017) New evidence for Kuroshio inflow and  
650 deepwater circulation in the Okinawa Trough, East China Sea: Sedimentary mercury variations  
651 over the last 20kyr. *Paleoceanography* **32**, 571-579.

- 652 Liotta M., Rizzo A., Paonita A., Caracausi A. and Martelli M. (2012) Sulfur isotopic compositions  
653 of fumarolic and plume gases at Mount Etna (Italy) and inferences on their magmatic source,  
654 *Geochem. Geophys. Geosyst.*, **13**, Q05015.
- 655 Mackie E. A. V., Lloyd J. M. and Leng M. J. (2007) Assessment of  $\delta^{13}\text{C}$  and C/N ratios in bulk  
656 organic matter as palaeosalinity indicators in Holocene and Late glacial isolation basin  
657 sediments, northwest Scotland. *J. Quat. Sci.* **22**, 579–591.
- 658 Manceau A., Lemouchi C., Enescu M., Gaillot A. C., Lanson M., Magnin V., Glatzel P., Poulin B.  
659 A., Ryan J. N., Aiken G. R., Gautier-Luneau I. and Nagy K. L. (2015) Formation of Mercury  
660 Sulfide from Hg(II)–Thiolate Complexes in Natural Organic Matter. *Environ. Sci. Technol.* **49**,  
661 9787-9796.
- 662 Martinez-Cortizas A., Pontevedra-Pombal X., Munoz J. N. and García-Rodeja E. (1997) Four  
663 thousand years of atmospheric Pb, Cd and Zn deposition recorded by the ombrotrophic peat bog  
664 of Penido Vello (Northwestern Spain). *Water Air Soil Pollut.* **100**, 387-403.
- 665 Martinez-Cortizas A., Pontevedra-Pombal X., Garcia-Rodeja E., Novoa-Munoz J. C. and Shotyk  
666 W. (1999) Mercury in a Spanish peat bog: archive of climate change and atmospheric metal  
667 deposition. *Science* **284**, 939-942.
- 668 Mason R. P., Choi A. L., Fitzgerald W. F., Hammerschmidt C. R., Lamborg C. H., Soerensen A.  
669 L. and Sunderland E. M. (2012) Mercury biogeochemical cycling in the ocean and policy  
670 implications. *Environ. Res.* **119**, 101-117.
- 671 Mercone D., Thomson J., Croudace I. W. and Troelstra S. R. (1999) A coupled natural  
672 immobilisation mechanism for mercury and selenium in deep-sea sediments  
673 *Geochim. Cosmochim. Acta* **63**, 1481-1488.
- 674 Meyers P. A. (1994) Preservation of elemental and isotopic source identification of sedimentary  
675 organic matter. *Chem. Geol.* **114**, 289–302.
- 676 Mikac N., Niessen S., Ouddane B. and Fisher J.-C. (2000) Effects of Acid Volatile Sulfides on the  
677 Use of Hydrochloric Acid for Determining Solid-Phase Associations of Mercury in Sediments.  
678 *Environ. Sci. Technol.* **34**, 1871-1876.
- 679 Mishra B., Shoenfelt E., Yu Q., Yee N., Fein J. B., Myneni S. C. B. (2017) Stoichiometry of  
680 mercury-thiol complexes on bacterial cell Envelopes. *Chem. Geol.* **464**, 137-146.

- 681 Moreno T., Higuera P., Jones T., McDonald I. and Gibbons W. (2005) Size fractionation in  
682 mercury-bearing airborne particles (HgPM10) at Almadén, Spain: Implications for inhalation  
683 hazards around old mines. *Atmos. Environ.* **39**, 6409-6419.
- 684 Mucci A., Boudreau B. and Guignard C. (2003) Diagenetic mobility of trace elements in sediments  
685 covered by a flash flood deposit: Mn, Fe and As. *Appl. Geochem.* **18**, 1011-1026.
- 686 Mucci A., Bernier G. and Guignard C. (2015) Mercury remobilization in Saguenay Fjord (Quebec,  
687 Canada) sediments: Insights following a mass-flow event and capping efficiency. *Appl.*  
688 *Geochem.* **54**, 13-26.
- 689 Muir D. C. G., Wang X., Yang F., Nguyen N., Jackson T. A., Evans M. S., Douglas M., Köck, G.,  
690 Lamoureux S., Pienitz R., Smol J. P., Vincent W. F. and Dastoor A. (2009) Spatial Trends and  
691 Historical Deposition of Mercury in Eastern and Northern Canada Inferred from Lake Sediment  
692 Cores. *Environ. Sci. Technol.* **43**, 4802-4809.
- 693 Munson K. M., Lamborg C. H., Swarr G. J. and Saito M. A. (2015) Mercury species  
694 concentrations and fluxes in the Central Tropical Pacific Ocean. *Global Biogeochem. Cycle* **29**,  
695 656-676.
- 696 Nriagu J. O. (1983) Occupational exposure to lead in ancient times. *Sci. Total Environ.* **31**, 105-  
697 116.
- 698 Polonia A., Bonatti E., Camerlenghi A., Lucchi R. G., Panieri G. and Gasperini L. (2013)  
699 Mediterranean megaturbidite triggered by the AD 365 Crete earthquake and tsunami. *Sci. Rep.-*  
700 *UK* **3**, 1285.
- 701 Outridge P. M., Sanei H., Stern G. A., Hamilton P. B. and Goodarzi F. (2007) Evidence for control  
702 of mercury accumulation in sediments by variations of aquatic primary productivity in Canadian  
703 High Arctic lakes. *Environ. Sci. Technol.* **41**, 5259–5265.
- 704 Outridge P. M., Mason R. P., Wang F., Guerrero S. and Heimbürger-Boavida L. E. (2018) Updated  
705 Global and Oceanic Mercury Budgets for the United Nations Global Mercury Assessment 2018.  
706 *Environ. Sci. Technol.* **52**, 12968–12977.
- 707 Ravichandran M. (2003) Interactions between mercury and dissolved organic matter, A Review.  
708 *Chemosphere* **55**, 319-331.

- 709 Rees C. E., Jenkins W. J., Monster J. (1978) The sulphur isotopic composition of ocean water  
710 sulphate. *Geochim. Cosmochim. Acta* **42**, 377–381.
- 711 Reimer P. J., Austin W. E. N., Bard E., Bayliss A., Blackwell P. G., Bronk Ramsey C., Butzin M.,  
712 Cheng H., Edwards R. L., Friedrich M., Grootes P. M., Guilderson T. P., Hajdas I., Heaton T.  
713 J., Hogg A. G., Hughen K. A., Kromer B., Manning S. W., Muscheler R., Palmer J. G., Pearson  
714 C., van der Plicht J., Reimer R. W., Richards D. A., Scott E. M., Southon J. R., Turney C. S.  
715 M., Wacker L., Adolphi F., Büntgen U., Capano M., Fahrni S. M., Fogtman-Schulz A.,  
716 Friedrich R., Köhler P., Kudsk S., Miyake F., Olsen J., Reinig F., Sakamoto M., Sookdeo A.  
717 and Talamo S. (2020) The IntCal20 Northern Hemisphere Radiocarbon Age Calibration Curve  
718 (0–55 cal kBP). *Radiocarbon* **62**, 725-757.
- 719 Rothwell R. G., Hoogakker B., Thomson J., Croudace I. W. and Frenz M. (2006) *Turbidite*  
720 *emplacement on the southern Balearic Abyssal Plain (western Mediterranean Sea) during*  
721 *Marine Isotope Stages 1-3: an application of ITRAX XRF scanning of sediment cores to*  
722 *lithostratigraphic analysis*. Geological Society, London, Special Publications **267**, 79-98.
- 723 Sanei H., Grasby S. E. and Beauchamp B. (2012) Latest Permian mercury anomalies. *Geology* **40**,  
724 63–66.
- 725 Serrano O., Martínez-Cortizas A., Mateo M. A., Biester, H. and Bindler R. (2013) Millennial scale  
726 impact on the marine biogeochemical cycle of mercury from early mining on the Iberian  
727 Peninsula. *Global Biogeochem. Cycles* **27**, 21-30.
- 728 Siani G., Paterne M., Arnold M., Bard E., Métivier B., Tisnerat N. and Bassinot F. (2000)  
729 Radiocarbon Reservoir Ages in the Mediterranean Sea and Black Sea. *Radiocarbon* **42**, 271-  
730 280.
- 731 de Simone F., Gencarelli C. N., Hedgecock I. M. and Pirrone N. (2016) A Modeling Comparison  
732 of Mercury Deposition from Current Anthropogenic Mercury Emission Inventories. *Environ.*  
733 *Sci. Technol.* **50**, 5154-5162.
- 734 Skrobonja A., Gojkovic Z., Soerensen A. L., Westlund P. O., Funk C. and Bjorn E. (2019) Uptake  
735 Kinetics of Methylmercury in a Freshwater Alga Exposed to Methylmercury Complexes with  
736 Environmentally Relevant Thiols. *Environ. Sci. Technol.* **53**, 13757-13766.

- 737 Skjellberg U., Bloom P. R., Qian J., Lin C.-M. and Bleam W. F. (2006) Complexation of  
738 Mercury(II) in Soil Organic Matter: EXAFS Evidence for Linear Two-Coordination with  
739 Reduced Sulfur Groups. *Environ. Sci. Technol.* **40**, 4174-4180.
- 740 Smith J. N. and Loring D. H. (1981) Geochronology for mercury pollution in the sediments of the  
741 Saguenay Fjord, Quebec. *Environ. Sci. Technol.* **15**, 944-951.
- 742 Song Y., Adediran G. A., Jiang T., Hayama S., Björn E. and Skjellberg U. (2020) Toward an  
743 Internally Consistent Model for Hg(II) Chemical Speciation Calculations in Bacterium–Natural  
744 Organic Matter–Low Molecular Mass Thiol Systems. *Environ. Sci. Technol.* **54**, 8094–8103.
- 745 Ternon E., Guieu C., Loye-Pilot M.-D., Leblond N., Bosc E., Gasser B., Miquel J.-C. and Martin  
746 J. (2010) The impact of Saharan dust on the particulate export in the water column of the North  
747 Western Mediterranean Sea. *Biogeosciences* **7**, 809–826.
- 748 Terpstra T. T. (2021) Mediterranean silver production and the site of Antas, Sardinia. *Oxf. J.*  
749 *Archaeol.* **40**, 176-190.
- 750 Thevenon F., Guédron S., Chiaradia M., Loizeau J.-L. and Poté J. (2011) (Pre-) historic changes  
751 in natural and anthropogenic heavy metals deposition inferred from two contrasting Swiss  
752 Alpine lakes. *Quaternary Sci. Rev.* **30**, 224-233.
- 753 Thibodeau A. M., Ritterbush K., Yager J. A., West A. J., Ibarra Y., Bottjer D. J., Berelson W. M.,  
754 Bergquist B. A. and Corsetti F. A. (2016) Mercury anomalies and the timing of biotic recovery  
755 following the end-Triassic mass extinction: *Nature Com.* **7**, 1–8.
- 756 Thibodeau A. M. and Bergquist B. A. (2017) Do mercury isotopes record the signature of massive  
757 volcanism in marine sedimentary records? *Geology* **45**, 95–96.
- 758 Thomson J., Jarvis I., Green D. R. H., Green, D. A. and Clayton T. (1998) Mobility and immobility  
759 of redox-sensitive elements in deep-sea turbidites during shallow burial. *Geochim. Cosmochim.*  
760 *Acta* **62**, 643–656.
- 761 Tribouillard N., Algeo T. J., Lyons T. and Riboulleau A. (2006) Trace metals as paleoredox and  
762 paleoproductivity proxies: an update. *Chem. Geol.* **232**, 12–32.
- 763 UN-Environment 2019. *Global Mercury Assessment 2018*. United Nation Environmental  
764 Programme, Chemicals and Health Branch, Programme Chemicals and Health Branch Geneva

765 Switzerland. ISBN 978-92-807-3744-8. [https://www.unenvironment.org/resources/publication/](https://www.unenvironment.org/resources/publication/global-mercury-assessment-2018)  
766 [global-mercury-assessment-2018](https://www.unenvironment.org/resources/publication/global-mercury-assessment-2018).

767 USGS (2001) African Dust Causes Widespread Environmental Distress. *Open-File Report 01-246*,  
768 U.S. Geological Survey, July 2001.

769 Žagar D., Sirnik N., Četina M., Horvat M., Kotnik J., Ogrinc N., Hedgecock I. M., Cinnirella S.,  
770 de Simone F., Gencarelli C. N. and Pirrone N. (2014) Mercury in the Mediterranean. Part 2:  
771 processes and mass balance. *Environ. Sci. Pollut. Res.* **21**, 4081–4094.

772 Zhang Y., Jacob D. J., Horowitz H. M., Chen L., Amos H. M., Krabbenhoft D. P., Slemr F., St.  
773 Louis V. L. and Sunderland E.M. (2016) Observed decrease in atmospheric mercury explained  
774 by global decline in anthropogenic emissions. *Proc. Natl. Acad. Sci. U.S.A.* **113**, 526-531.

775 Zúñiga D., Calafat A. Sanchez-Vidal A., Canals M., Price N. B., Heussner S. and Miserocchi S.  
776 (2007a) Particulate organic carbon budget in the open Algero-Balearic Basin (Western  
777 Mediterranean): Assessment from a one-year sediment trap experiment. *Deep-Sea Res. I* **54**,  
778 1530-1548.

779 Zúñiga D., Garcia-Orellana J., Calafat A., Price N. B., Adatte T., Sanchez-Vidal A., Canals M.,  
780 Sanchez-Cabeza J. A., Masque P. and Fabres J. (2007b) Late Holocene fine-grained sediments  
781 of the Balearic Abyssal Plain, Western Mediterranean Sea. *Mar. Geol.* **237**, 25–36.

782

### 783 **Declaration of Competing Interest**

784 The authors declare that they have no known competing financial interests or personal  
785 relationships that could have appeared to influence the work reported in this paper.

786

### 787 **ACKNOWLEDGEMENTS**

788 This work was supported financially by the European Community in the framework of the ADIOS  
789 MAST program (EVK3-CT-2000-00035, Atmospheric deposition and impact of pollutants on  
790 the open Mediterranean Sea). We would like to thank Jean-Francois Hélie and Bassam Ghaleb  
791 at GEOTOP-UQAM for carrying out the total sulfur,  $\delta^{34}\text{S}$  and complementary  $^{210}\text{Pb}$  analyses.  
792 These analyses were subsidized by a Regroupement Stratégique grant from the Fonds Québécois  
793 de Recherche Nature et Technologies (FQRNT) to GEOTOP as well as an NSERC Discovery

794 grant to A.M. We would also like to thank Pascale Occhipinti and Laurent Nectoux for the Hg  
795 analyses performed at the INERIS, and Roselyne Buscail for providing the C and N data. Thanks  
796 are due to Neal Bailey and Feiyue Wang (University of Manitoba, Center for Earth Observation  
797 Science, Winnipeg, Canada) for providing Hg concentration levels in the Saharan dust collected  
798 in the Canary Islands and Cape Verde.  
799

800

## TABLES

801 *Table 1. Location, water depths of the multicore stations, and sediment core lengths in the Balearic Abyssal*802 *Plain of the Western Mediterranean.*

Station (core)	Latitude N	Longitude E	Depth (m)	Core length (cm)
A	39°28.30'	5°57.37'	2850	22
B	39°29.51'	6°10.88'	2854	32
C	39°18.81'	6°04.22'	2854	30

803

804

805 *Table 2. Mercury concentrations (mean ± standard deviation) in material recovered from sediment traps*806 *deployed at site C (Fig. 1, Table 1) between April 2001 and April 2002. Particulate organic carbon (POC)*807 *data are from Zúñiga et al. (2007a). Water column depth above sediments: 2854 m. Average atmospheric*808 *Hg deposition onto Mediterranean Sea surface waters is ca. 34 ng m<sup>-2</sup> d<sup>-1</sup> (Gencarelli et al., 2014).*

Depth (m)	Hg (ng g <sup>-1</sup> )	C <sub>org</sub> (%)	Hg/C <sub>org</sub> (molar ratio 10 <sup>-6</sup> )	POC flux (mg m <sup>-2</sup> d <sup>-1</sup> )	Hg flux (ng m <sup>-2</sup> d <sup>-1</sup> )
250	127 ± 30	13.4 ± 5.2	0.057	9.9	12.2 ± 8.2
1440	126 ± 19	6.7 ± 2.3	0.112	3.8	8.8 ± 5.5
2820	130 ± 20	5.1 ± 1.3	0.152	2.9	8.6 ± 6.2

809

810

## FIGURE CAPTIONS

811  
812 **Figure 1.** *Sampling location of sediment cores A, B, and C in the Balearic Abyssal Plain of the*  
813 *Western Mediterranean (see also Table 1).*

814 **Figure 2.** *Temporal variation of Hg concentrations in the material recovered from the sediment*  
815 *traps moored at station C between April 2001 and April 2002. Average biogenic content*  
816 *(organic matter, calcium carbonate, and opal) modified from figure 6 in Zúñiga et al. (2007a).*

817 **Figure 3.** *Information logs of sediment cores A, B, and C, showing geological units according to*  
818 *Zúñiga et al. (2007b): Pteropod ooze layers (U2 and U5), foraminifer–pteropod oozes (U1 and*  
819 *U4), and turbidite unit (U3) between 7-13 cm, 9-15 cm, and 8-14 cm, for cores A, B, and C,*  
820 *respectively. See text for details. Note that several multicorer samplings were performed at each*  
821 *site during the R/V Urania cruise in 2001. Hence, core B analyzed in this study is the same as*  
822 *the one described by Angelidis et al. (2011), but different from core B described by Zúñiga et*  
823 *al. (2007b).*

824 **Figure 4.** *Elemental composition of sediment core B.*

825 **Figure 5.** *Total mercury (Hg), Hg accumulation rate (Hg-AR), and Hg:C<sub>org</sub> ratio profiles in*  
826 *sediment cores A, B, and C.*

827 **Figure 6.** *Mercury (Hg) versus sulfur (S) concentrations in core B. The Hg:S ratio profile in*  
828 *sediment core B is given in the insert.*

829 **Figure 7.** *Hg accumulation rates (Hg-AR) for marine, lacustrine, and mire sediment historical*  
830 *records. Records are presented according to their geographical location from west to east*  
831 *following the trade wind direction (westerlies) from bottom to top: Penido Vello mire (Spain,*  
832 *Martínez-Cortizas et al., 1999), Portlligat Bay marine sediment (Spain, Serrano et al., 2013),*  
833 *cores A, B, and C marine sediment from the Balearic Abyssal plain (this study), and two*  
834 *headwater catchment lake records from the western (Robert, France, Elbaz-Poulichet et al.,*  
835 *2020) and central Alps (Meidsee, Switzerland, Thevenon et al., 2011).*

836

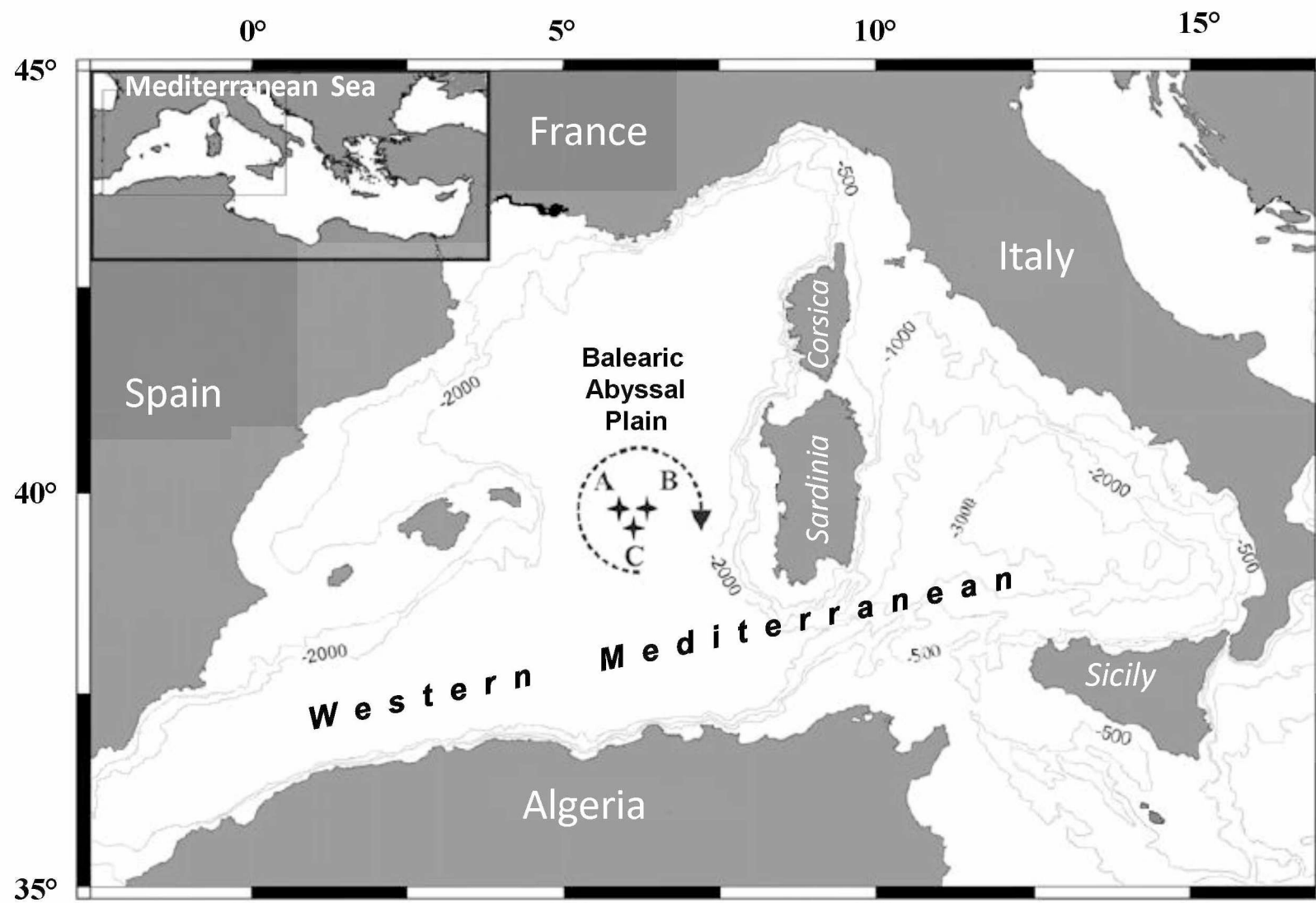


Fig. 1

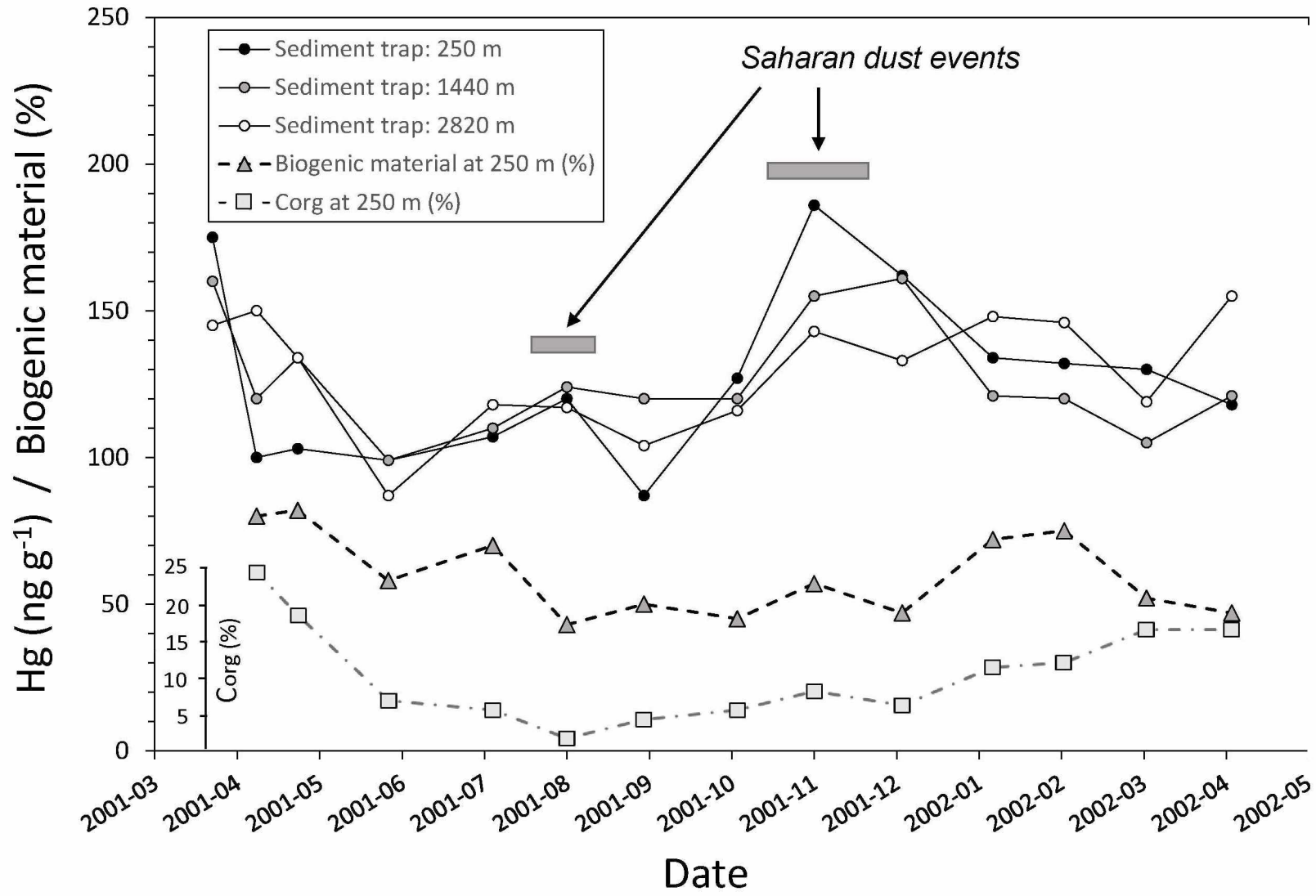


Fig. 2

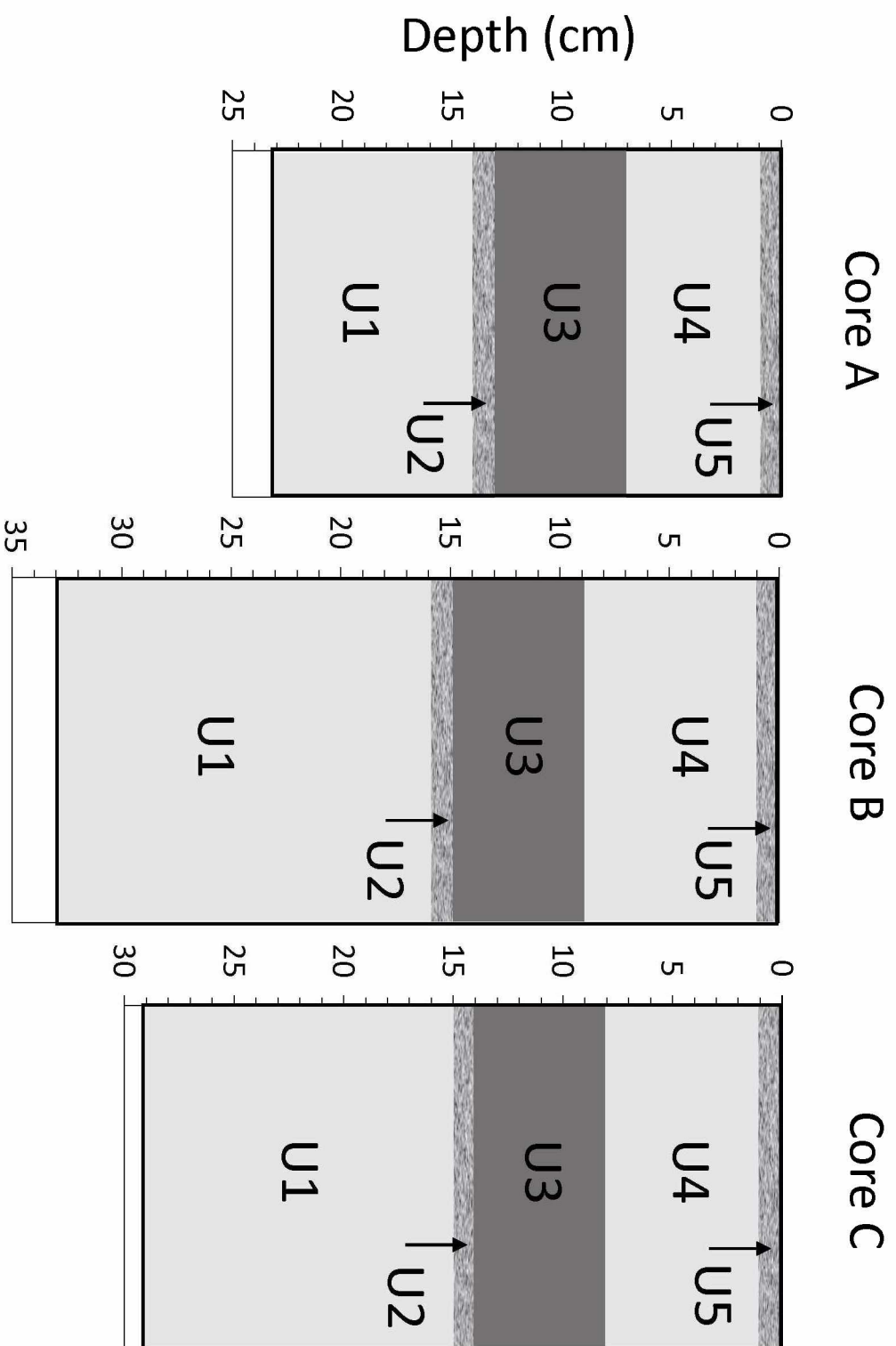


Fig. 3

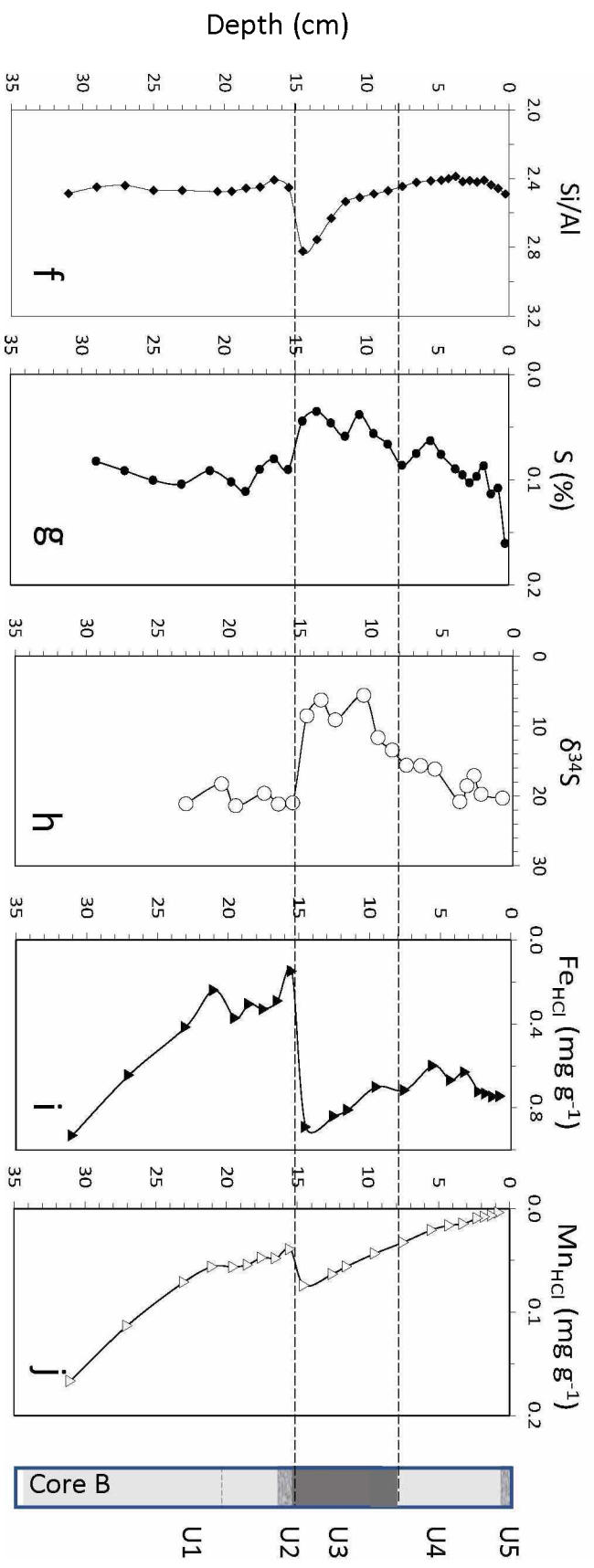
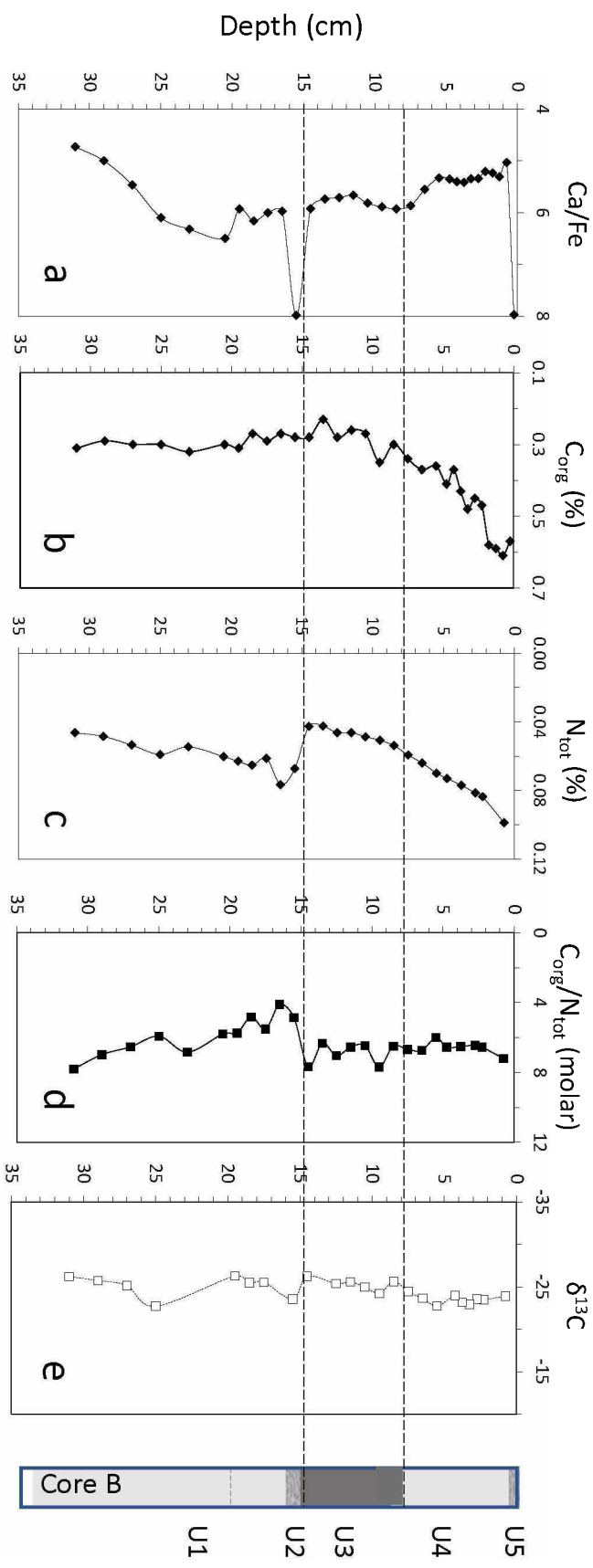


Fig. 4

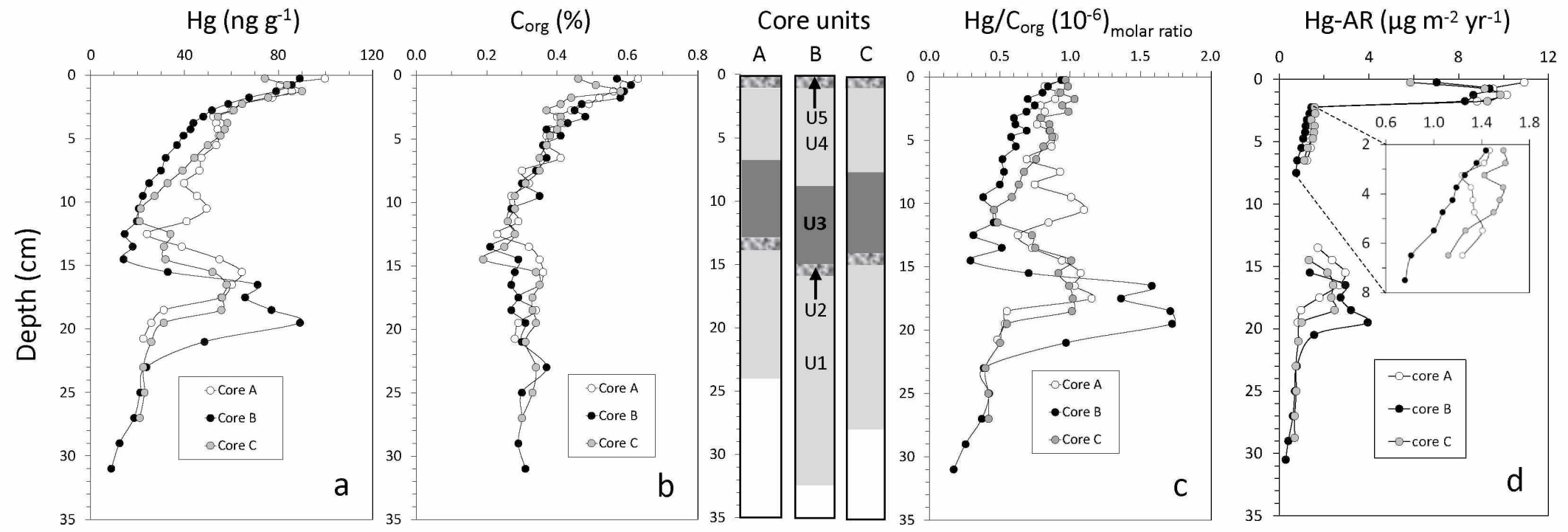


Fig. 5

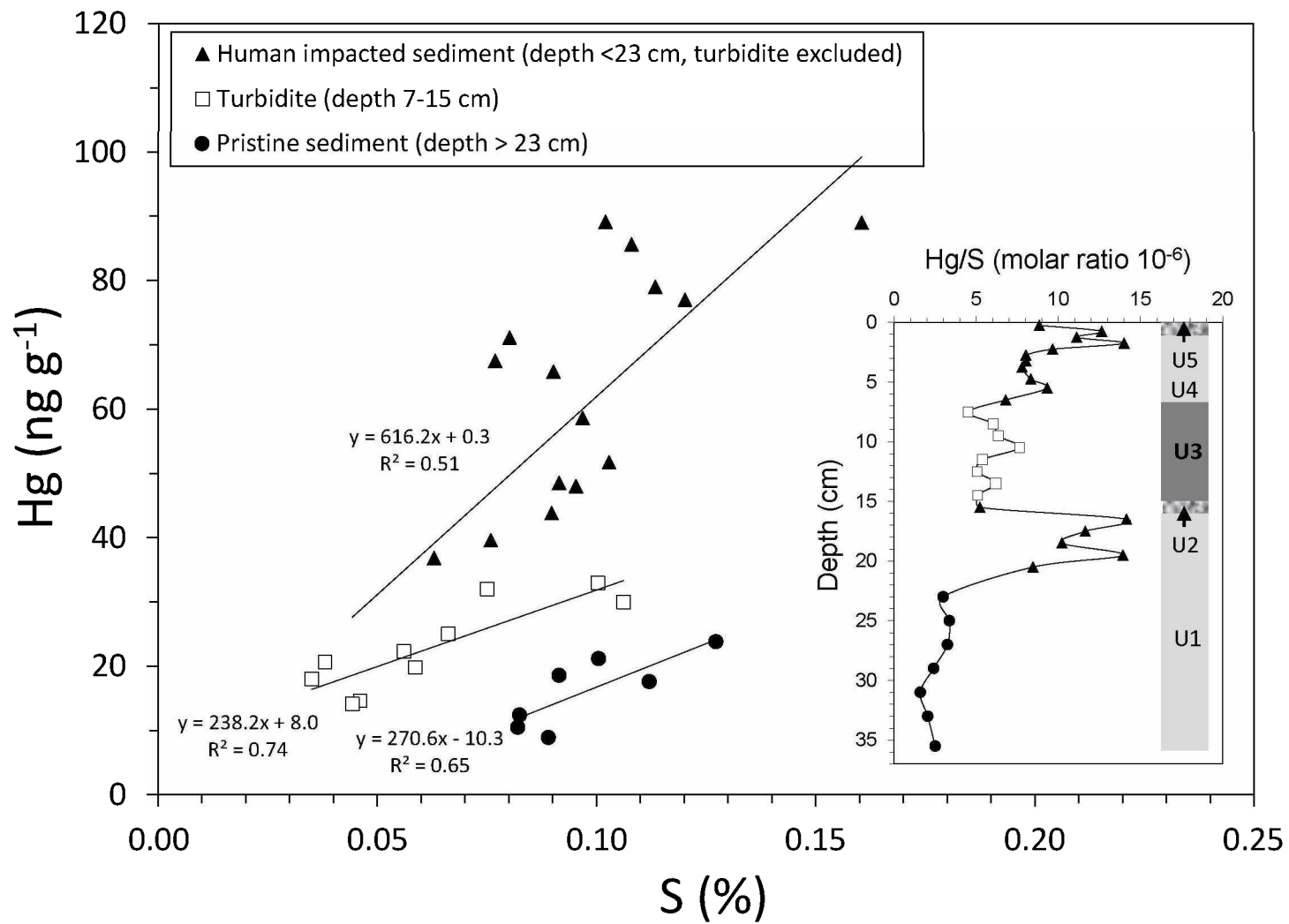


Fig. 6

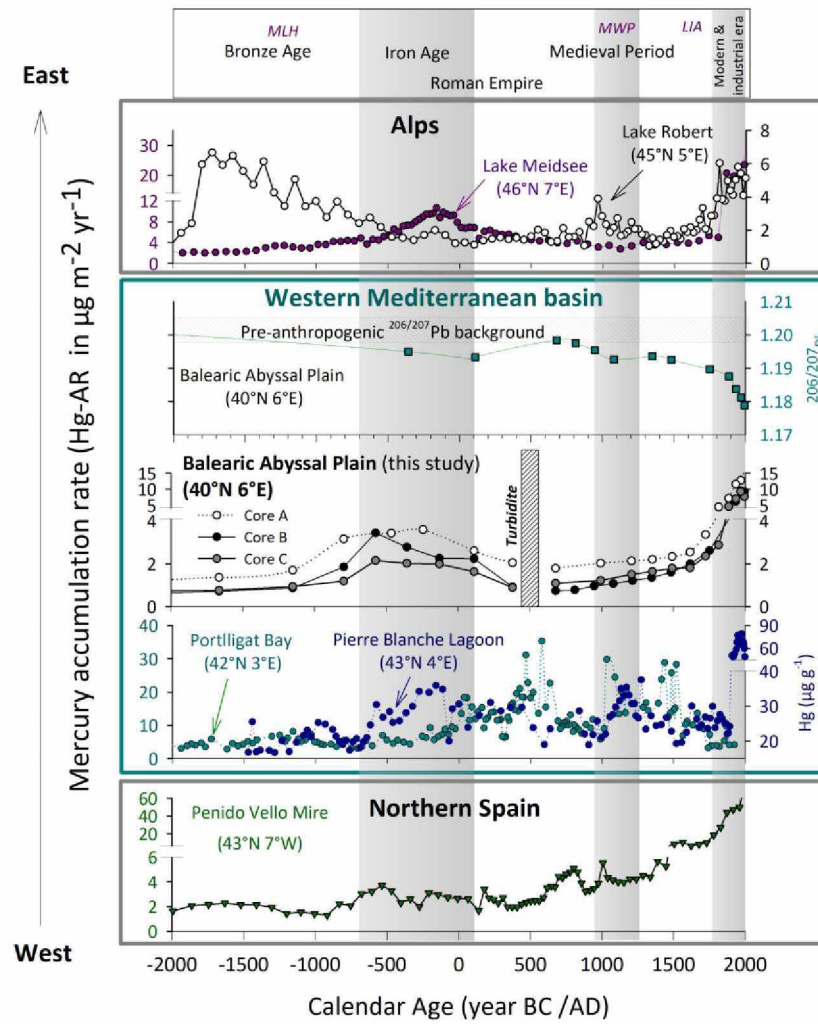


Fig. 7



Click here to access/download

**Electronic Annex**

ADIOS Hg Suppl Info v2.docx



## **Mercury accumulation in the sediment of the Western Mediterranean abyssal plain : A reliable archive of the late Holocene.**

Cossa, D.<sup>1,2\*</sup>, Mucci A.<sup>3</sup>, Guédron S.<sup>1</sup>, Coquery M.<sup>4</sup>, Radakovich O.<sup>5,6</sup>, Escoube R.<sup>2,7</sup>,  
Campillo, S.<sup>1</sup>, Heussner, S.<sup>8</sup>

<sup>1</sup>*Université Grenoble Alpes, ISTerre, CS 40700, F-38058 Grenoble Cedex 9, France*

<sup>2</sup>*IFREMER, Atlantic Center, LBCM, F-44031 Nantes, France*

<sup>3</sup>*Geotop and Department of Earth and Planetary Sciences, McGill University, 3450 University St., Montreal, QC, H3A 0E8 Canada*

<sup>4</sup>*INRAE, UR RiverLy, 5 rue de la Doua CS 20244, F-69625 Villeurbanne, France*

<sup>5</sup>*IRSN (Institut de Radioprotection et de Sûreté Nucléaire), PSE-ENV/SRTE/LRTA, F-13115 Saint-Paul-lès-Durance, France.*

<sup>6</sup>*Aix Marseille Université, CNRS, IRD, INRAE, Coll France, CEREGE, F-13545 Aix-en-Provence, France*

<sup>7</sup>*University of Cologne, Department of Geology and Mineralogy, D-50923 Köln, Germany*

<sup>8</sup>*Univeristé de Perpignan Via Domitia, CEFREM, UMR 5110, F-66860 Perpignan Cedex, France*

*\*Corresponding author: [dcossa@ifremer.fr](mailto:dcossa@ifremer.fr)*

### **Declaration of Competing Interest**

The authors declare that they have no known competing financial interests or personal relationships that could have appeared to influence the work reported in this paper.